

# **Bioengineering and biomechanical approaches for pancreatic cancer**

Tyler J. Lieberthal

March 2018

A thesis submitted for  
the degree of Doctor of Philosophy of Imperial College

Department of Bioengineering  
Imperial College London

**Imperial College  
London**

*The copyright of this thesis rests with the author and is made available under a Creative Commons Attribution Non-Commercial No Derivatives licence. Researchers are free to copy, distribute or transmit the thesis on the condition that they attribute it, that they do not use it for commercial purposes and that they do not alter, transform or build upon it. For any reuse or redistribution, researchers must make clear to others the licence terms of this work.*

*I declare this thesis and all work presented in it is the result of my own research, unless otherwise acknowledged or referenced.*

## Acknowledgements

I would like to acknowledge the support of fellow CMBL group members, past and present, and my advisor for their support in the last few years. I'm grateful for the technical help, guidance, and/or collaboration provided by the Department of Bioengineering (Shanas Choudhury, Joel Eustaquino, Kosta Rolev, and Danny O'Hare), London Centre for Nanotechnology (Peter Petrov and Andrei Mihai), Department of Materials (Deana Kwong Hong Tsang and Norbert Klein), Department of Medicine (Kevin Woollard), and Histology (Lorraine Lawrence).

This work and resulting thesis were made possible through financial support by the Whitaker International Foundation Fellowship and the James Dyson Foundation PhD Fellowship. Lastly, I would like to thank my family and friends for their unconditional encouragement.

## Abstract

Pancreatic cancer is the fourth-leading cause of cancer related mortality and is predicted to be the second leading cause of cancer death by 2030. A hallmark feature of pancreatic ductal adenocarcinoma (PDAC) is dense fibrotic stroma surrounding the tumor, composed of extracellular matrix (ECM) and cells such as myofibroblasts. The properties of this stroma and functional contribution to carcinogenesis and disease progression has been the subject of intense focus in the past decade; yet, the role of mechanobiology in modulating the phenotype of immune cells in the tumor microenvironment remains to be elucidated. Although a lack of understanding PDAC etiology and progression limits effective treatments that can be deployed by clinicians, current methods of diagnosing PDAC likely are insufficient even if such treatments exist, especially if there is a narrow early window for drug efficacy. Recently, however, extracellular vesicles have emerged as powerful circulating blood biomarkers, thus paving the way for a new era of non-invasive cancer diagnostics. However, currently the process of extracellular vesicle isolation and detection is not only highly inefficient, but also technically challenging.

This thesis describes bioengineering tools and biomechanical investigations of pancreatic cancer. In Chapter 2, the biomechanical phenotype of macrophages is studied in context of a stromal modulation agent, the chemotherapeutic drug tamoxifen. Tamoxifen was found to regulate macrophage focal adhesion dynamics, cytoskeletal activity, migratory behavior, and expression of TLR4. In Chapter 3, a novel microfluidic device was modeled and built to determine cell adhesion strength with potential applications to investigate regulation of focal adhesion structure by candidate drugs. Chapter 4 describes the development of methods and devices for isolation and detection of extracellular vesicles using acoustophoresis and a graphene field effect transistor, respectively. Such tools and perspectives could serve to detect PDAC earlier as well as identify and test new therapies.



## Table of Contents

<b>Acknowledgements</b> .....	<b>3</b>
<b>Abstract</b> .....	<b>4</b>
<b>List of figures</b> .....	<b>8</b>
<b>List of tables</b> .....	<b>9</b>
<b>List of abbreviations</b> .....	<b>10</b>
<b>Published Work</b> .....	<b>11</b>
<b>Chapter 1: Introduction</b> .....	<b>12</b>
1.1 Pancreatic ductal adenocarcinoma (PDAC) .....	12
1.2 Outlook .....	13
1.3 Histopathology, biomechanics, and the stroma .....	15
1.4 Macrophages in PDAC .....	22
1.4.1 Role of macrophages in PDAC progression.....	24
1.4.2 Mechanobiology of macrophages .....	26
1.5 Use of tamoxifen in PDAC .....	31
1.5.1 Research questions and hypotheses .....	32
1.6 PDAC biomarkers and diagnostics .....	33
1.6.1 Current biomarkers.....	33
1.6.2 Extracellular vesicles in PDAC .....	34
1.6.3 Engineered solutions for extracellular vesicle diagnostics .....	37
1.7 References .....	40
<b>Chapter 2: Tamoxifen modulates biomechanical phenotype of macrophages and TLR4 in the tumor microenvironment</b> .....	<b>56</b>
2.1 Introduction .....	57
2.2 Materials and Methods .....	58
2.2.1 Cells and reagents.....	58
2.2.2 Animals.....	59
2.2.3 Collection of conditioned media .....	59
2.2.4 2D migration .....	60
2.2.5 Polyacrylamide gel substrates.....	61
2.2.6 Immunofluorescence .....	61
2.2.7 Scanning electron microscopy.....	63
2.2.8 Fluorescence recovery after photobleaching (FRAP) microscopy .....	63
2.2.9 Western Blot.....	63
2.2.10 Quantitative RT-PCR.....	64
2.2.11 Statistics .....	64
2.3 Results.....	65
2.3.1 Tamoxifen reduces cell spread area and increases circularity.....	65
2.3.2 Morphological changes are recapitulated in fibrotic-like in vitro environments .....	65

2.3.3	Tamoxifen regulates talin-containing podosomes, cytoskeleton, and migration.....	68
2.3.4	Tamoxifen regulates TLR4 and downstream cytokines .....	72
2.3.5	TLR4 downregulation does not affect paracrine cytotoxicity .....	73
2.4	Discussion .....	76
2.4.1	Substrate stiffness modulation of macrophage phenotype .....	76
2.4.2	Role of TLR4 in PDAC.....	77
2.5	Conclusions .....	79
2.6	Contributions and Acknowledgements .....	79
2.7	References .....	79

### **Chapter 3: A multishear microfluidic device for determining cell adhesion strength 84**

3.1	Introduction .....	85
3.2	Materials and Methods .....	86
3.2.1	Device fabrication .....	86
3.2.2	Cell culture.....	88
3.2.3	Experimental set-up and Imaging.....	89
3.2.4	COMSOL simulations .....	89
3.3	Results.....	89
3.3.1	Device design.....	89
3.3.2	Adhesion strength of RAW264.7 macrophages .....	92
3.4	Discussion .....	93
3.5	Contributions and Acknowledgements .....	95
3.6	References .....	95

### **Chapter 4: Engineering a microfluidic diagnostic device for extracellular vesicle isolation and analysis ..... 97**

4.1	Introduction .....	98
4.1.1	Surface acoustic waves and interdigital transducers .....	98
4.1.2	Acoustophoresis.....	101
4.1.3	Graphene field effect transistors.....	105
4.1.4	Design considerations .....	106
4.2	Materials and Methods .....	110
4.2.1	Photolithography.....	110
4.2.2	Interdigital transducer fabrication .....	110
4.2.3	Graphene FET device fabrication.....	113
4.2.4	Biosensor functionalization.....	114
4.2.5	Electrical measurements .....	115
4.2.6	Collection of extracellular vesicles from cell culture supernatant .....	115
4.3	Results and Discussion .....	116
4.3.1	IDT fabrication and acoustophoresis.....	116
4.3.2	PDMS functionalization with antibodies .....	117
4.3.3	Graphene-microfluidic integration.....	119
4.3.4	XPS of exosomes on graphene.....	120
4.3.5	Exosome attachment to graphene biosensor.....	121
4.3.6	Graphene FET response to PBS.....	122
4.3.7	Dirac point shifts of exosomes.....	122
4.4	Conclusions .....	125

4.5 Contributions and Acknowledgements .....	126
4.6 References .....	126
<b>Chapter 5: Conclusions and future work .....</b>	<b>129</b>
5.1 Role of tamoxifen in immune modulation.....	129
5.2 Macrophage mechanobiology.....	129
5.3 Extracellular vesicle diagnostics .....	130
5.4 References .....	132
<b>Appendix: Copyright Permissions.....</b>	<b>134</b>

## List of figures

<b>Figure 1-1.</b> Survival of pancreatic cancer in comparison to other common cancers and projected cancer deaths .....	14
<b>Figure 1-2.</b> Tissue hallmarks of PDAC development.....	17
<b>Figure 1-3.</b> Major immune cells of whole blood and common progenitors and classifications .....	23
<b>Figure 1-4.</b> Descriptive relationship of populations of cell subtypes in the immune infiltrate between normal pancreatic tissue, non-cancerous benign pancreatitis, and PDAC.....	25
<b>Figure 1-5.</b> Tamoxifen reduces hypoxia and increases blood vessel density in a KPC mouse model of pancreatic cancer. ....	32
<b>Figure 1-6.</b> Low magnification (tiled 10x) immunohistochemistry staining of GPER in wild type (WT), PanIN (precursor lesions), and PDAC mouse tissues (n=3) .....	32
<b>Figure 1-7.</b> Exosome biogenesis .....	35
<b>Figure 2-1.</b> Preparation of CM from tamoxifen treated cells, media changes involved, and their purpose .....	60
<b>Figure 2-2.</b> Formation of polyacrylamide gel substrates for cell culture .....	61
<b>Figure 2-3.</b> Tamoxifen (TAM) induces morphological changes in RAW264.7 macrophages.....	66
<b>Figure 2-4.</b> Macrophages respond to substrates mimicking fibrotic environments...67	
<b>Figure 2-5.</b> Macrophage cell spread area and circularity on soft (1.2 kPa) or stiff (25 kPa) polyacrylamide gels conjugated with low (10 µg/mL) or high (50 µg/mL) fibronectin (FN) 48 hours after seeding.....	67
<b>Figure 2-6.</b> Confocal microscopy of F-actin stained macrophages grown on substrates mimicking little fibrosis (low stiffness, low FN) or high fibrosis (high stiffness, high FN) .....	68
<b>Figure 2-7.</b> Tamoxifen regulates focal adhesion dynamics and cell migration .....	70
<b>Figure 2-8.</b> Gene ontology enrichment of RAW264.7 macrophages cultured on soft (1.2 kPa) and stiff (150 kPa) substrates (data set GSE36878 (ref 13)).....	71
<b>Figure 2-9.</b> 2D migration distance and speed of macrophages is inhibited by tamoxifen .....	71
<b>Figure 2-10.</b> Tamoxifen reduces macrophage adherent density on fibronectin-coated glass, likely due to shear-induced detachment during staining .....	72
<b>Figure 2-11.</b> Tamoxifen downregulates TLR4 .....	74
<b>Figure 2-12.</b> Tamoxifen treatment and TLR4 inhibition is not associated with increased SUIT-2, BxPC-3, or PSC I cell proliferation .....	75
<b>Figure 2-13.</b> Expression of HIF-1α in pancreas tissue of KPC vehicle CTRL mice and mice treated with 5 mg tamoxifen by immunofluorescence (IF) .....	78
<b>Figure 3-1.</b> Fabrication of microfluidic channels using photolithography .....	87
<b>Figure 3-2.</b> Mask and mold required to reproduce PDMS channels.....	88

<b>Figure 3-3.</b> Design of variable shear microfluidic device .....	90
<b>Figure 3-4.</b> Uniformity of shear stress in wells.....	92
<b>Figure 3-5.</b> Detachment of RAW264.7 macrophages in microfluidic channels under shear .....	93
<b>Figure 3-6.</b> Proposed model for utilization of the device as a force applicator .....	94
<b>Figure 4-1.</b> Modes of acoustic waves and their orientations .....	99
<b>Figure 4-2.</b> Common modifications of IDTs .....	101
<b>Figure 4-3.</b> Simplified depiction of traveling and standing waves .....	102
<b>Figure 4-4.</b> Generation of standing surface acoustic waves (sSAWs) with interdigital transducers (IDTs).....	103
<b>Figure 4-5.</b> Schematic detailing the proposed isolation and detection of extracellular vesicles (EVs).....	109
<b>Figure 4-6.</b> Fabrication of IDTs with photolithography and thin film deposition .....	112
<b>Figure 4-7.</b> Antibody functionalization schematic via PEG linker .....	114
<b>Figure 4-8.</b> Brightfield micrographs of <b>(A)</b> IDTs and <b>(B)</b> the microfluidic channel ..	116
<b>Figure 4-9.</b> Distribution of beads in microfluidic channels .....	117
<b>Figure 4-10.</b> Non-specific adsorption of beads coated with BSA is reduced on silane-PEG-amine conjugated surfaces.....	119
<b>Figure 4-11.</b> Integration of graphene biosensor with microfluidic element .....	120
<b>Figure 4-12.</b> Nitrogen XPS spectra of graphene biosensor with increasing layers of functionalization.....	121
<b>Figure 4-13.</b> SEM of exosomes on graphene biosensor .....	121
<b>Figure 4-14.</b> Measurement of exosome concentration using a graphene field effect transistor.....	123
<b>Figure 4-15.</b> Current/gate voltage response to exosomes measured on graphene functionalized with an IgG isotype control antibody. ....	123
<b>Figure 4-16.</b> Graphene detection of exosomes is time-dependent.....	124
<b>Figure 4-17.</b> Dirac point shift of exosomes when a neutral buffer is replaced with a pH 5 solution, indicating a neutralization of exosome-mediated p-doping. ....	125

### List of tables

<b>Table 1.</b> Selected landmark studies in the past 20 years demonstrating the functional and therapeutic role of the desmoplastic stroma.....	19
<b>Table 2.</b> Comprehensive list of devices used to separate/purify and/or detect extracellular vesicles .....	38
<b>Table 3.</b> Cell lines used in this study.....	59

## List of abbreviations

$\alpha$ -SMA, $\alpha$ -smooth muscle actin	TGF- $\beta$ , transforming growth factor- $\beta$
AFM, atomic force microscopy	TIRF, total internal reflectance microscopy
ATRA, all-trans retinoic acid	TLR4, toll-like receptor 4
CDKN2A, cyclin-dependent kinase inhibitor 2A	TNF- $\alpha$ , tumor necrosis factor- $\alpha$
CM, conditioned media	TP53, tumor protein 53
DCSS, double charcoal stripped serum	TSAW, traveling surface acoustic wave
ECM, extracellular matrix	VEGF, vascular endothelial growth factor
EMT, epithelial-to-mesenchymal transition	$V_{DS}$ , drain-source voltage
ER, estrogen receptor	$V_g$ , gate voltage
ERK, extracellular signal-regulated kinase	XPS, x-ray photoelectron spectroscopy
EV, extracellular vesicle	
FAK, focal adhesion kinase	
FBS, fetal bovine serum	
FET, field effect transistor	
FN, fibronectin	
FRAP, fluorescence recovery after photobleaching	
HCC, hepatocellular carcinoma	
Hh, hedgehog	
HIF-1 $\alpha$ , hypoxia inducible factor-1 $\alpha$	
$I_{DS}$ , drain-source current	
IDT, interdigital transducer	
IHC, immunohistochemistry	
IL, interleukin	
KLA, Kdo2-Lipid A	
KPC, Pdx-1 Cre; KRas <sup>G12D/+</sup> ; p53 <sup>R172H/+</sup>	
KRAS, Kirsten rat sarcoma viral oncogene homolog	
LOC, lab on a chip	
LPS, lipopolysaccharide	
MCN, mucinous cystic neoplasms	
M $\phi$ , macrophage	
MCP-1, monocyte chemoattractant protein-1	
MEMS, microelectromechanical systems	
MIF, macrophage inflammatory factor	
PanIN, pancreatic intraepithelial neoplasia	
PBMC, peripheral blood mononuclear cell	
PDAC, pancreatic ductal adenocarcinoma	
PDMS, polydimethylsiloxane	
PMA, phorbol 12-myristate 13-acetate	
PMN, polymorphonuclear neutrophil	
$\Delta P$ , pressure drop	
PSA, prostate specific antigen	
PSC, pancreatic stellate cell	
Q, volumetric flow rate	
R, fluidic resistance	
ROCK, Rho associated protein kinase	
SAW, surface acoustic wave	
SEM, scanning electron microscopy	
SHG, second harmonic generation	
Smo, smoothened	
TAM, tamoxifen	

## Published Work

### Peer-reviewed publications

- **Lieberthal, T. J.** & Del Rio Hernandez, A. Tamoxifen modulates biomechanical phenotype of macrophages and TLR4 in the tumor microenvironment. 2018. *Submitted*.
- Tsang D. H. K., **Lieberthal T. J.**, Del Rio Hernandez A., & Klein, N. Chemically functionalised graphene FET with double conductance minima for the microfluidic sensing of exosomes. 2018. *Submitted*.
- Cortes E., Sarper M., Robinson B., Chronopoulos A., Lachowski D., Attwood S., Haining A. W., Karim S., **Lieberthal T. J.**, Morton J., & Del Rio Hernandez, A. GPER: A mechano-regulator of pancreatic stellate cells and the tumor microenvironment. 2018. *Submitted*.
- Cortes E, Robinson E, Sarper M, Lachowski D, Teppo J, Thorpe S, **Lieberthal T. J.**, Iwamoto K., Karim S., Haining A. W., Chronopoulos A., Lee D., Okada-Hatakeyama M., Varjosalo M., Morton J., & Del Rio Hernandez A. Tamoxifen mechanically reprograms the tumor microenvironment and the survival of cancer cells via HIF-1A. 2018. *Submitted*.
- Sarper, M., Cortes, E., **Lieberthal T. J.**, & Del Rio Hernandez A. ATRA modulates mechanical activation of TGF-beta by pancreatic stellate cells. *Sci Rep*. 2016; 6, 27639.
- Haining, A. W., **Lieberthal T. J.**, & Del Rio Hernandez A. Talin: a mechanosensitive molecule in health and disease. *FASEB J*. 2016; 30, 2073-2085.

### Other written work

- Chronopoulos A., **Lieberthal T. J.**, del Rio Hernandez A. Pancreatic cancer: a mechanobiology approach. *Converg. Sci. Phys. Oncol*. 2017; 1, 013001.
- Chronopoulos A., **Lieberthal T. J.**, del Rio Hernandez A. Exosomes as a platform for “liquid biopsy” in pancreatic cancer. *Converg. Sci. Phys. Oncol*. 2017; 1, 013005

## Chapter 1: Introduction

### 1.1 Pancreatic ductal adenocarcinoma (PDAC)

The pancreas is a major organ of the digestive tract, performing both endocrine functions (regulation of blood glucose) and exocrine functions (production of digestive enzymes). Endocrine cells are grouped into the islets of Langerhans, which secrete insulin, glucagon, somatostatin, and pancreatic polypeptide, all of which contribute to metabolism by controlling blood glucose concentration. Dysregulation of insulin secretion by the beta cells of the pancreas can lead to diabetes mellitus, a common pancreatic disease state. Exocrine functions are carried out by acinar cells, which secrete bicarbonate ions and synthesize digestive enzymes such as pancreatic amylase that collect in ducts composed of epithelia. Enzymes and ions that collect in pancreatic ducts drain into the duodenum during digestion. Pancreatic cancers of the endocrine cells are called neuroendocrine tumors and are less common and lethal than their exocrine counterpart, termed pancreatic ductal adenocarcinoma (PDAC)<sup>1</sup>. Several rare exocrine subtypes exist, but a majority of exocrine tumors and pancreatic tumors in general are of the ductal adenocarcinoma subtype. Hereafter, pancreatic cancer and PDAC will be used interchangeably.

PDAC afflicts mainly older adults, with 47% of cases occurring in people aged 75 and older and over 90% of cases in people over 55 (ref 2). The initiation and progression of PDAC can be described as an accumulation of age- and environmental-related trauma to the pancreas: diabetes, obesity, and smoking are risk factors<sup>3</sup>. Additionally, familial history of pancreatic cancer increases one's risk of developing the disease<sup>4</sup>. The incidence of pancreatic cancer is relatively low and, reflecting the late age at which it might appear, is only significant in the developed world. In the UK, pancreatic cancer comprises 3% of all cancer cases<sup>2</sup>.

PDAC begins as non-cancerous inflammatory precursor lesions of the epithelia such as pancreatic intraepithelial neoplasias (PanINs), intraductal papillary mucinous neoplasms (IPMNs), or mucinous cystic neoplasms (MCNs)<sup>5</sup>. Typically, cases of non-cancerous chronic pancreatitis feature the most important precursor lesion, PanIN, which can harbor the common (95% of PDAC cases) driver mutation – activated Kirsten rat sarcoma viral oncogene homolog (KRAS). As PanIN lesions progress through morphologically distinct stages, they accumulate tumor suppressor gene



mutations in cyclin-dependent kinase inhibitor 2A (*CDKN2A*, 75-80%), tumor protein 53 (*TP53*, 80%), SMAD family member 4 (*SMAD4*, 95%), among others<sup>6,7</sup>. Such driver mutations are common among primary PDACs and their metastases without much genetic heterogeneity<sup>8</sup>; however, the accumulated “passenger” mutations that do not alone promote tumorigenesis display heterogeneity and contribute to tumor growth, metastasis, and resistance<sup>9</sup>. These mutations perturb signaling pathways involving EGFR, PI3K/AKT, VEGF, WNT/ $\beta$ -catenin, and the TGF- $\beta$  pathway<sup>6</sup>. Low grade PanIN lesions may not lead to invasive pancreatic cancer, but the risk increases markedly for high grade (stage 3) lesions<sup>10</sup>.

Clinical presentation of PDAC often represents general symptoms of the presence of a tumor (e.g. weight loss); a symptom which may be specific to a pancreatic tumor is often jaundice, which can be a result of a biliary duct obstruction, particularly if the tumor is at the head of the pancreas. The first symptom may be abdominal pain resulting from tumor growth along the posterior wall of the abdomen<sup>6</sup>. Following hepatic function evaluation and imaging tests, if PDAC is confirmed by biopsy, the tumor can be staged by CT imaging, which determines severity by tumor size, involvement of lymph nodes, celiac axis, or superior mesenteric artery, and distant metastasis<sup>11</sup>. Unfortunately, surgical resection is the only potential curative therapeutic option, and most patients present with surgically unresectable tumors that show evidence of involvement with arteries or distant metastasis. Chemotherapy may be indicated for patients following surgical resection. Standard first line treatments used are nucleoside analogs like gemcitabine or 5-fluorouracil. New chemotherapy single agent or combination treatments may improve survival: the median overall survival of advanced pancreatic cancer with FOLFIRINOX (oxaliplatin, irinotecan, fluorouracil, and leucovorin) and nab-paclitaxel/gemcitabine compared to gemcitabine alone was 11.1 vs. 6.8 months and 8.5 vs. 6.7, respectively<sup>12,13</sup>, although such improvement still lag well behind other cancer subtype treatments.

## 1.2 Outlook

The prognosis of PDAC is notoriously bleak: the 5-year survival rate in England is 3.3% (ref 14). In general, advances in cancer detection and treatments have improved survival for most cancers and on average; however, the survival rate of pancreatic cancer is essentially unchanged in the past 40 years (**Figure 1-1A**). Furthermore, data

suggest that pancreatic cancer will become second leading cause of cancer related mortality in the US by 2030 (ref 15) (**Figure 1-1B**).

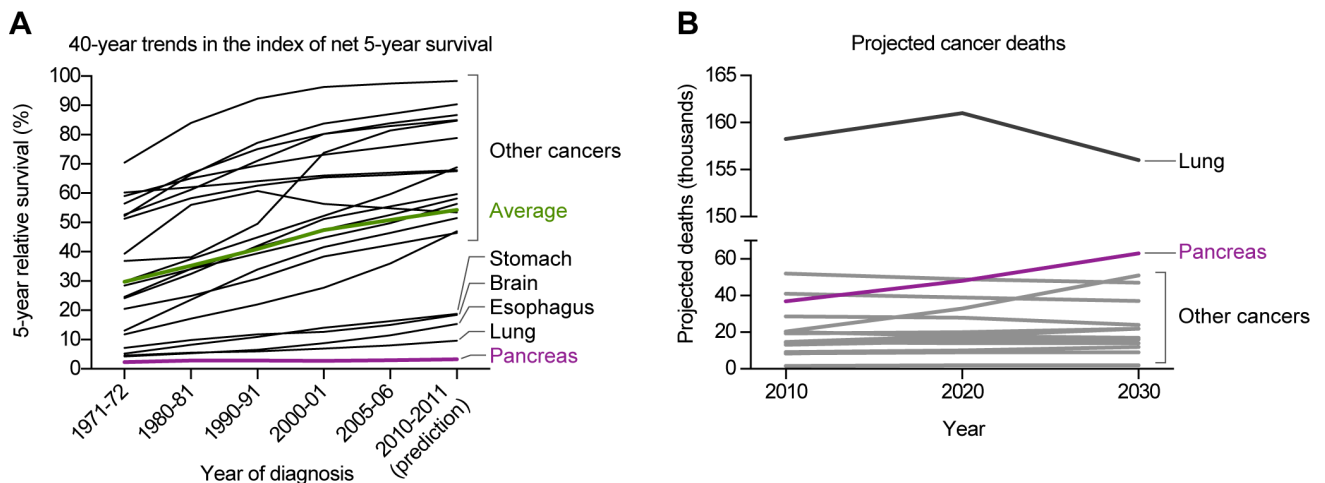


**Figure 1-1.** Survival of pancreatic cancer in comparison to other common cancers and projected cancer deaths. **(A)** 5-year survival rates by year of diagnosis for common cancers in England. Predicted 5-year survival rate for pancreatic cancer diagnoses in 2010-2011 was 3.3% at the time the analysis was published. Data adapted from Quaresma, et al. *Lancet* 2015; 385, 1206-1218 (ref 14). **(B)** Projected deaths from cancers by subtype in the United States. Pancreatic cancer is predicted to be the second-leading cause of cancer related death by 2030. Data adapted from Rahib, et al. *Cancer Res* 2014; 74, 2913-2921 (ref 15).

The poor prognosis of PDAC is due to several important factors. PDAC is a relatively rare incidence disease, which makes accurate detection difficult. Common risk factors as previously mentioned (diabetes, smoking, obesity) are insufficient to screen for a low incidence disease. Detection is also hindered by the non-specific presentation of symptoms that mimic benign illness such as stomach pain, weight loss, and indigestion; early stage PDAC may also be asymptomatic (NHS). PDAC may be diagnosed from routine imaging, but final medical decisions are decided based upon histopathological examination of tissue biopsies. Distinguishing non-invasive lesions from PDAC may be difficult even for experienced pathologists, and pre-emptive surgical resection may be recommended even for benign lesions. Finally, there are no clinically approved biomarkers that have the necessary sensitivity or specificity to effectively distinguish PDAC from benign lesions and healthy patients, thereby thwarting the opportunity for early detection. Current and new promising biomarkers are discussed in further detail in **Section 1.6** and **Chapter 4**.

Delayed cancer diagnosis implies delayed treatment and a narrowed therapeutic window to eradicate the tumor. However, even if detected early, PDAC remains a thoroughly recalcitrant tumor that resists conventional forms of chemotherapy and

radiation. Thus, detection of PDAC is often followed by an aggressive pancreaticoduodenectomy (Whipple procedure) if it has not spread beyond the pancreatic head<sup>16</sup>. For metastatic pancreatic cancer, treatment options are even more limited and palliative care is indicated. PDAC is particularly lethal because of its ability to metastasize, and metastasis can occur very early – even prior to the formation of the primary tumor<sup>17</sup>. There is a dearth of viable chemotherapeutic options mainly due to the lack of mutational drug targets, genetic heterogeneity<sup>18,19</sup>, and features unique to the PDAC tumor structure as described in **Section 1.3**. It is important to note that even in cases where a patient's tumor can be fully sequenced, apparent mutations may not readily suggest a candidate drug; one study found that empirical testing of drug candidates in patient derived models is necessary even with sequencing information available<sup>20</sup>. Such studies indicate that a holistic understanding of PDAC that incorporates emergent biochemical and biophysical properties is necessary to identify drug targets.

### 1.3 Histopathology, biomechanics, and the stroma

As previously discussed in **Section 1.2**, PDAC most often develops from precursor lesions called PanINs, which increase in severity over four morphologically distinct stages. Whereas normal ducts are organized into simple cuboidal epithelial cells, PanINs begin to exhibit more pseudostratified columnar epithelium with nuclear crowding and cribriform structures<sup>21</sup>. This is concomitant with an increase in overall tissue stiffness and integrin-mediated signaling (**Figure 1-2A**).

The critical molecular interactions that govern cell response to substrate stiffness relies on engagement of membrane proteins called integrins – which bind and anchor the cell to extracellular matrix (ECM) proteins – and intercellular integrin binding proteins that comprise the focal adhesion complex. Focal adhesion proteins like paxillin, vinculin, and talin are recruited to attachment sites and are subject to mechanical forces due to traction stresses developed by actomyosin contractility<sup>22</sup>. Talin, for example, unfolds under tension to reveal cryptic binding sites for vinculin, and talin regulation is implicated in a number of disease states related to this activity<sup>23</sup>. Another mechanotransduction pathway relies on YAP (Yes-Activated Protein) and TAZ (transcriptional co-activator with PDZ-binding motif), which are translocated to the nucleus in stiff substrate environments and regulate transcription of cell growth

and survival<sup>24</sup>. These pathways are relevant to disease states such as cancer and atherosclerosis where ECM or biomechanical parameters (i.e. shear stress) perturb homeostasis.

In cancer, the tumor cells coordinate with non-cancerous stromal cells to develop a characteristic milieu – a tumor microenvironment – featuring remodeled ECM and altered intercellular biochemical and intracellular paracrine networks. Specifically, the tumor microenvironment mimics an unresolved wound; in 1986, Harold Dvorak popularized the idea of cancer as “the wound that never heals,” a description that still resonates in cancer research 30 years later<sup>25,26</sup>. The presence of chronic inflammation and fibroblast activation results in considerable connective tissue – scar tissue in wounds and desmoplasia in solid tumors.

Certainly this is true of PDAC, for which fibroblast activation and extensive ECM deposition (desmoplasia) and an immune infiltrate (inflammation) are hallmarks. Surrounding the pancreatic ducts is a pronounced stroma containing pancreatic stellate cells (PSCs). Despite comprising only 4% of pancreatic parenchyma in normal tissue, PSCs are thought to be the lynchpin in the development of cancer<sup>27,28</sup>. PSCs were discovered in 1982 and characterized in 1998 as analogs to hepatic stellate cells (HSCs), which, like PSCs, are involved in tissue injury (HSCs, cirrhosis; PSCs, pancreatitis)<sup>27,29</sup>. Like with HSCs, PSCs exhibit two phenotypes: quiescent and activated. Under homeostatic conditions, quiescent PSCs store cytoplasmic vitamin A lipid droplets and contribute to tissue maintenance. In normal tissue, PSCs become activated upon inflammatory insult or injury by synthesizing ECM proteins like collagen. Simultaneously ECM is remodeled via secreted proteases such as metalloproteinases (MMPs). Activated PSCs express  $\alpha$ -smooth muscle actin ( $\alpha$ -SMA) and are a prominent presence in the PDAC stroma<sup>30</sup>. Multiple cytokine signaling networks exist between PSCs, other stromal cells, and cancer cells. Cancer cells can induce proliferation and activation of PSCs, which then secrete growth factors and chemokines that regulate endothelial cells, T-cells, neurons, and cancer cells themselves<sup>31</sup>. As a result of the abundant fibrosis produced by PSCs, tumors are mostly hypovascular with insufficient collapsed vessels, leading to hypoxia. The increased matrix stiffness and hypoxia in turn leads to further PSC activation and fibrosis, thus establishing a deleterious positive feedback loop (**Figure 1-2B**). Culture

of myfibroblasts on stiff substrates *in vitro* is also sufficient to induce expression of  $\alpha$ -SMA and stimulate a wound-repair transcriptional program<sup>32</sup>.

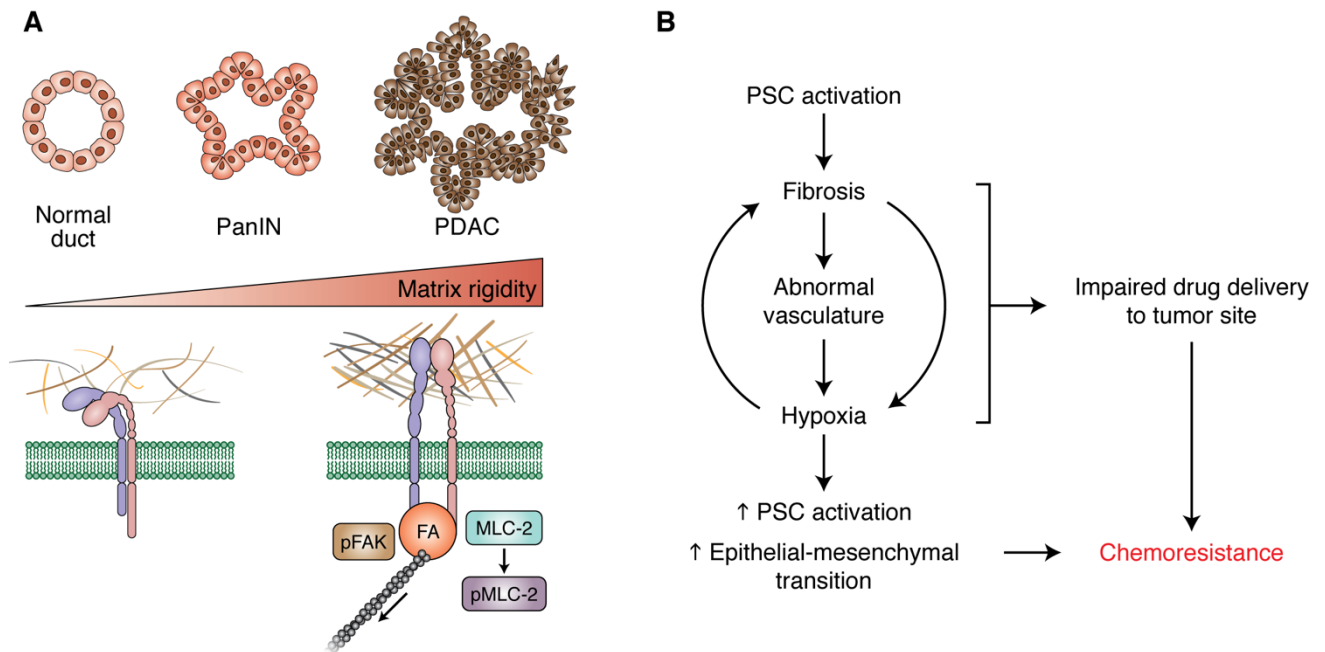


**Figure 1-2.** Tissue hallmarks of PDAC development. **(A)** Duct disorganization associated with PDAC. As ducts progress from pre-cancerous lesions (pancreatic intraepithelial neoplasia; PanIN) to PDAC, ductal cells become more columnar and pseudostratified with simultaneous increase in ECM deposition, leading to increased tissue rigidity. Integrins become activated by outside-in and inside-out signaling and initiate downstream signaling pathways via focal adhesion (FA) proteins, phosphorylated focal adhesion kinase (pFAK), and myosin light chain-2 (MLC-2). Adapted from Chronopoulos A, Lieberthal TJ, and del Rio Hernandez A. *Converg. Sci. Phys. Oncol.* 3 (1), 013001 (ref 33) with permission. **(B)** Cycle of perpetual tissue fibrosis initiated by activated PSCs, ECM protein deposition, poor perfusion, and hypoxia. As a consequence of desmoplasia, chemotherapeutic drugs are unable to penetrate the tissue and duct epithelia undergo mesenchymal transition.

However, the functional contribution of the non-cellular component of the peritumoral tissue to tumor progression is subject to intense debate in the field. It has been noted early in the characterization of PDAC that ductal tumors are dense and obtrusive based on gross anatomy and that tumors contain an abundance of connective tissue. Indeed, most (90%) of the tumor volume is composed of stroma. In view of the wound model of cancer, the stromal reaction was initially thought to be a byproduct of the resolution process and a physiological reaction intended to restrain cancer from dissemination; this view was largely abandoned for many by 2011 (ref 34), but was later reexamined thoroughly in 2014 by several studies<sup>35,36</sup>. **Table 1** contains selected landmark studies that document the evolution in the consensus (or lack of consensus) in the understanding of the PDAC stroma.

In general, chemotherapeutics that target the stroma are used in combination with standard cytotoxic drugs given that they are typically not intended to target the tumor cells themselves. Two early combination treatments that specifically targeted the stroma were MMP inhibitors, the use of which aligned with the stromal protection theory. An imbalance in MMPs over their inhibitors was thought to allow breaches of the stroma and therefore contribute to local invasion and metastasis. However, either broad-spectrum or specific MMP inhibitors in combination with gemcitabine, the standard chemotherapeutic drug, failed to improve overall survival in patients<sup>37,38</sup>.

In 2005, V. Weaver and colleagues published a pioneering study in mechanobiology that demonstrated substrate stiffness-dependent disruption of epithelial duct morphogenesis via enhanced integrin signaling, Rho associated protein kinase (ROCK) and extracellular signal-regulated kinase-1 (ERK) activation, and cytoskeletal tension<sup>39</sup>. (Chaudhuri *et al.* (2014) also showed substrate stiffness-dependent disruption of epithelial morphogenesis using an alginate-laminin biomaterial platform<sup>40</sup>). Later, they demonstrated that extensive crosslinking of ECM (specifically collagen) by lysyl oxidase (LOX) can similarly increase tissue stiffness and drive integrin signaling and mechanotransduction pathways, leading to more invasive behavior of cancerous mammary epithelium<sup>41</sup>. Indeed, LOX inhibitors have been shown to demonstrate chemotherapeutic improvement<sup>42</sup>. Importantly, the abundance of collagen in tumors is only one facet of the tumor-ECM signature; stromal collagen fibers are known to align into bundles whereas healthy tissue contains randomly oriented collagen as determined by second harmonic generation microscopy (SHG), thereby providing “tracks” on which cancer cells can invade<sup>43</sup>. Although these three studies were conducted using breast cancer as a model, the implications are far-ranging – from basic cell biology to other cancers and disease states. Breast ductal carcinoma bears many similarities to PDAC, including disrupted duct morphology and increased tissue stiffness.

In 2009, Olive *et al.* documented the insufficiencies of tumor transplant models of PDAC, showing that transplanted tumors do not develop desmoplasia akin to native *in situ* tumors<sup>44</sup>. The genetically engineered mouse model used in the study was previously reported by the same group; mutations are initiated by conditional activation of transgenic mice bearing **KRas**<sup>G12D/+</sup>; **p53**<sup>R172H/+</sup> mutations under control of pancreatic promoter Pdx-1-driven **Cre** recombinase (KPC mice)<sup>45,46</sup>.

**Table 1.** Selected landmark studies in the past 20 years demonstrating the functional and therapeutic role of the desmoplastic stroma.

Year	Key result(s)	Citation
2002	Broad-spectrum MMP inhibitor marmastat offers no improvement in combination with gemcitabine.	Bramhall, et al. <i>Br J Cancer</i> . 2002; 87, 161-167. (ref 37)
2003	A MMP-2, MMP-3, MMP- 9 and MMP-13 inhibitor is significantly inferior to gemcitabine.	Moore, et al. <i>J Clin Oncol</i> . 2003; 21, 3296-3302. (ref 38)
2005	Enhanced matrix stiffness increases cytoskeletal tension and disrupts mammary epithelial morphology.	Paszek, et al. <i>Cancer Cell</i> . 2005; 8, 241-254. (ref 39)
2006	Aligned collagen fibers in breast cancer is a tumor signature and allows invasion of cancer cells.	Provenzano, et al. <i>BMC Med</i> . 2006; 4, 38. (ref 43)
2009	Crosslinking of collagen via LOX promotes breast tissue stiffening, integrin signaling, and tumor invasion.	Levental, et al. <i>Cell</i> . 2009; 139, 891-906. (ref 41)
2009	Combination therapy of gemcitabine and a drug that inhibits the Hedgehog and depletes tumor-associated stromal tissue.	Olive, et al. <i>Science</i> . 2009; 324, 1457-1461. (ref 44)
2011	CD40 agonist reprograms macrophages and reduces fibrosis in PDAC mouse model.	Beatty, et al. <i>Science</i> . 2011; 331, 1612-1616. (ref 47)
2011	ROCK activation increases actomyosin contraction and cell tension. Collagen deposition and skin carcinoma tumor growth are promoted by ROCK.	Samuel, et al. <i>Cancer Cell</i> . 2011; 19, 776-791. (ref 48)
2012	Hyaluronic acid component of stromal ECM raises interstitial fluid pressure and collapses blood vessels. Enzymatic degradation of HA improves survival and reduces desmoplasia.	Provenzano, et al. <i>Cancer Cell</i> . 2012; 21, 418-429. (ref 49)
2014	Hh pathway inhibition accelerates tumor growth while depleting stroma by increasing progenitor-like epithelial cells.	Lee, et al. <i>PNAS</i> . 2014; 111, E3091-3100. (ref 50)
2014	Shh-deficient tumors are more aggressive.	Rhim, et al. <i>Cancer Cell</i> . 2014; 25, 735-747. (ref 36)
2014	Myofibroblast ablation increases tumor aggressiveness and reduces survival.	Ozdemir, et al. <i>Cancer Cell</i> . 2014; 25, 719-734. (ref 35)
2014	Vitamin D receptor reprograms PSCs and improves chemotherapy.	Sherman, et al. <i>Cell</i> . 2014; 159, 80-93. (ref 51)
2016	Mutations in TGF- $\beta$ effectors, increased JAK/STAT signaling, and integrin activation increases ROCK-dependent cell contractility and p-MLC, which increases tissue stiffness and collagen remodeling.	Laklai, et al. <i>Nat Med</i> . 2016; 22, 497-505. (ref 52)
2016	FAK inhibition in cancer cells reduces tissue fibrosis and potentiates T-cell immunotherapy	Jiang, et al. <i>Nat Med</i> . 2016; 22, 851-860. (ref 53)
2017	Priming tissue with a ROCK inhibitor sensitized tumors to chemotherapy in KPC and PDX models.	Vennin, et al. <i>Sci Transl Med</i> . 2017; 9. (ref 54)

They hypothesized that the dense stroma was causally related to the collapse of a vascular network required for drug delivery. To disrupt the stroma and increase drug perfusion, they targeted the hedgehog (Hh) pathway, which induces desmoplasia via paracrine signaling from tumor cells to stromal cells<sup>55,56</sup>.

Remarkably, smoothed (Smo; a membrane protein component of the Hh pathway) inhibition dramatically reduced  $\alpha$ -SMA expressing fibroblasts, increased vessel density, enhanced delivery of doxorubicin and gemcitabine, increased median survival of mice, and reduced liver metastases. Yet, the response to the Smo inhibitor was only transient (hypovascularity and tumor growth relapsed), ultimately limiting the increase in median survival. Nevertheless, this study established a new paradigm in the field that posited several lasting hypotheses regarding PDAC fibrosis: the tumor stroma (1) is a barrier to drug delivery and treatment (2) weakens and reduces the vasculature and (3) can be depleted by targeting cancer associated myofibroblasts either directly or indirectly. This study also confirmed the usefulness of the KPC mouse model for studying PDAC.

Unfortunately, despite much promise, several clinical trials of Hh inhibitors yielded either underwhelming results or even reduced survival<sup>57-59</sup>. A series of studies in 2014 sought to determine the shortcomings of *Shh* inhibition and elucidate the functional role of the stroma. Lee *et al.* used various genetically engineered mouse models (*Shh* deletion with driver mutations) as well as pharmacological inhibition and activation of the *Hh* pathway to demonstrate that *Hh* suppression increased the formation of PanINs and eventual PDAC while reducing survival<sup>50</sup>. Consistent with Olive *et al.*, *Hh* inhibition reduced fibrosis, and *Hh* activation produced a pronounced stroma. However, the disappearance of the fibrotic stroma upon *Hh* inhibition was concomitant with compensatory epithelial proliferation. Epithelial cells were also more undifferentiated, exhibiting a progenitor-like phenotype.

Two other studies published in 2014 in the same issue of *Cancer Cell* also addressed the conflicting reports. Like the previous study, Rhim *et al.* used *Shh*<sup>fl/fl</sup> mice to understand the overall effect of *Shh* inhibition in PDAC and found that *Shh* deletion increased tumor aggressiveness and reduced survival<sup>36</sup>. Tumors were also poorly differentiated, an indication of poor prognosis. Following up on their 2009 study, they carried out longer term Smo inhibition, which revealed that the transient response



seen earlier was eventually overcome by aggressive tumor growth. The increase in vascularization, previously thought to facilitate drug delivery, likely only contributed to delayed autophagy in tumor cells. Ozdemir *et al.* took a more direct approach by ablating  $\alpha$ -SMA<sup>+</sup> myofibroblasts to understand the role of fibrosis in PDAC. Expectedly, removal of myofibroblasts led to stromal depletion mostly due to absent collagen and a softening of the tissue as measured by atomic force microscopy (AFM). However, tumors remained hypovascular and hypoxic and an increase in gemcitabine efficacy was not observed. Interestingly, myofibroblast ablation also significantly modulated the adaptive and immune response to reduce survival.

Predictably, the consensus on the role of the tumor stroma had to be re-evaluated, and further study was required to understand whether the pancreatic cancer stroma was, indeed, a “friend or foe”<sup>60</sup>. In the last few years, there has been a focus on further elucidating the genetic interactions with mechanobiology of the stroma<sup>52</sup> and other stromal modulation strategies. One promising target is hyaluronic acid (HA), a glycosaminoglycan of the ECM that binds water and elevates interstitial fluid pressure or solid stress<sup>49,61</sup>. In several cancers, HA has been shown to be elevated along the invasive front of tumors, contributing to an increase in cell proliferation and migration<sup>62</sup>. Administration of a polyethylene glycol and PH20 hyaluronidase (PEGPH20) conjugate reduces hyaluronic acid in the stroma and relieves pressure. Unlike the Smo inhibitor, PEGPH20 did not increase vascularity, but allowed existing vessels to become patent and able to deliver chemotherapeutics<sup>49,63</sup>. A phase II trial of PEGPH20 with gemcitabine and nab-paclitaxel reported encouraging results in early 2017; a phase III trial is currently under way (NCT02715804).

Since the failure of *Shh* inhibitors, the concept of stromal depletion has arguably become more nuanced to recognize the complexity of interactions involved; “stromal modulation” is perhaps more appropriate. In view of this, Vennin *et al.* (2017) recently used transient treatment of a ROCK inhibitor (Fasudil) to “prime” the tissue for chemotherapy<sup>54</sup>. As mentioned previously, ROCK is an essential component of tumor mechanobiology in which integrin engagement and ERK activation stimulate ROCK-mediated actomyosin contractility, additional force generation, and perturbed tissue architecture<sup>39,48,52</sup>. This study deployed a remarkable suite of tools to interrogate biomechanical and biomechanical properties of cells and tissues such as SHG imaging, AFM, gel contraction assays, organotypics, Förster resonance energy

transfer (FRET) biosensors, shear stress assays, intravital imaging, and patient derived xenograft (PXD) models. Beyond demonstrating the individual efficacy of Fasudil, this study suggests that stromal modulating by “priming” the tissue prior to first-line chemotherapy as a neo-adjuvant, rather than chronic treatment, may be utilized with other stromal modulation candidates such as PEGPH20 and LOX inhibitors<sup>64</sup>.

## 1.4 Macrophages in PDAC

The aforementioned studies on tumor cell mechanobiology or tissue mechanics are often studied alongside the cells of the immune system, which (like in the wound microenvironment) are integral to initiation, progression, and treatment of cancer. In recognition of the dynamic role immunology plays in cancer and the potential to harness the immune system for therapeutics, cancer immunology is a growing and exciting field. Broadly, the immune system can be divided into innate and adaptive immunity, the latter typically wielded in new forms of cancer immunotherapy, which was named the “breakthrough of the year” in 2013 by *Science*<sup>65</sup>.

The extensive specialization required of the immune system naturally gives rise to divisions in cell type subsets that differentiate from common progenitors. Within one cell type subset, further phenotypic plasticity may prompt further divisions in hematopoietic taxonomy. Besides containing platelets and erythrocytes, whole blood contains peripheral blood mononuclear cells (PBMCs) and granulocytes, which are formed from hematopoietic stem cells in the bone marrow. Cells derived from the myeloid lineage include monocytes – which differentiate into macrophages (M $\phi$ ) and dendritic cells – and granulocytes, including mast cells, polymorphonuclear neutrophils (PMN), eosinophils, and basophils. Cells of lymphoid progenitors, with the exception of natural killer (NK) cells, comprise the adaptive immune system (**Figure 1-3**).

The diversity of cell types is required for compartmentalization of functions and response to pathogens with various mechanisms of action. Temporal control of the immune response is also highly regulated by cell type with cells of the innate immune system (e.g. monocytes, PMN) orchestrating initial inflammatory cascades via cross-talk with fibroblasts and T cells. Macrophages play an important role in the wound environment as professional phagocytes by disabling opportunistic pathogens and

clearing apoptotic PMNs, after which they contribute to ECM remodeling, angiogenesis, and wound resolution<sup>66</sup>.

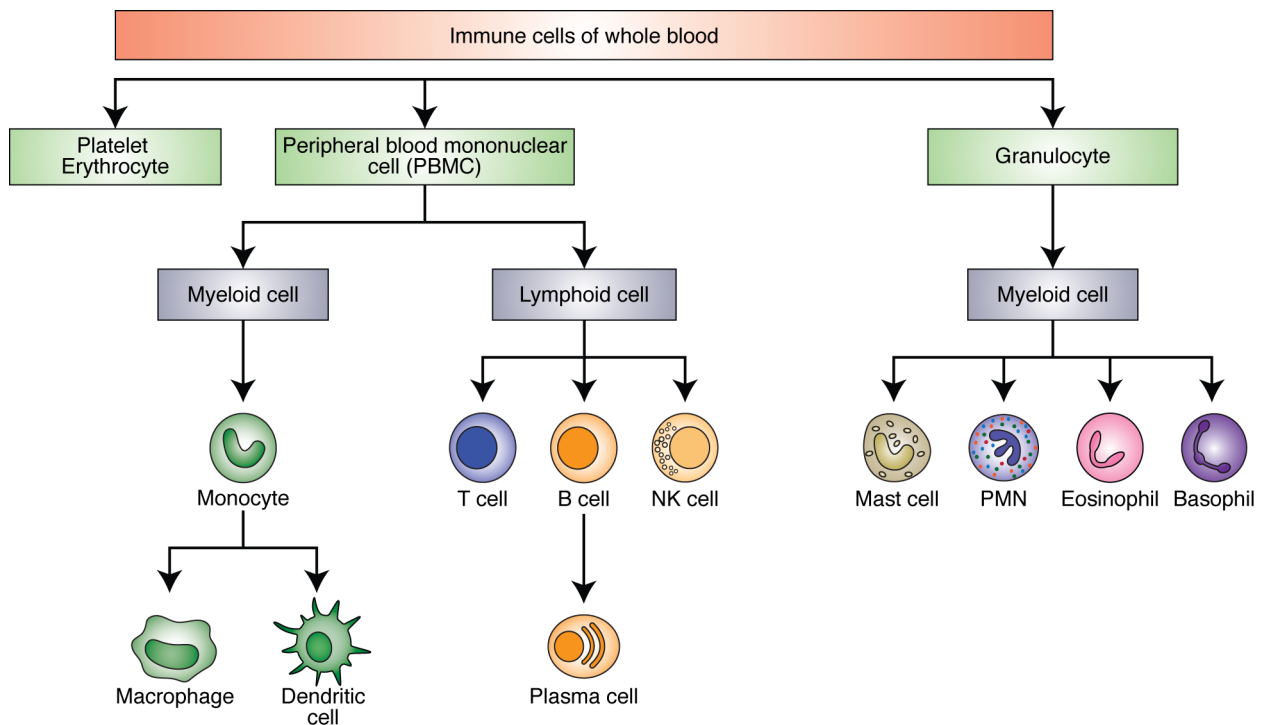


**Figure 1-3.** Major immune cells of whole blood and common progenitors and classifications. NK, natural killer; PMN, polymorphonuclear neutrophil. Myeloid and lymphoid are the major classifiers of immune cells. Whole blood can be fractionated into PBMC and granulocyte layers based on density.

A hallmark of tumor microenvironments is chronic inflammation, which is initiated by macrophages and PMN in concert with cancer-associated fibroblasts<sup>67</sup>. A related hallmark is immunosuppression: cytotoxic CD8<sup>+</sup> T cells are deactivated and unable to recognize and destroy cancer cells. The lack of an immune response to cancer is in part a result of the adaptive immune system's tight control over recognition of self antigens (the disruption of which leads to autoimmune disease); cancer, unlike pathogens, may not express antigens that are recognized as foreign<sup>68</sup>. Additionally, paracrine signaling from stromal cells as well as cancer cells themselves contribute to immunosuppression. Macrophages in particular have multifaceted functions in the tumor stroma by promoting chronic ECM turnover and suppression of T cells.

To elucidate the functional phenotype of macrophages in the tumor microenvironment, cancer researchers have adopted a classification system previously used by wound healing researchers: M1 and M2 type macrophages. In wound healing, M1 (classically activated or inflammatory) macrophages are associated with the initial inflammatory response needed to phagocytose pathogens and apoptotic PMNs as well as present

antigens to cells of the adaptive immune system. Stimulation of naïve macrophages with lipopolysaccharide (LPS, or endotoxin, a component of the bacterial cell wall) and interferon gamma (IFN- $\gamma$ ) are said to induce the inflammatory M1 phenotype, which secretes tumor necrosis factor- $\alpha$  (TNF- $\alpha$ ), interleukin-1 $\beta$  (IL-1 $\beta$ ), IL-6, IL-1, reactive oxygen species, and inducible nitric oxide synthase (iNOS), among others. M2 (alternatively activated or anti-inflammatory) macrophages are instead called “pro-wound healing” – to contrast them with the “pro-inflammatory” M1 macrophages – and they are associated with dampening the immune response and stimulating angiogenesis via secretion of vascular endothelial growth factor (VEGF), TGF- $\beta$ , and IL-10; they are induced by IL-4 and IL-13. Some have argued for further subdivision of M2 into M2a, M2b, M2c, M2d<sup>69</sup>.

This M1/M2 system was first formalized in 2000, and shortly thereafter cancer researchers widely adopted this classification system with the modification that M1 macrophages are “anti-tumor” and M2 macrophages are “pro-tumor”<sup>70,71</sup>. However, the M1/M2 phenotypes are far from binary, and their use in published work likely obfuscates underlying complexity of macrophage behavior. It allows a simple way to understand whether a particular treatment may beneficially polarize macrophages by determining the expression of one or two selected molecular markers. Yet, further interrogation of the phenotype often reveals a “mixed M1/M2 phenotype” or a failure to classify macrophages, which undermines the validity of the system<sup>72</sup>. In recent years, several high-profile review articles and editorials have argued for a re-evaluation or abandonment of the M1/M2 paradigm and a more nuanced or precise interrogation of macrophage phenotype<sup>73-78</sup>. Furthermore, it should be understood that M1 and M2 macrophages, such as they exist, cannot be reduced down to “good” or “bad” macrophages, respectively<sup>79</sup>. Inevitably, such a view requires instead a wide overview and analysis of macrophage gene expression using transcriptomic profiling and an understanding that, for example, IFN- $\gamma$ /LPS-stimulated macrophages are best described not by an arbitrary classifier such as M1 but can be more precisely defined as just that: an IFN- $\gamma$ /LPS-stimulated macrophage<sup>77</sup>.

#### 1.4.1 Role of macrophages in PDAC progression

Macrophages have been implicated in the initiation and progression of PDAC as well as the formation of liver metastases. Immune infiltration with significant populations of macrophages is a typical feature of PDAC. The presence of macrophages can be

determined by CD68 positivity or F4/80 positivity (murine macrophages only) in tissue. The population of tissue immune infiltration evolves over the course of PDAC progression; notably, the initial inflammatory stage of benign pancreatitis features many inflammatory macrophages. Characteristic of the immunosuppressed tumor microenvironment, the number of cytotoxic CD8 T cells is reduced after tumorigenesis (**Figure 1-4**)<sup>80</sup>.

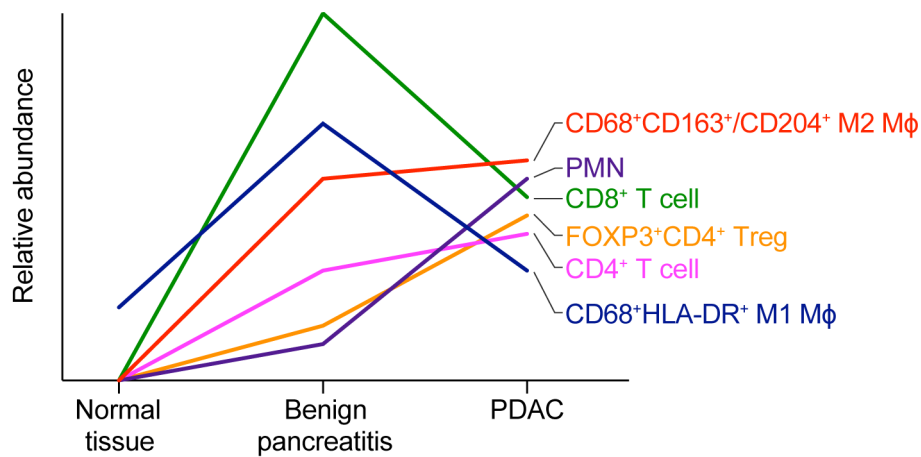


**Figure 1-4.** Descriptive relationship of populations of cell subtypes in the immune infiltrate between normal pancreatic tissue, non-cancerous benign pancreatitis, and PDAC. The M1/M2 macrophages were defined by the authors; the M2 Mφ population was defined as either CD163 or CD204 positivity along with the pan-Mφ marker CD68. Ratios of immune cell populations predict long- or short-term survival; higher ratio of M1/M2 or (CD4 or CD8 T cells)/Tregs are associated with significantly longer survival. Relative changes between the three tissue types adapted from Ino, et al. *Br J Cancer*. 2013; 108, 914-923 (ref 80).

Therapeutic efforts have hypothesized that inhibiting macrophage infiltration or inducing a transcriptional program that stimulates CD8 T cells would beneficially reduce deleterious inflammation and provoke adaptive immune responses. To that end, Nywening *et al.* (2016) reported a phase 1b trial of a CCR2 inhibitor with FOLFIRINOX (folinic acid, fluorouracil, irinotecan, oxaliplatin), in which inhibition of CCR2 (that binds to CCL2 or monocyte chemoattractant protein-1; MCP-1) blocks mobilization of bone marrow derived monocytes from infiltrating into the tissue. Combination of CCR2 and CXCR2 inhibition (which target monocytes and PMNs, respectively) was also recently shown to improve chemotherapy efficacy<sup>81</sup>.

Alternatively, tissue resident or infiltrated macrophages could be reprogrammed to stimulate adaptive immunity. Instead of inhibiting macrophage infiltration, these efforts focus on redirecting the presence of macrophages for anti-tumor activity. Kaneda *et*

*al.* (2015) demonstrated that PI3K $\gamma$  inhibition in macrophages reduced expression of *Arg1*, *Tgfb*, and *Il10*, which allowed recruitment and activation of CD8 T cells; additionally, PI3K $\gamma$  inhibition reduced expression of platelet-derived growth factor (PDGF-BB), which stimulates fibroblast-dependent desmoplasia<sup>82</sup>. Another study also demonstrated that a CD40 agonist, initially employed to activate T cell immunity, instead could activate tissue macrophages, reduce collagen in the tissue, and reduce the tumor burden in clinical trials<sup>47</sup>. In a subsequent study, they found that CD40 promoted secretion of CCL2, which, in combination with IFN- $\gamma$ , depleted stromal fibrosis via MMPs – an apparent reversal of the strategy adopted by administration of CCR2 inhibitors<sup>83</sup>. Whether macrophages can beneficially be inhibited, ablated, or reprogrammed for treatment of PDAC, and which population should be targeted, is currently an intensive area of research.

#### 1.4.2 Mechanobiology of macrophages

In investigating the mechanisms of mechanobiology and the relationship to tumor biology, naturally questions may arise concerning the mechanobiology of stromal cells like macrophages in addition to fibroblasts and cancer cells. The extent to which macrophages are subject to the same mechanical stimuli and response as stromal and tumor cells is unclear. It is not immediately apparent whether macrophages or other immune cells should rely on the same mechanotransduction mechanisms as fibroblasts and epithelia previously studied (see **Section 1.3**) given that fundamental properties and functions like adhesion and migration may significantly differ<sup>84</sup>. In T cells, for example, specialized mechanobiology pathways exist in the cell-cell contact between T cells and target infected cells<sup>85</sup>, and innate immune cells must perform mechanically demanding activities such as phagocytosis. Fundamental questions of macrophage mechanobiology may be important in other disease states as well such as atherosclerosis and the foreign body response to implanted devices.

In several limited studies, macrophage responses to substrates of variable stiffnesses have been investigated as well as the response to shape regulation, but agreement between them is lacking<sup>86</sup>. Early evidence for mechanical regulation of macrophages comes from studies in which cyclic mechanical strain or pressure was applied to macrophages to simulate the physical environment of alveolar macrophages. Under cyclic strain or pressure, macrophages mostly upregulate inflammatory cytokines such as IL-8, TNF- $\alpha$ , IL-6, MMPs, and the transcription factor NF $\kappa$ B, which may be

dependent on exogenous stimuli like LPS, PMA, or hypoxia<sup>87-90</sup>. The morphology and actin cytoskeletal and focal adhesion organization is also regulated by cyclic strain<sup>91</sup>.

Hydrogel substrates have been extensively utilized to determine how macrophages respond to different substrate stiffnesses. On stiffer polyacrylamide substrates, macrophages increase cell spread area, polarize their morphology, reduce proliferation rate, and increase phagocytic activity<sup>92</sup>. Blakney *et al.* (2012) used an RGD-modified poly(ethylene glycol) hydrogel to demonstrate that stiffer gels upregulated pro-inflammatory cytokines in the presence of LPS, and stiffer gels implanted in mice resulted in a more severe foreign body response marked by extensive macrophage accumulation on the gel surface<sup>93</sup>. Previtiera *et al.* (2015) similarly found that substrate stiffness upregulated TLR4 expression (through which LPS signals), resulting in downstream secretion of cytokines like TNF- $\alpha$ <sup>94</sup>. In contrast, THP-1 monocytes reduced TNF- $\alpha$  expression on stiffer interpenetrating networks, whereas IL-8 secretion was biphasic<sup>95</sup>. This reverse trend of substrate stiffness modulation of TNF- $\alpha$  as a prototypical inflammatory cytokine has also been reported with polyacrylamide gels<sup>96</sup>. In 2D and 3D collagen matrices with modified stiffnesses via crosslinking, macrophages have variously been reported to adopt either inflammatory or anti-inflammatory phenotypes<sup>97-99</sup>.

A consistent finding among these studies is that macrophages become more spread and polarized on stiffer substrates as expected from other cell types. Similarly, macrophages stimulated with different cytokines may differentially regulate their morphology, raising the question of whether controlling cell morphology alone could regulate phenotype. Several studies have designed substrates that regulate macrophage shape via microcontact printing or microgrooves to achieve either a rounded or elongated morphology<sup>100</sup>. Using a micropatterning approach, McWhorter *et al.* (2013) found that forcing bone marrow derived macrophages into an elongated morphology induced polarization characterized by expression of arginase-1, CD206, and YM-1 and potentiated the actions of IL-4 and IL-13 (ref 101).

Other cell types generally demonstrate durotaxis, or migration along stiffness gradients. Studies with macrophages are less conclusive, either showing little or no preference, or durotaxis against the gradient with simultaneous LPS treatment<sup>92,102</sup>. The composition and topology of the ECM is likely to play a bigger role in the migration

mode adopted by macrophages (i.e. amoeboid vs. mesenchymal)<sup>103</sup>. Yet, an interesting correlation between the relatively high rigidity of the invasive front of breast cancer and macrophage accumulation has been observed, although the physical underpinnings that drive this process are unclear<sup>104</sup>.

Mechanistic understanding of the role of substrate stiffness in macrophage phenotype is somewhat lacking in these studies, although important effectors of focal adhesion regulation have been implicated such as various integrins, class A macrophage scavenger receptor (SR-A), FAK, Rac GTPases, and components of the actomyosin contractile apparatus<sup>100</sup>. Macrophage podosomes (focal adhesion-like structures) have, similar to other cells, been shown to be mechanosensitive elements that regulate their stiffness according to substrate stiffness as a result of actomyosin contraction and mechanosensitive focal adhesion proteins talin, vinculin, and paxillin<sup>105,106</sup>. Although the molecular components of podosomes are largely similar to focal adhesions, the architecture differs: focal adhesion proteins form a ring around actin binding proteins (e.g. Arp2/3) and an F-actin core, which exerts protrusive normal forces rather than tangential forces. It is likely through mechanosensitive podosomes and involvement of PI3K, RhoA, and myosin II that macrophage traction forces scale with substrate stiffness in a “frontal-towing” leading edge dependent manner during 2D migration<sup>107</sup>. In 3D environments, macrophages adopting a mesenchymal mode of migration develop podosomes more akin to protease-dependent invadosomes seen with invasive cancer cells, and improper podosome formation is associated with a reduced ability of macrophages to degrade and migrate through matrices<sup>103,108,109</sup>. The ability of podosomes to degrade the ECM is a result of secretion of various proteases including membrane type MMPs (MT-MMPs), ADAMs (a disintegrin and metalloproteinase), serine and cysteine proteases, and the plasmin activation system<sup>110</sup>. However, macrophages adopting an amoeboid-type mode of migration in more porous matrices depend instead on Rho/ROCK signaling with less dependence on integrins<sup>103</sup>.

In general, integrin expression and regulation dictates cell adhesion, spreading, focal adhesion structure, and downstream signaling. In leukocytes, various low affinity integrins are expressed that become conformationally activated by inflammatory signals as well as outside-in signaling, leading to rolling on the endothelium, arrest, and transmigration. The  $\beta_1$  integrins bind primarily to ECM proteins whereas  $\beta_2$



integrins primarily bind cell adhesion molecules important for cell-cell adhesion<sup>111</sup>. Monocyte-derived macrophages undergo differentiation that results in a pattern of integrin expression unique from naïve monocytes and monocyte-derived dendritic cells<sup>112,113</sup>. The role of integrins in determining macrophage phenotype is often studied in context of the development of an inflammatory transcriptional program, as it is essential to the function of the innate immune system. Recognition of LPS, or endotoxin, is also a major function of macrophages in order to identify bacterial pathogens, and integrin signaling synergy with LPS response is often a focus. LPS is a pathogen associated molecular pattern (PAMP) that signals through pattern recognition receptors (PRRs) such as TLR4. Engagement of integrins has long been known to induce secretion of inflammatory cytokines, and leukocyte adhesion to tissue culture plastic is sufficient for induction of inflammatory responses such as the release of IL-1 $\beta$ <sup>114,115</sup>, and the response to LPS is dependent on integrin engagement<sup>116</sup>.

The inflammatory response due to integrin binding may be a result of the promiscuity of integrin dimers – the  $\alpha_M\beta_2$  integrin (CD11b/CD18; Mac1) expressed on myeloid cells, for example, doubles as a PRR for complement proteins and several other ligands<sup>117</sup>. The integrin  $\alpha_V\beta_3$  (CD51/CD61), which binds vitronectin and fibronectin, similarly stimulates pro-inflammatory cytokine mRNA expression via induction of NF- $\kappa$ B in macrophages and synergizes with the response to LPS<sup>118</sup>. It was subsequently shown that expression of  $\alpha_V\beta_3$  increases upon LPS stimulation and dependent on TLR4 activation<sup>119</sup>. Blakney *et al.* (2012) observed that  $\alpha_V$  expression was increased in macrophages on stiffer PEG-RGD gels and suggested that this was a major component of macrophage substrate stiffness mechanosensing<sup>93</sup>. LPS also regulates expression of  $\beta_1$  integrin pairs<sup>120</sup> and activation of  $\beta_2$  integrins via small GTPases Rap1 and R-ras<sup>121</sup>. Rap1 activation is common to several inside-out signaling pathways that induce high affinity states of  $\alpha_L\beta_2$  (CD11a/CD18) and  $\alpha_4\beta_1$  (VLA4; CD49d/CD29)<sup>122</sup>. Other TLRs and their ligands are mediators of integrin activation and cell adhesion through inside-out signaling<sup>123,124</sup>. Induction of a classically activated inflammatory state is therefore associated with increased integrin expression and enhanced adhesion on various substrates<sup>125</sup>.

Bidirectional communication between integrins and TLRs, in which integrin signaling regulates TLR pathways, may also exist, although the association is less clear with  $\alpha_M$  engagement shown to either inhibit or synergize with the TLR4 pathway<sup>126-130</sup>. Of

these, more recent studies support a role for  $\alpha_M$  and  $\beta_2$  integrins in degrading components of the TLR pathway as a negative feedback mechanism, probably due to a more refined understanding of primary cell type subsets. Although loss of  $\beta_2$  integrins may enhance TLR-dependent inflammatory responses in this manner, *in vivo* knockout or genetic mutations of  $\beta_2$  integrins in leukocytes without any other autoimmune or disease state has the overall effect of impairing innate immunity, understandably due to the inability of PMNs in particular to migrate and be recruited to injured tissue. However, the effect of inhibiting  $\beta_2$  from bone marrow derived mononuclear cells under non-homeostatic conditions is less clear<sup>131</sup>. Such studies provide suggestive evidence that macrophage substrate stiffness sensing involves integrins, which may modulate inflammatory cytokine secretion, expression of PRRs, or both.

Some insights on the biomechanical properties of the cells themselves come from studies investigating the effects of cholesterol on monocyte membrane mechanics in context of atherosclerosis: cholesterol depletion decreases membrane deformability (increases tension), which induces cell spreading, polarization, and actin polymerization<sup>132</sup>. Cholesterol depletion also increased monocyte interactions with E-selectin surfaces and reduced cell velocity of monocyte rolling<sup>133</sup>. For adherent cells, there is a causal relationship between substrate stiffness and membrane tension and a relationship between membrane tension and inflammatory activity. Indeed, the membrane Young's modulus of monocytes increases upon differentiation to macrophages, and treatment with LPS or IFN- $\gamma$  further increases membrane stiffness<sup>134</sup>. Further, macrophage phagocytic rate can be modulated by altering membrane stiffness via substrate stiffness, LPS/IFN- $\gamma$  treatment, or both<sup>96</sup>.

A lack of consensus in some of these studies – in particular how substrate stiffness polarizes macrophages – is likely due to differences between macrophage cell types (i.e. cell line, murine bone marrow derived, human peripheral blood), mechanistic differences in 2D and 3D *in vitro* systems, the contribution of ECM type and architecture independent of stiffness, and the synergistic or antagonistic role of exogenous stimulants or cytokines.

## 1.5 Use of tamoxifen in PDAC

Our group has previously explored the use of tamoxifen, an estrogen receptor (ER) antagonist typically used in breast cancer treatment, as a potential adjuvant for PDAC\*. Tamoxifen has demonstrated anti-fibrotic and anti-inflammatory properties in various cancerous and non-cancerous conditions<sup>135-139</sup>, perhaps indicating a more general mechanism in which tamoxifen reprograms tissue unrelated to the dysregulated estrogen signaling in breast cancer. The ability of tamoxifen to reduce fibrosis is of particular interest to strategies for therapeutic targeting of the stroma. Although still contentious, normalizing stromal mechanics and reducing the abundant ECM may improve chemotherapy. Thus, tamoxifen was studied as a drug candidate intended to target the stroma and ameliorate the fibroinflammatory reaction.

Indeed, we find that tamoxifen can act through the G-protein coupled receptor (GPER; GPR30) to inhibit RhoA activity, p-MLC, YAP mechanotransduction, and cell actomyosin contraction in PSCs. As a result, PSCs are unable to adopt a contractile myofibroblast phenotype, which reduces cell stiffness, traction forces, their ability to contract matrices, mechanically activate TGF- $\beta$ , and reduces overall stiffness of organotypic gels and tissue in a mouse model of PDAC. Concurrently, tamoxifen reduces expression of hypoxia inducible factor-1 $\alpha$  (HIF-1 $\alpha$ ), a “master regulator” of the tumor and metastatic microenvironment via the lysyl oxidase (LOX) family of collagen crosslinkers<sup>140,141</sup>. As a result, tamoxifen-treated mice that develop PDAC express less tissue level HIF-1 $\alpha$ , LOX-L2, MMP-2, and overall ECM (collagen, fibronectin) proteins. The level of tissue hypoxia, a hallmark feature of PDAC, is also markedly reduced with tamoxifen (**Figure 1-5**). The expression of GPER is furthermore reduced in mouse tissues (**Figure 1-6**), and in human patients, high GPER-expressing tumors demonstrate significantly improved survival, indicating a role for GPER signaling in suppressing tumor aggressiveness.

---

\* Unpublished data:

Cortes E, Robinson E, Sarper M, Lachowski D, Teppo J, Thorpe S, Lieberthal T. J., Iwamoto K., Karim S., Haining A. W., Chronopoulos A., Lee D., Okada-Hatakeyama M., Varjosalo M., Morton J., & Del Rio Hernandez, A. Tamoxifen mechanically reprograms the tumor microenvironment and the survival of cancer cells via HIF-1A.

Cortes E., Sarper M., Robinson B., Chronopoulos A., Lachowski D., Attwood S., Haining A. W., Karim S., Lieberthal T. J., Morton J., & Del Rio Hernandez, A. GPER: A mechano-regulator of pancreatic stellate cells and the tumor microenvironment.

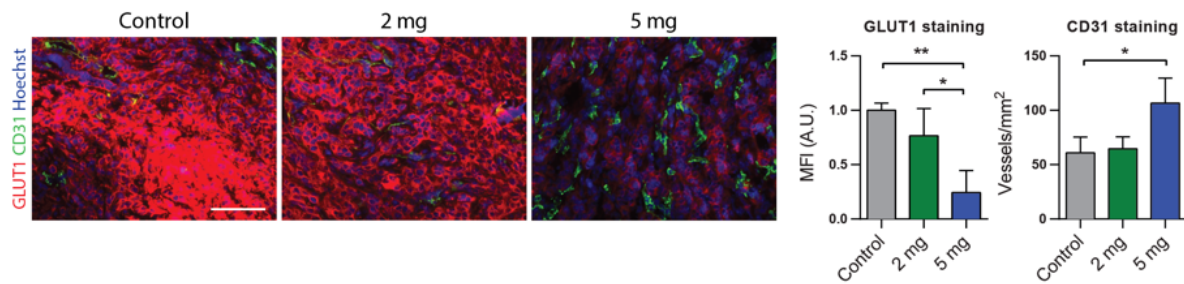


**Figure 1-5.** Tamoxifen reduces hypoxia and increases blood vessel density in a KPC mouse model of pancreatic cancer. Immunofluorescence images of PDAC tissues from KPC mice treated with vehicle control, and 2 mg, and 5 mg of tamoxifen, scale bar 100  $\mu$ m. GLUT1 is a hypoxia marker and CD31 (endothelial cell marker) indicates blood vessels. Bars represent mean  $\pm$  SEM (n = 3).

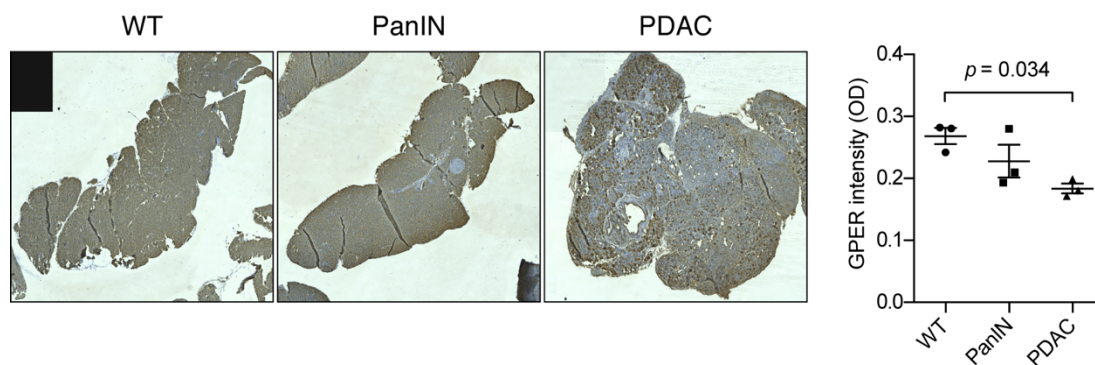


**Figure 1-6.** Low magnification (tiled 10x) immunohistochemistry staining of GPER in wild type (WT), PanIN (precursor lesions), and PDAC mouse tissues (n=3). Positive staining is indicated by brown precipitate. Nuclei are counterstained with hematoxylin (blue).

This evidence suggests that tamoxifen can target the PSCs in a mechanically-dependent manner – by inhibiting their ability to sense mechanical cues via actomyosin – inducing a more quiescent homeostatic phenotype, leading to a reduction in the appearance of a characteristic fibrotic PDAC stroma. On-going investigations will determine if such stromal reprogramming with tamoxifen or a specific GPER agonist, paired with a first line chemotherapeutic treatment, can have clinical/translational value. Additionally, the existence of other GPER-expressing stromal cells suggests that tamoxifen or a GPER agonist may act more generally to regulate cell mechanics within the stromal compartment.

### 1.5.1 Research questions and hypotheses

Given evidence supporting a role for matrix stiffening in regulation of both epithelia and stromal fibroblasts and the observation that macrophages are responsive to substrate stiffness, it is likely that macrophages undergo a similar transformation in

which substrate stiffness regulates the immunophenotype relevant to cancer; specifically, the composition and mechanics of the tumor stroma ECM could mediate a switch to an immunosuppressive polarized tumor-associated macrophage and enhance migration into the peritumoral area. Accordingly, drugs that target the mechanics of stromal cells, such as tamoxifen, may also regulate macrophage phenotype in the tumor microenvironment. Therefore, in **Chapter 2**, we explored the use of tamoxifen to regulate macrophage mechanics and the molecular basis therein. We hypothesize that substrate stiffness regulation of macrophages can be overcome by tamoxifen and such intervention beneficially polarizes macrophages in the tumor microenvironment. In **Chapter 3**, in order to further investigate biomechanical changes of macrophages, a microfluidic cell adhesion strength device was built.

## 1.6 PDAC biomarkers and diagnostics

As described in **Section 1.2 Outlook**, PDAC is uniformly lethal due to low incidence, early metastasis, lack of presenting symptoms, and lack of early detection. In this section, the current state of PDAC biomarkers and new opportunities for engineered solutions are discussed. Work in this area is presented in **Chapter 4**.

### 1.6.1 Current biomarkers

Currently there is a dearth of PDAC biomarkers that achieve the necessary sensitivity and specificity required for accurate diagnosis. The “gold standard” for PDAC diagnosis is a fine needle aspiration biopsy of the tissue following CT or other imaging tests. This requires a subjective histological evaluation of the tissue by a pathologist and has yet to be automated by machine learning algorithms. Thus, the diagnosis of PDAC is often made on a qualitative basis after the patient presents with symptoms, which likely indicates not only the presence of fully formed neoplastic lesions, but likely metastatic colonies as well. The only biomarker used clinically, although infrequently, is the serum carbohydrate CA19-9, which has a sensitivity and specificity of 79-81% and 82-90%, respectively, and a low positive predictive value of 0.5-0.9% (ref 142).

Other biomarker or prognostic indicators currently under development include circulating nucleic acids<sup>143,144</sup>, ratios of immune cell populations<sup>145</sup>, and circulating proteins<sup>146</sup>. Circulating tumor cells can also be isolated from the blood as a biomarker<sup>147</sup>, yet circulating tumor cells are a very rare cell population and difficult to

isolate. Furthermore, their presence likely already indicates later stage metastasis by which time the survival rate is greatly reduced.

### 1.6.2 Extracellular vesicles in PDAC

A new class of biomarkers called extracellular vesicles, which includes exosomes and microvesicles, has attracted interest recently. Exosomes are ~40-150 nm vesicles of endosomal origin that are shed from all cell types and present in all biofluids<sup>148</sup>. Although once considered debris due to their small size, molecular analysis of exosomes revealed that they constitute a discrete population of vesicles with protein cargo reflecting its unique biogenesis that distinguishes them from directly budded vesicles or membrane fragments<sup>149</sup>. Exosome biogenesis begins with inward invagination of the plasma membrane, leading to an early endosome. With the help of endosomal sorting complex required for transport (ESCRT) proteins, intraluminal vesicles (ILVs) form a multivesicular body (MVB). At the formation of MVB stage, exosomal cargo – including proteins and nucleic acids – can be incorporated into the ILVs. ESCRT machinery and their accessory proteins (e.g. ALIX), along with tetraspanins (e.g. CD63 and CD81) that facilitate selection of cargo, are frequently used as protein markers to identify exosomes<sup>150,151</sup>. ESCRT-independent mechanisms of MVB formation also exist<sup>152</sup>. MVBs may fuse with lysosomes, leading to degradation of components, or they can be trafficked to the plasma membrane via interactions with the cytoskeleton and regulated by RAB family of small GTPase proteins. Once transported to the cell membrane, MVBs can fuse with the membrane to release exosomes extracellularly, and this depends on the formation of a SNARE complex<sup>153</sup>. The exosome biogenesis pathway is depicted in **Figure 1-7**.

Exosomes are a valuable source of information because they can contain hundreds of internal and membrane proteins as well as nucleic acids which can be transferred to other cells in a paracrine-like manner. Their role in healthy cells and normal physiology is largely unknown; they may facilitate cellular waste removal<sup>154</sup> or ejection of misfolded proteins and degraded RNA<sup>155,156</sup>. Cells generally increase exosome secretion in response to stress (e.g. chemotherapy, hypoxia), supporting a role for exosomes in waste removal and potentially paracrine communication of a perturbed physiological state<sup>153</sup>. In cancer, exosomes appear mostly to promote the diseased phenotype by dampening the immune response<sup>157,158</sup>, promoting angiogenesis<sup>159</sup>, preparing pre-metastatic niche environments<sup>160-163</sup>, and disseminating metastatic

behavior via “phenocopying”<sup>164,165</sup>. These functions of exosomes are a result of protein and RNA cargo that are protected from degradation in circulation. Incredibly, various forms of RNA carried by exosomes can be transmitted to distant cells to modulate target cell transcription<sup>166-168</sup>.

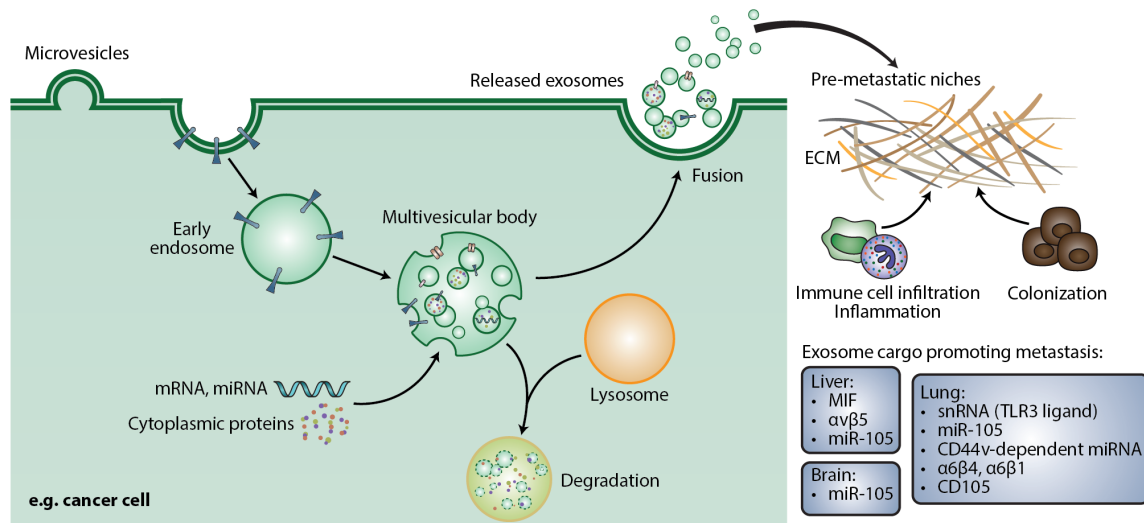


**Figure 1-7.** Exosome biogenesis. Exosomes are distinguished from microvesicles, which bud directly from the membrane and are larger in diameter (>200 nm). Cargo (proteins, nucleic acids) are known to promote distant tissue microenvironments conducive to metastatic colonization. Reprinted from Chronopoulos A, Lieberthal TJ, and del Rio Hernandez A. *Converg. Sci. Phys. Oncol.* 2017; 3, 013005 (ref 169) with permission.

Costa-Silva *et al.* (2015) described how pancreatic cancer exosomes prepare a pre-metastatic niche in the liver through a cascade of activated liver cells that is initiated by macrophage inflammatory factor (MIF)-expressing exosomes<sup>160</sup>. Kupffer cells, a type of resident liver macrophage, scavenge tumor-derived exosomes and secrete TGF- $\beta$ , which activates hepatic stellate cells, initiates bone marrow-derived myeloid cell infiltration, and develops a pre-fibrotic environment conducive to circulating tumor cell establishment and colonization. Accordingly, exosomes from a more aggressive pancreatic cancer cell line enhance the inflammatory niche in the liver<sup>170</sup>. Circulating monocytes may clear blood-borne exosomes by phagocytosis, potentially limiting their dissemination, but this is dependent on expression of CD47 on exosomes<sup>171</sup>. Several mechanisms in which extracellular vesicles are taken up have been identified, such as clathrin-dependent and -independent endocytosis, micropinocytosis, and phagocytosis<sup>172</sup>. Hoshino *et al.* (2015) went further to describe the exosomal integrins involved in organotropic metastasis:  $\alpha 6 \beta 4$  and  $\alpha 6 \beta 1$  integrins direct lung metastasis, whereas  $\alpha v \beta 5$  directs liver metastasis<sup>162</sup>.

Extracellular vesicles can also regulate behavior within the primary tumor microenvironment. Pancreatic fibroblast exosomes have been implicated in stroma-tumor signaling, leading to altered metabolism and cancer cell survival<sup>173,174</sup>. Interestingly, cancer associated fibroblasts accelerate vesicle secretion as a mechanism of chemoresistance<sup>173</sup>. Alternatively, pancreatic cancer-derived microvesicles carrying miR-155 may communicate in the reverse direction to modulate the behavior of fibroblasts and the maintenance of the tumor microenvironment<sup>175</sup>. Exosomes thus represent a therapeutic target for inhibiting primary tumor growth or limiting metastasis. Their apparent ability to retain bioactivity in circulation and acquire organotropism also opens avenues for engineering exosomes for drug delivery; for example, to carry shRNA or siRNA against KRAS<sup>G12D</sup> (ref 171).

Because exosomes are abundant in biofluids ( $>10^9$ /mL whole blood<sup>176</sup>) and information dense, they are an excellent candidate as a biomarker. Circulating exosomal DNA carrying driver mutations (KRAS<sup>G12D</sup> and TP53<sup>R273H</sup>) have been detected in PDAC patients with higher sensitivity than detection of mutant KRAS from cell free DNA<sup>177,178</sup>. A study by Melo *et al.* (2015) showed that exosomal glypican-1 detects PDAC with absolute (100%) sensitivity and specificity<sup>179</sup>. The 100% specificity is essential to prevent false-positive results, due to the low incidence rates in the general population. Furthermore, exosome derived glypican-1 was present in the blood of mice with early PDAC tumors, and the concentration of exosomal glypican-1 scaled with disease progression. However, subsequent studies did not find the same sensitivity as reported by Melo *et al.*, instead finding that either exosomal miRNAs or combinations of surface proteins were superior biomarkers<sup>180,181</sup>. Nevertheless, accumulating evidence has demonstrated that extracellular vesicles play an important role in cancer progression and hold potential as early stage biomarkers.

Unfortunately, extracellular vesicles can be difficult to isolate, which limits the utility of glypican-1, any other membrane proteins, or internal protein or RNA cargo found within circulating exosomes. Because of their small size, exosomes must be isolated from whole blood using high speed ultracentrifugation, which requires 4-6 hours to complete after which a low yield of exosomes (5-25%) can be recovered<sup>182</sup>. Additional steps such as 0.22  $\mu$ m filtration, flotation on a sucrose gradient, and size exclusion chromatography are also recommended in addition to centrifugation to purify exosomes<sup>183</sup>. However, a recent study discouraged use of ultracentrifugation in



exosome research due to aggregation of vesicles which may bias quantitative measurements and potentially affect exosome function<sup>184</sup>. Several other studies have found that commercial exosome isolation kits such as ExoQuick (System Biosciences) also trap significant protein contaminants<sup>185-188</sup>. Furthermore, ultracentrifugation requires specialized equipment that may be inaccessible to clinical facilities and other resource poor settings. There is therefore a need for an easy-to-use low cost device that can separate and detect extracellular vesicles as a platform for early non-invasive detection of PDAC.

### 1.6.3 Engineered solutions for extracellular vesicle diagnostics

The recent interest in extracellular vesicles as propagators of cancer and as blood-borne biomarkers – along with the technical difficulties in vesicle isolation – has attracted the interest of engineers. In the past 5 years, lab on a chip (LOC) and microelectromechanical systems (MEMS) devices have been deployed to address the insufficiencies of conventional techniques. This has taken the form of devices that perform one or all of the following functions: separation, purification, concentration, and/or detection of vesicle membrane proteins or intravesicular proteins and nucleic acids. Currently, methods to isolate extracellular vesicles include immunoaffinity capture, filtration, magnetic (with beads), deterministic lateral displacement, and manipulation of microfluidic flows. Detection methods range from fluorescence, colorimetry, surface plasmon resonance, micro nuclear magnetic resonance ( $\mu$ NMR), and electrochemistry. A detailed list of such devices is tabulated in **Table 2**.

A main design specification in the fabrication of such devices is the level of autonomy and the extent to which the sample or device are pre- or post-processed. Ideally, a point-of-care device should require minimal pre-processing of the sample and allow for direct on-chip measurements. Many current microfluidic devices require prior isolation of exosomes, pre-labeling of exosomes with magnetic nanoparticles or beads to remove them from biofluids, or perform just one function (isolation or detection) only. In general, it is desirable to allow label free detection of the analyte in which detection does not rely on a labeled nano/microparticle or fluorescently labeled secondary antibody.

A device that accomplishes the overall goal of detecting a cancer-associated biomarker must furthermore be designed with recognition of the complexity and scarcity of the biofluid, the difficulty of operating the device, and any expected

downstream applications of the sample. Crucially, the sensitivity and specificity of the sensor must also be maximized in consideration with these other factors. Further design considerations are discussed in **Chapter 4** where we introduce acoustophoresis for vesicle isolation and a graphene field effect transistor for extracellular vesicle detection.

**Table 2.** Comprehensive list of devices used to separate/purify and/or detect extracellular vesicles. Only devices that contain microfluidic or LOC elements are included. Published work on variations of established methods (e.g. SPR) are not included, nor are novel imaging technologies. No method of purification may be denoted in cases where the detection element is said to carry out simultaneous purification (e.g. immunoaffinity capture). Unless otherwise indicated, separation parameter refers to the extracellular vesicles. This tabulation represents publications prior to Dec 2017. \*Indicates of particular interest to this thesis.

Year	Method of isolation	Separation parameter	Method detection	of	Marker detected	Citation
2010	Immunoaffinity	Protein specificity	Fluorescence		Membrane protein	Chen, et al. <i>Lab Chip</i> . 2010; 10, 505-511 (ref 189).
2012	Nanoporous membrane	Size	-		-	Davies, et al. <i>Lab Chip</i> . 2012; 12, 5202-5210 (ref 190).
2012	Membrane filtration	Size	Magnetic nanoparticles and $\mu$ NMR		Membrane protein	Shao, et al. <i>Nat Med</i> . 2012; 18, 1835-1840 (ref 191).
2013	Membrane filtration	Size	Magnetic nanoparticles and $\mu$ NMR		Membrane protein	Rho, et al. <i>ACS Nano</i> . 2013; 7, 11227-11233 (ref 192).
2013	Ciliated micropillars	Size	-		-	Wang, et al. <i>Lab Chip</i> . 2013; 13, 2879-2882 (ref 193).
2014	Immunoaffinity	Protein specificity	Fluorescence		Membrane protein	Kanwar, et al. <i>Lab Chip</i> . 2014; 14, 1891-1900 (ref 194).
2014	Immunomagnetic	Protein specificity	Chemi-fluorescence		Intravesicular protein	He, et al. <i>Lab Chip</i> . 2014; 14, 3773-3780 (ref 195).
2014	-	-	SPR		Membrane protein	Im, et al. <i>Nat Biotechnol</i> . 2014; 32, 490-495 (ref 196).
2014	-	-	SPR		Membrane protein	Zhu, et al. <i>Anal Chem</i> . 2014; 86, 8857-8864 (ref 197).
2014	Nanoshearing-enhanced immunoaffinity	Protein specificity	Colormetric		Membrane protein	Vaidyanathan, et al. <i>Anal Chem</i> . 2014; 86, 11125-11132 (ref 198).
2014	Deterministic lateral displacement	Size	-		-	Santana, et al. <i>Biomed Microdevices</i> . 2014; 16, 869-877 (ref 199).
* 2015	Acoustophoresis	Size	-		-	Lee, et al. <i>ACS Nano</i> . 2015; 9, 2321-2327 (ref 200).

2015	Inertial lift	Bead size	On-chip cytometry	flow	Membrane protein	Dudani, et al. <i>Biomicrofluidics</i> . 2015; 9, 014112 (ref 201).
2015	-	-	Electrophoresis		Zeta potential	Akagi, et al. <i>PLoS One</i> . 2015; 10, e0123603 (ref 202).
* 2015	Surface acoustic wave lysis of vesicles	-	Ion-exchange nanosensor		Intravesicular RNA	Taller, et al. <i>Lab Chip</i> . 2015; 15, 1656-1666 (ref 203).
2015	Immunomagnetic separation	Protein specificity	PCR of lysed RNA adsorbed to glass beads		Intravesicular RNA	Shao, et al. <i>Nat Commun</i> . 2015; 6, 6999 (ref 204).
2016	Immunomagnetic separation	Protein specificity	Electrochemical		Membrane protein	Jeong, et al. <i>ACS Nano</i> . 2016; 10, 1802-1809 (ref 205).
2016	-	-	Fluorogenic ELISA		Membrane protein	Zhang, et al. <i>Lab Chip</i> . 2016; 16, 3033-3042 (ref 206).
2016	Nanoscale deterministic lateral displacement	Size	-		-	Wunsch, et al. <i>Nat Nanotechnol</i> . 2016; 11, 936-940 (ref 207).
2016	Immunoaffinity (magnetic beads)	Protein specificity	Fluorescence		Membrane protein	Zhao, et al. <i>Lab Chip</i> . 2016; 16, 489-496 (ref 208).
2016	Electrophoretic migration through membrane	Size	-		-	Cho, et al. <i>Sens. Actuators B Chem</i> . 2016; 233, 289-297 (ref 209).
2016	Membrane filtration	Bead size	Fluorescence		Membrane protein	Ko, et al. <i>Sci Rep</i> . 2016; 6, 31215 (ref 210).
2017	Electrokinesis	Dielectric properties	Fluorescence		Membrane and intravesicular RNA	Ibsen, et al. <i>ACS Nano</i> . 2017; 11, 6641-6651 (ref 211).
2017	Filtration	Size	-		-	Liu, et al. <i>ACS Nano</i> . 2017; 11, 10712-10723 (ref 212).
2017	Pinched flow fractionation	Size	-		-	Shin, et al. <i>Sci Rep</i> . 2017; 7, 9907 (ref 213).
2017	Capture/release immunoaffinity	Protein specificity	Fluorescence		Membrane protein	Kang, et al. <i>Nanoscale</i> . 2017; 9, 13495-13505 (ref 214).
* 2017	Acoustophoresis	Size	-		-	Wu, et al. <i>Proc Natl Acad Sci U S A</i> . 2017; 114, 10584-10589 (ref 215).
2017	Elastic lift	Size	-		-	Liu, et al. <i>ACS Nano</i> . 2017; 11, 6968-6976 (ref 216).
* 2017	-	-	SPR		Membrane protein	Yang, et al. <i>Sci Transl Med</i> . 2017; 9 (ref 181).
2017	-	-	TIRF fluorescence		Intravesicular RNA	Hu, et al. <i>Nat Commun</i> . 2017; 8, 1683 (ref 217).
2017	Filtration	Size	Colorimetric		Membrane protein	Liang, et al. <i>Sci Rep</i> . 2017; 7, 46224 (ref 218).

2017	-	-	Fluorescence	Membrane protein	Ishihara, et al. <i>ACS Omega</i> . 2017; 2, 6703-6707 (ref 219).
2017	Magnetic nanoparticles	Protein specificity	Fluorescence	Membrane protein	Fang, et al. <i>PLoS One</i> . 2017; 12, e0175050 (ref 220).

## 1.7 References

- Hallet, J., Law, C. H., Cukier, M., Saskin, R., Liu, N. & Singh, S. Exploring the rising incidence of neuroendocrine tumors: a population-based analysis of epidemiology, metastatic presentation, and outcomes. *Cancer*. 2015; 121, 589-597.
- Cancer Research UK. *Pancreatic Cancer Statistics*, <<http://www.cancerresearchuk.org/health-professional/cancer-statistics/statistics-by-cancer-type/pancreatic-cancer>> (2015). Accessed Nov 2017.
- Gold, E. B. & Goldin, S. B. Epidemiology of and risk factors for pancreatic cancer. *Surg Oncol Clin N Am*. 1998; 7, 67-91.
- Klein, A. P., Brune, K. A., Petersen, G. M., Goggins, M., Tersmette, A. C., Offerhaus, G. J., Griffin, C., Cameron, J. L., Yeo, C. J., Kern, S. & Hruban, R. H. Prospective risk of pancreatic cancer in familial pancreatic cancer kindreds. *Cancer Res*. 2004; 64, 2634-2638.
- Distler, M., Aust, D., Weitz, J., Pilarsky, C. & Grutzmann, R. Precursor lesions for sporadic pancreatic cancer: PanIN, IPMN, and MCN. *Biomed Res Int*. 2014; 2014, 474905.
- McPherson, R. A., Henry, J. B., McPherson, R. A., Pincus, M. R. & Abraham, N. Z. (2011). *Henry's clinical diagnosis and management by laboratory methods* (22th ed.). Philadelphia: Elsevier/Saunders.
- Ying, H., Dey, P., Yao, W., Kimmelman, A. C., Draetta, G. F., Maitra, A. & DePinho, R. A. Genetics and biology of pancreatic ductal adenocarcinoma. *Genes Dev*. 2016; 30, 355-385.
- Makohon-Moore, A. P., Zhang, M., Reiter, J. G., Bozic, I., Allen, B., Kundu, D., Chatterjee, K., Wong, F., Jiao, Y., Kohutek, Z. A., Hong, J., Attiyeh, M., Javier, B., Wood, L. D., Hruban, R. H., Nowak, M. A., Papadopoulos, N., Kinzler, K. W., Vogelstein, B. & Iacobuzio-Donahue, C. A. Limited heterogeneity of known driver gene mutations among the metastases of individual patients with pancreatic cancer. *Nat Genet*. 2017; 49, 358-366.
- Samuel, N. & Hudson, T. J. The molecular and cellular heterogeneity of pancreatic ductal adenocarcinoma. *Nat Rev Gastroenterol Hepatol*. 2011; 9, 77-87.
- Sipos, B., Frank, S., Gress, T., Hahn, S. & Kloppel, G. Pancreatic intraepithelial neoplasia revisited and updated. *Pancreatol*. 2009; 9, 45-54.
- Townsend, C. M., Jr., Beauchamp, R. D., Evers, B. M. & Mattox, K. L. (2012). *Sabiston Textbook of Surgery: The Biological Basis of Modern Surgical Practice* (19th ed.). London: Elsevier Health Sciences.
- Conroy, T., Desseigne, F., Ychou, M., Bouche, O., Guimbaud, R., Becouarn, Y., Adenis, A., Raoul, J. L., Gourgou-Bourgade, S., de la Fouchardiere, C., Bennouna, J., Bachet, J. B., Khemissa-Akouz, F., Pere-Verge, D., Delbaldo, C., Assenat, E., Chauffert, B., Michel, P., Montoto-Grillot, C., Ducreux, M., Groupe Tumeurs Digestives of, U. & Intergroup, P. FOLFIRINOX versus gemcitabine for metastatic pancreatic cancer. *N Engl J Med*. 2011; 364, 1817-1825.

- 13 Von Hoff, D. D., Ervin, T., Arena, F. P., Chiorean, E. G., Infante, J., Moore, M., Seay, T., Tjulandin, S. A., Ma, W. W., Saleh, M. N., Harris, M., Reni, M., Dowden, S., Laheru, D., Bahary, N., Ramanathan, R. K., Taberero, J., Hidalgo, M., Goldstein, D., Van Cutsem, E., Wei, X., Iglesias, J. & Renschler, M. F. Increased survival in pancreatic cancer with nab-paclitaxel plus gemcitabine. *N Engl J Med.* 2013; 369, 1691-1703.
- 14 Quaresma, M., Coleman, M. P. & Rachet, B. 40-year trends in an index of survival for all cancers combined and survival adjusted for age and sex for each cancer in England and Wales, 1971-2011: a population-based study. *Lancet.* 2015; 385, 1206-1218.
- 15 Rahib, L., Smith, B. D., Aizenberg, R., Rosenzweig, A. B., Fleshman, J. M. & Matrisian, L. M. Projecting cancer incidence and deaths to 2030: the unexpected burden of thyroid, liver, and pancreas cancers in the United States. *Cancer Res.* 2014; 74, 2913-2921.
- 16 Crist, D. W., Sitzmann, J. V. & Cameron, J. L. Improved hospital morbidity, mortality, and survival after the Whipple procedure. *Ann Surg.* 1987; 206, 358-365.
- 17 Rhim, A. D., Mirek, E. T., Aiello, N. M., Maitra, A., Bailey, J. M., McAllister, F., Reichert, M., Beatty, G. L., Rustgi, A. K., Vonderheide, R. H., Leach, S. D. & Stanger, B. Z. EMT and dissemination precede pancreatic tumor formation. *Cell.* 2012; 148, 349-361.
- 18 Chung, W. J., Daemen, A., Cheng, J. H., Long, J. E., Cooper, J. E., Wang, B. E., Tran, C., Singh, M., Gnad, F., Modrusan, Z., Foreman, O. & Junttila, M. R. Kras mutant genetically engineered mouse models of human cancers are genomically heterogeneous. *Proc Natl Acad Sci U S A.* 2017.
- 19 Campbell, P. J., Yachida, S., Mudie, L. J., Stephens, P. J., Pleasance, E. D., Stebbings, L. A., Morsberger, L. A., Latimer, C., McLaren, S., Lin, M. L., McBride, D. J., Varela, I., Nik-Zainal, S. A., Leroy, C., Jia, M., Menzies, A., Butler, A. P., Teague, J. W., Griffin, C. A., Burton, J., Swerdlow, H., Quail, M. A., Stratton, M. R., Iacobuzio-Donahue, C. & Futreal, P. A. The patterns and dynamics of genomic instability in metastatic pancreatic cancer. *Nature.* 2010; 467, 1109-1113.
- 20 Witkiewicz, A. K., Balaji, U., Eslinger, C., McMillan, E., Conway, W., Posner, B., Mills, G. B., O'Reilly, E. M. & Knudsen, E. S. Integrated Patient-Derived Models Delineate Individualized Therapeutic Vulnerabilities of Pancreatic Cancer. *Cell Rep.* 2016; 16, 2017-2031.
- 21 Recavarren, C., Labow, D. M., Liang, J., Zhang, L., Wong, M., Zhu, H., Wang, J., Francis, F. & Xu, R. Histologic characteristics of pancreatic intraepithelial neoplasia associated with different pancreatic lesions. *Hum Pathol.* 2011; 42, 18-24.
- 22 Jansen, K. A., Donato, D. M., Balcioglu, H. E., Schmidt, T., Danen, E. H. & Koenderink, G. H. A guide to mechanobiology: Where biology and physics meet. *Biochim Biophys Acta.* 2015; 1853, 3043-3052.
- 23 del Rio, A., Perez-Jimenez, R., Liu, R., Roca-Cusachs, P., Fernandez, J. M. & Sheetz, M. P. Stretching single talin rod molecules activates vinculin binding. *Science.* 2009; 323, 638-641.
- 24 Mohri, Z., Del Rio Hernandez, A. & Krams, R. The emerging role of YAP/TAZ in mechanotransduction. *J Thorac Dis.* 2017; 9, E507-E509.
- 25 Dvorak, H. F. Tumors: wounds that do not heal. Similarities between tumor stroma generation and wound healing. *N Engl J Med.* 1986; 315, 1650-1659.
- 26 Dvorak, H. F. Tumors: wounds that do not heal-redux. *Cancer Immunol Res.* 2015; 3, 1-11.
- 27 Apte, M. V., Haber, P. S., Applegate, T. L., Norton, I. D., McCaughan, G. W., Korsten, M. A., Pirola, R. C. & Wilson, J. S. Periacinar stellate shaped cells in rat pancreas: identification, isolation, and culture. *Gut.* 1998; 43, 128-133.

- 28 Apte, M. V. & Wilson, J. S. Dangerous liaisons: pancreatic stellate cells and pancreatic cancer cells. *J Gastroenterol Hepatol*. 2012; 27 Suppl 2, 69-74.
- 29 Watari, N., Hotta, Y. & Mabuchi, Y. Morphological studies on a vitamin A-storing cell and its complex with macrophage observed in mouse pancreatic tissues following excess vitamin A administration. *Okajimas Folia Anat Jpn*. 1982; 58, 837-858.
- 30 Apte, M. V., Park, S., Phillips, P. A., Santucci, N., Goldstein, D., Kumar, R. K., Ramm, G. A., Buchler, M., Friess, H., McCarroll, J. A., Keogh, G., Merrett, N., Pirola, R. & Wilson, J. S. Desmoplastic reaction in pancreatic cancer: role of pancreatic stellate cells. *Pancreas*. 2004; 29, 179-187.
- 31 Pothula, S. P., Xu, Z., Goldstein, D., Pirola, R. C., Wilson, J. S. & Apte, M. V. Key role of pancreatic stellate cells in pancreatic cancer. *Cancer Lett*. 2016; 381, 194-200.
- 32 Tomasek, J. J., Gabbiani, G., Hinz, B., Chaponnier, C. & Brown, R. A. Myofibroblasts and mechano-regulation of connective tissue remodelling. *Nat Rev Mol Cell Biol*. 2002; 3, 349-363.
- 33 Chronopoulos, A., Lieberthal, T. J. & del Río Hernández, A. E. Pancreatic cancer: a mechanobiology approach. *Converg Sci Phys Oncol*. 2017; 3, 013001.
- 34 Neesse, A., Michl, P., Frese, K. K., Feig, C., Cook, N., Jacobetz, M. A., Lolkema, M. P., Buchholz, M., Olive, K. P., Gress, T. M. & Tuveson, D. A. Stromal biology and therapy in pancreatic cancer. *Gut*. 2011; 60, 861-868.
- 35 Ozdemir, B. C., Pentcheva-Hoang, T., Carstens, J. L., Zheng, X., Wu, C. C., Simpson, T. R., Laklai, H., Sugimoto, H., Kahlert, C., Novitskiy, S. V., De Jesus-Acosta, A., Sharma, P., Heidari, P., Mahmood, U., Chin, L., Moses, H. L., Weaver, V. M., Maitra, A., Allison, J. P., LeBleu, V. S. & Kalluri, R. Depletion of carcinoma-associated fibroblasts and fibrosis induces immunosuppression and accelerates pancreas cancer with reduced survival. *Cancer Cell*. 2014; 25, 719-734.
- 36 Rhim, A. D., Oberstein, P. E., Thomas, D. H., Mirek, E. T., Palermo, C. F., Sastra, S. A., Dekleva, E. N., Saunders, T., Becerra, C. P., Tattersall, I. W., Westphalen, C. B., Kitajewski, J., Fernandez-Barrena, M. G., Fernandez-Zapico, M. E., Iacobuzio-Donahue, C., Olive, K. P. & Stanger, B. Z. Stromal elements act to restrain, rather than support, pancreatic ductal adenocarcinoma. *Cancer Cell*. 2014; 25, 735-747.
- 37 Bramhall, S. R., Schulz, J., Nemunaitis, J., Brown, P. D., Baillet, M. & Buckels, J. A. A double-blind placebo-controlled, randomised study comparing gemcitabine and marimastat with gemcitabine and placebo as first line therapy in patients with advanced pancreatic cancer. *Br J Cancer*. 2002; 87, 161-167.
- 38 Moore, M. J., Hamm, J., Dancey, J., Eisenberg, P. D., Dagenais, M., Fields, A., Hagan, K., Greenberg, B., Colwell, B., Zee, B., Tu, D., Ottaway, J., Humphrey, R., Seymour, L. & National Cancer Institute of Canada Clinical Trials, G. Comparison of gemcitabine versus the matrix metalloproteinase inhibitor BAY 12-9566 in patients with advanced or metastatic adenocarcinoma of the pancreas: a phase III trial of the National Cancer Institute of Canada Clinical Trials Group. *J Clin Oncol*. 2003; 21, 3296-3302.
- 39 Paszek, M. J., Zahir, N., Johnson, K. R., Lakins, J. N., Rozenberg, G. I., Gefen, A., Reinhart-King, C. A., Margulies, S. S., Dembo, M., Boettiger, D., Hammer, D. A. & Weaver, V. M. Tensional homeostasis and the malignant phenotype. *Cancer Cell*. 2005; 8, 241-254.
- 40 Chaudhuri, O., Koshy, S. T., Branco da Cunha, C., Shin, J. W., Verbeke, C. S., Allison, K. H. & Mooney, D. J. Extracellular matrix stiffness and composition jointly regulate the induction of malignant phenotypes in mammary epithelium. *Nat Mater*. 2014; 13, 970-978.

- 41 Levental, K. R., Yu, H., Kass, L., Lakins, J. N., Egeblad, M., Erler, J. T., Fong, S. F., Csiszar, K., Giaccia, A., Weninger, W., Yamauchi, M., Gasser, D. L. & Weaver, V. M. Matrix crosslinking forces tumor progression by enhancing integrin signaling. *Cell*. 2009; 139, 891-906.
- 42 Miller, B. W., Morton, J. P., Pinese, M., Saturno, G., Jamieson, N. B., McGhee, E., Timpson, P., Leach, J., McGarry, L., Shanks, E., Bailey, P., Chang, D., Oien, K., Karim, S., Au, A., Steele, C., Carter, C. R., McKay, C., Anderson, K., Evans, T. R., Marais, R., Springer, C., Biankin, A., Erler, J. T. & Sansom, O. J. Targeting the LOX/hypoxia axis reverses many of the features that make pancreatic cancer deadly: inhibition of LOX abrogates metastasis and enhances drug efficacy. *EMBO Mol Med*. 2015; 7, 1063-1076.
- 43 Provenzano, P. P., Eliceiri, K. W., Campbell, J. M., Inman, D. R., White, J. G. & Keely, P. J. Collagen reorganization at the tumor-stromal interface facilitates local invasion. *BMC Med*. 2006; 4, 38.
- 44 Olive, K. P., Jacobetz, M. A., Davidson, C. J., Gopinathan, A., McIntyre, D., Honess, D., Madhu, B., Goldgraben, M. A., Caldwell, M. E., Allard, D., Frese, K. K., Denicola, G., Feig, C., Combs, C., Winter, S. P., Ireland-Zecchini, H., Reichelt, S., Howat, W. J., Chang, A., Dhara, M., Wang, L., Ruckert, F., Grutzmann, R., Pilarsky, C., Izeradjene, K., Hingorani, S. R., Huang, P., Davies, S. E., Plunkett, W., Egorin, M., Hruban, R. H., Whitebread, N., McGovern, K., Adams, J., Iacobuzio-Donahue, C., Griffiths, J. & Tuveson, D. A. Inhibition of Hedgehog signaling enhances delivery of chemotherapy in a mouse model of pancreatic cancer. *Science*. 2009; 324, 1457-1461.
- 45 Hingorani, S. R., Petricoin, E. F., Maitra, A., Rajapakse, V., King, C., Jacobetz, M. A., Ross, S., Conrads, T. P., Veenstra, T. D., Hitt, B. A., Kawaguchi, Y., Johann, D., Liotta, L. A., Crawford, H. C., Putt, M. E., Jacks, T., Wright, C. V., Hruban, R. H., Lowy, A. M. & Tuveson, D. A. Preinvasive and invasive ductal pancreatic cancer and its early detection in the mouse. *Cancer Cell*. 2003; 4, 437-450.
- 46 Hingorani, S. R., Wang, L., Multani, A. S., Combs, C., Deramaudt, T. B., Hruban, R. H., Rustgi, A. K., Chang, S. & Tuveson, D. A. Trp53R172H and KrasG12D cooperate to promote chromosomal instability and widely metastatic pancreatic ductal adenocarcinoma in mice. *Cancer Cell*. 2005; 7, 469-483.
- 47 Beatty, G. L., Chiorean, E. G., Fishman, M. P., Saboury, B., Teitelbaum, U. R., Sun, W., Huhn, R. D., Song, W., Li, D., Sharp, L. L., Torigian, D. A., O'Dwyer, P. J. & Vonderheide, R. H. CD40 agonists alter tumor stroma and show efficacy against pancreatic carcinoma in mice and humans. *Science*. 2011; 331, 1612-1616.
- 48 Samuel, M. S., Lopez, J. I., McGhee, E. J., Croft, D. R., Strachan, D., Timpson, P., Munro, J., Schroder, E., Zhou, J., Brunton, V. G., Barker, N., Clevers, H., Sansom, O. J., Anderson, K. I., Weaver, V. M. & Olson, M. F. Actomyosin-mediated cellular tension drives increased tissue stiffness and beta-catenin activation to induce epidermal hyperplasia and tumor growth. *Cancer Cell*. 2011; 19, 776-791.
- 49 Provenzano, P. P., Cuevas, C., Chang, A. E., Goel, V. K., Von Hoff, D. D. & Hingorani, S. R. Enzymatic targeting of the stroma ablates physical barriers to treatment of pancreatic ductal adenocarcinoma. *Cancer Cell*. 2012; 21, 418-429.
- 50 Lee, J. J., Perera, R. M., Wang, H., Wu, D. C., Liu, X. S., Han, S., Fitamant, J., Jones, P. D., Ghanta, K. S., Kawano, S., Nagle, J. M., Deshpande, V., Boucher, Y., Kato, T., Chen, J. K., Willmann, J. K., Bardeesy, N. & Beachy, P. A. Stromal response to Hedgehog signaling restrains pancreatic cancer progression. *Proc Natl Acad Sci U S A*. 2014; 111, E3091-3100.
- 51 Sherman, M. H., Yu, R. T., Engle, D. D., Ding, N., Atkins, A. R., Tiriach, H., Collisson, E. A., Connor, F., Van Dyke, T., Kozlov, S., Martin, P., Tseng, T. W., Dawson, D. W., Donahue, T. R., Masamune, A., Shimosegawa, T., Apte, M. V., Wilson, J. S., Ng, B., Lau, S. L., Gunton, J. E., Wahl, G. M., Hunter, T., Drebin, J. A., O'Dwyer, P. J., Liddle, C., Tuveson, D. A., Downes,

- M. & Evans, R. M. Vitamin D receptor-mediated stromal reprogramming suppresses pancreatitis and enhances pancreatic cancer therapy. *Cell*. 2014; 159, 80-93.
- 52 Laklai, H., Miroshnikova, Y. A., Pickup, M. W., Collisson, E. A., Kim, G. E., Barrett, A. S., Hill, R. C., Lakins, J. N., Schlaepfer, D. D., Mouw, J. K., LeBleu, V. S., Roy, N., Novitskiy, S. V., Johansen, J. S., Poli, V., Kalluri, R., Iacobuzio-Donahue, C. A., Wood, L. D., Hebrok, M., Hansen, K., Moses, H. L. & Weaver, V. M. Genotype tunes pancreatic ductal adenocarcinoma tissue tension to induce matricellular fibrosis and tumor progression. *Nat Med*. 2016; 22, 497-505.
- 53 Jiang, H., Hegde, S., Knolhoff, B. L., Zhu, Y., Herndon, J. M., Meyer, M. A., Nywening, T. M., Hawkins, W. G., Shapiro, I. M., Weaver, D. T., Pachter, J. A., Wang-Gillam, A. & DeNardo, D. G. Targeting focal adhesion kinase renders pancreatic cancers responsive to checkpoint immunotherapy. *Nat Med*. 2016; 22, 851-860.
- 54 Vennin, C., Chin, V. T., Warren, S. C., Lucas, M. C., Herrmann, D., Magenau, A., Melenec, P., Walters, S. N., Del Monte-Nieto, G., Conway, J. R., Nobis, M., Allam, A. H., McCloy, R. A., Currey, N., Pinese, M., Boulghourjian, A., Zaratzian, A., Adam, A. A., Heu, C., Nagrial, A. M., Chou, A., Steinmann, A., Drury, A., Froio, D., Giry-Laterriere, M., Harris, N. L., Phan, T., Jain, R., Weninger, W., McGhee, E. J., Whan, R., Johns, A. L., Samra, J. S., Chantrell, L., Gill, A. J., Kohonen-Corish, M., Harvey, R. P., Biankin, A. V., Australian Pancreatic Cancer Genome, I., Evans, T. R., Anderson, K. I., Grey, S. T., Ormandy, C. J., Gallego-Ortega, D., Wang, Y., Samuel, M. S., Sansom, O. J., Burgess, A., Cox, T. R., Morton, J. P., Pajic, M. & Timpson, P. Transient tissue priming via ROCK inhibition uncouples pancreatic cancer progression, sensitivity to chemotherapy, and metastasis. *Sci Transl Med*. 2017; 9.
- 55 Yauch, R. L., Gould, S. E., Scales, S. J., Tang, T., Tian, H., Ahn, C. P., Marshall, D., Fu, L., Januario, T., Kallop, D., Nannini-Pepe, M., Kotkow, K., Marsters, J. C., Rubin, L. L. & de Sauvage, F. J. A paracrine requirement for hedgehog signalling in cancer. *Nature*. 2008; 455, 406-410.
- 56 Bailey, J. M., Swanson, B. J., Hamada, T., Eggers, J. P., Singh, P. K., Caffery, T., Ouellette, M. M. & Hollingsworth, M. A. Sonic hedgehog promotes desmoplasia in pancreatic cancer. *Clin Cancer Res*. 2008; 14, 5995-6004.
- 57 Kim, E. J., Sahai, V., Abel, E. V., Griffith, K. A., Greenson, J. K., Takebe, N., Khan, G. N., Blau, J. L., Craig, R., Balis, U. G., Zalupski, M. M. & Simeone, D. M. Pilot clinical trial of hedgehog pathway inhibitor GDC-0449 (vismodegib) in combination with gemcitabine in patients with metastatic pancreatic adenocarcinoma. *Clin Cancer Res*. 2014; 20, 5937-5945.
- 58 Catenacci, D. V., Junttila, M. R., Karrison, T., Bahary, N., Horiba, M. N., Nattam, S. R., Marsh, R., Wallace, J., Kozloff, M., Rajdev, L., Cohen, D., Wade, J., Sleckman, B., Lenz, H. J., Stiff, P., Kumar, P., Xu, P., Henderson, L., Takebe, N., Salgia, R., Wang, X., Stadler, W. M., de Sauvage, F. J. & Kindler, H. L. Randomized Phase Ib/II Study of Gemcitabine Plus Placebo or Vismodegib, a Hedgehog Pathway Inhibitor, in Patients With Metastatic Pancreatic Cancer. *J Clin Oncol*. 2015; 33, 4284-4292.
- 59 Amakye, D., Jagani, Z. & Dorsch, M. Unraveling the therapeutic potential of the Hedgehog pathway in cancer. *Nat Med*. 2013; 19, 1410-1422.
- 60 Gore, J. & Korc, M. Pancreatic cancer stroma: friend or foe?; *Cancer Cell*. 2014; 25, 711-712.
- 61 Chauhan, V. P., Boucher, Y., Ferrone, C. R., Roberge, S., Martin, J. D., Stylianopoulos, T., Bardeesy, N., DePinho, R. A., Padera, T. P., Munn, L. L. & Jain, R. K. Compression of pancreatic tumor blood vessels by hyaluronan is caused by solid stress and not interstitial fluid pressure. *Cancer Cell*. 2014; 26, 14-15.
- 62 Whatcott, C. J., Han, H., Posner, R. G., Hostetter, G. & Von Hoff, D. D. Targeting the tumor microenvironment in cancer: why hyaluronidase deserves a second look. *Cancer Discov*. 2011; 1, 291-296.



- 63 Jacobetz, M. A., Chan, D. S., Neesse, A., Bapiro, T. E., Cook, N., Frese, K. K., Feig, C., Nakagawa, T., Caldwell, M. E., Zecchini, H. I., Lolkema, M. P., Jiang, P., Kultti, A., Thompson, C. B., Maneval, D. C., Jodrell, D. I., Frost, G. I., Shepard, H. M., Skepper, J. N. & Tuveson, D. A. Hyaluronan impairs vascular function and drug delivery in a mouse model of pancreatic cancer. *Gut*. 2013; 62, 112-120.
- 64 Vennin, C., Cox, T. R., Pajic, M. & Timpson, P. Transient targeting of the pancreatic cancer stroma as a 'fine-tuned' anti-tumor and anti-metastatic therapy. *Oncotarget*. 2017; 8, 84635-84636.
- 65 Couzin-Frankel, J. Breakthrough of the year 2013. Cancer immunotherapy. *Science*. 2013; 342, 1432-1433.
- 66 Koh, T. J. & DiPietro, L. A. Inflammation and wound healing: the role of the macrophage. *Expert Rev Mol Med*. 2011; 13, e23.
- 67 Shalapour, S. & Karin, M. Immunity, inflammation, and cancer: an eternal fight between good and evil. *J Clin Invest*. 2015; 125, 3347-3355.
- 68 Houghton, A. N. & Guevara-Patino, J. A. Immune recognition of self in immunity against cancer. *J Clin Invest*. 2004; 114, 468-471.
- 69 Ferrante, C. J. & Leibovich, S. J. Regulation of Macrophage Polarization and Wound Healing. *Adv Wound Care (New Rochelle)*. 2012; 1, 10-16.
- 70 Mills, C. D., Kincaid, K., Alt, J. M., Heilman, M. J. & Hill, A. M. M-1/M-2 macrophages and the Th1/Th2 paradigm. *J Immunol*. 2000; 164, 6166-6173.
- 71 Mantovani, A., Sozzani, S., Locati, M., Allavena, P. & Sica, A. Macrophage polarization: tumor-associated macrophages as a paradigm for polarized M2 mononuclear phagocytes. *Trends Immunol*. 2002; 23, 549-555.
- 72 Helm, O., Held-Feindt, J., Grage-Griebenow, E., Reiling, N., Ungefroren, H., Vogel, I., Kruger, U., Becker, T., Ebsen, M., Rocken, C., Kabelitz, D., Schafer, H. & Sebens, S. Tumor-associated macrophages exhibit pro- and anti-inflammatory properties by which they impact on pancreatic tumorigenesis. *Int J Cancer*. 2014; 135, 843-861.
- 73 Martinez, F. O. & Gordon, S. The M1 and M2 paradigm of macrophage activation: time for reassessment. *F1000Prime Rep*. 2014; 6, 13.
- 74 Ginhoux, F., Schultze, J. L., Murray, P. J., Ochando, J. & Biswas, S. K. New insights into the multidimensional concept of macrophage ontogeny, activation and function. *Nat Immunol*. 2016; 17, 34-40.
- 75 Aras, S. & Zaidi, M. R. TAMEless traitors: macrophages in cancer progression and metastasis. *Br J Cancer*. 2017; 117, 1583-1591.
- 76 Nahrendorf, M. & Swirski, F. K. Abandoning M1/M2 for a Network Model of Macrophage Function. *Circ Res*. 2016; 119, 414-417.
- 77 Murray, P. J., Allen, J. E., Biswas, S. K., Fisher, E. A., Gilroy, D. W., Goerdt, S., Gordon, S., Hamilton, J. A., Ivashkiv, L. B., Lawrence, T., Locati, M., Mantovani, A., Martinez, F. O., Mege, J. L., Mosser, D. M., Natoli, G., Saeij, J. P., Schultze, J. L., Shirey, K. A., Sica, A., Suttles, J., Udalova, I., van Ginderachter, J. A., Vogel, S. N. & Wynn, T. A. Macrophage activation and polarization: nomenclature and experimental guidelines. *Immunity*. 2014; 41, 14-20.
- 78 Heppner, F. L., Ransohoff, R. M. & Becher, B. Immune attack: the role of inflammation in Alzheimer disease. *Nat Rev Neurosci*. 2015; 16, 358-372.

- 79 Helm, O., Held-Feindt, J., Schafer, H. & Sebens, S. M1 and M2: there is no "good" and "bad"- How macrophages promote malignancy-associated features in tumorigenesis. *Oncoimmunology*. 2014; 3, e946818.
- 80 Ino, Y., Yamazaki-Itoh, R., Shimada, K., Iwasaki, M., Kosuge, T., Kanai, Y. & Hiraoka, N. Immune cell infiltration as an indicator of the immune microenvironment of pancreatic cancer. *Br J Cancer*. 2013; 108, 914-923.
- 81 Nywening, T. M., Belt, B. A., Cullinan, D. R., Panni, R. Z., Han, B. J., Sanford, D. E., Jacobs, R. C., Ye, J., Patel, A. A., Gillanders, W. E., Fields, R. C., DeNardo, D. G., Hawkins, W. G., Goedegebuure, P. & Linehan, D. C. Targeting both tumour-associated CXCR2(+) neutrophils and CCR2(+) macrophages disrupts myeloid recruitment and improves chemotherapeutic responses in pancreatic ductal adenocarcinoma. *Gut*. 2017.
- 82 Kaneda, M. M., Cappello, P., Nguyen, A. V., Ralainirina, N., Hardamon, C. R., Foubert, P., Schmid, M. C., Sun, P., Mose, E., Bouvet, M., Lowy, A. M., Valasek, M. A., Sasik, R., Novelli, F., Hirsch, E. & Varner, J. A. Macrophage PI3Kgamma Drives Pancreatic Ductal Adenocarcinoma Progression. *Cancer Discov*. 2016; 6, 870-885.
- 83 Long, K. B., Gladney, W. L., Tooker, G. M., Graham, K., Fraietta, J. A. & Beatty, G. L. IFNgamma and CCL2 Cooperate to Redirect Tumor-Infiltrating Monocytes to Degrade Fibrosis and Enhance Chemotherapy Efficacy in Pancreatic Carcinoma. *Cancer Discov*. 2016; 6, 400-413.
- 84 Huse, M. Mechanical forces in the immune system. *Nat Rev Immunol*. 2017; 17, 679-690.
- 85 Basu, R., Whitlock, B. M., Husson, J., Le Floc'h, A., Jin, W., Oyler-Yaniv, A., Dotiwala, F., Giannone, G., Hivroz, C., Biais, N., Lieberman, J., Kam, L. C. & Huse, M. Cytotoxic T Cells Use Mechanical Force to Potentiate Target Cell Killing. *Cell*. 2016; 165, 100-110.
- 86 Li, J., Li, Y., Gao, B., Qin, C., He, Y., Xu, F., Yang, H. & Lin, M. Engineering mechanical microenvironment of macrophage and its biomedical applications. *Nanomedicine (Lond)*. 2018.
- 87 Pugin, J., Dunn, I., Jolliet, P., Tassaux, D., Magnenat, J. L., Nicod, L. P. & Chevrolet, J. C. Activation of human macrophages by mechanical ventilation in vitro. *Am J Physiol*. 1998; 275, L1040-1050.
- 88 Yang, J. H., Sakamoto, H., Xu, E. C. & Lee, R. T. Biomechanical regulation of human monocyte/macrophage molecular function. *Am J Pathol*. 2000; 156, 1797-1804.
- 89 Shiratsuch, H. & Basson, M. D. Differential regulation of monocyte/macrophage cytokine production by pressure. *Am J Surg*. 2005; 190, 757-762.
- 90 Oya, K., Sakamoto, N., Ohashi, T. & Sato, M. Combined stimulation with cyclic stretching and hypoxia increases production of matrix metalloproteinase-9 and cytokines by macrophages. *Biochem Biophys Res Commun*. 2011; 412, 678-682.
- 91 Matheson, L. A., Maksym, G. N., Santerre, J. P. & Labow, R. S. Cyclic biaxial strain affects U937 macrophage-like morphology and enzymatic activities. *J Biomed Mater Res A*. 2006; 76, 52-62.
- 92 Adlerz, K. M., Aranda-Espinoza, H. & Hayenga, H. N. Substrate elasticity regulates the behavior of human monocyte-derived macrophages. *Eur Biophys J*. 2016; 45, 301-309.
- 93 Blakney, A. K., Swartzlander, M. D. & Bryant, S. J. The effects of substrate stiffness on the in vitro activation of macrophages and in vivo host response to poly(ethylene glycol)-based hydrogels. *J Biomed Mater Res A*. 2012; 100, 1375-1386.
- 94 Previtera, M. L. & Sengupta, A. Substrate Stiffness Regulates Proinflammatory Mediator Production through TLR4 Activity in Macrophages. *PLoS One*. 2015; 10, e0145813.

- 95 Irwin, E. F., Saha, K., Rosenbluth, M., Gamble, L. J., Castner, D. G. & Healy, K. E. Modulus-dependent macrophage adhesion and behavior. *J Biomater Sci Polym Ed.* 2008; 19, 1363-1382.
- 96 Patel, N. R., Bole, M., Chen, C., Hardin, C. C., Kho, A. T., Mih, J., Deng, L., Butler, J., Tschumperlin, D., Fredberg, J. J., Krishnan, R. & Koziel, H. Cell elasticity determines macrophage function. *PLoS One.* 2012; 7, e41024.
- 97 Friedemann, M., Kalbitzer, L., Franz, S., Moeller, S., Schnabelrauch, M., Simon, J. C., Pompe, T. & Franke, K. Instructing Human Macrophage Polarization by Stiffness and Glycosaminoglycan Functionalization in 3D Collagen Networks. *Adv Healthc Mater.* 2017; 6.
- 98 Franz, S., Allenstein, F., Kajahn, J., Forstreuter, I., Hintze, V., Moller, S. & Simon, J. C. Artificial extracellular matrices composed of collagen I and high-sulfated hyaluronan promote phenotypic and functional modulation of human pro-inflammatory M1 macrophages. *Acta Biomater.* 2013; 9, 5621-5629.
- 99 Badylak, S. F., Valentin, J. E., Ravindra, A. K., McCabe, G. P. & Stewart-Akers, A. M. Macrophage phenotype as a determinant of biologic scaffold remodeling. *Tissue Eng Part A.* 2008; 14, 1835-1842.
- 100 McWhorter, F. Y., Davis, C. T. & Liu, W. F. Physical and mechanical regulation of macrophage phenotype and function. *Cell Mol Life Sci.* 2015; 72, 1303-1316.
- 101 McWhorter, F. Y., Wang, T., Nguyen, P., Chung, T. & Liu, W. F. Modulation of macrophage phenotype by cell shape. *Proc Natl Acad Sci U S A.* 2013; 110, 17253-17258.
- 102 Previtera, M. L., Peterman, K., Shah, S. & Luzuriaga, J. Lipid rafts direct macrophage motility in the tissue microenvironment. *Ann Biomed Eng.* 2015; 43, 896-905.
- 103 Van Goethem, E., Poincloux, R., Gauffre, F., Maridonneau-Parini, I. & Le Cabec, V. Matrix architecture dictates three-dimensional migration modes of human macrophages: differential involvement of proteases and podosome-like structures. *J Immunol.* 2010; 184, 1049-1061.
- 104 Acerbi, I., Cassereau, L., Dean, I., Shi, Q., Au, A., Park, C., Chen, Y. Y., Liphardt, J., Hwang, E. S. & Weaver, V. M. Human breast cancer invasion and aggression correlates with ECM stiffening and immune cell infiltration. *Integr Biol (Camb).* 2015; 7, 1120-1134.
- 105 Labernadie, A., Bouissou, A., Delobelle, P., Balor, S., Voituriez, R., Proag, A., Fourquaux, I., Thibault, C., Vieu, C., Poincloux, R., Charriere, G. M. & Maridonneau-Parini, I. Protrusion force microscopy reveals oscillatory force generation and mechanosensing activity of human macrophage podosomes. *Nat Commun.* 2014; 5, 5343.
- 106 Bouissou, A., Proag, A., Bourg, N., Pingris, K., Cabriel, C., Balor, S., Mangeat, T., Thibault, C., Vieu, C., Dupuis, G., Fort, E., Leveque-Fort, S., Maridonneau-Parini, I. & Poincloux, R. Podosome Force Generation Machinery: A Local Balance between Protrusion at the Core and Traction at the Ring. *ACS Nano.* 2017; 11, 4028-4040.
- 107 Hind, L. E., Dembo, M. & Hammer, D. A. Macrophage motility is driven by frontal-towing with a force magnitude dependent on substrate stiffness. *Integr Biol (Camb).* 2015; 7, 447-453.
- 108 Cougoule, C., Le Cabec, V., Poincloux, R., Al Saati, T., Mege, J. L., Tabouret, G., Lowell, C. A., Laviolette-Malirat, N. & Maridonneau-Parini, I. Three-dimensional migration of macrophages requires Hck for podosome organization and extracellular matrix proteolysis. *Blood.* 2010; 115, 1444-1452.
- 109 Guet, R., Verollet, C., Lamsoul, I., Cougoule, C., Poincloux, R., Labrousse, A., Calderwood, D. A., Glogauer, M., Lutz, P. G. & Maridonneau-Parini, I. Macrophage mesenchymal migration requires podosome stabilization by filamin A. *J Biol Chem.* 2012; 287, 13051-13062.

- 110 Wiesner, C., Le-Cabec, V., El Azzouzi, K., Maridonneau-Parini, I. & Linder, S. Podosomes in space: macrophage migration and matrix degradation in 2D and 3D settings. *Cell Adh Migr.* 2014; 8, 179-191.
- 111 Ruoslahti, E. Integrins. *J Clin Invest.* 1991; 87, 1-5.
- 112 Prieto, J., Eklund, A. & Patarroyo, M. Regulated expression of integrins and other adhesion molecules during differentiation of monocytes into macrophages. *Cell Immunol.* 1994; 156, 191-211.
- 113 Ammon, C., Meyer, S. P., Schwarzfischer, L., Krause, S. W., Andreesen, R. & Kreutz, M. Comparative analysis of integrin expression on monocyte-derived macrophages and monocyte-derived dendritic cells. *Immunology.* 2000; 100, 364-369.
- 114 Juliano, R. L. & Haskill, S. Signal transduction from the extracellular matrix. *J Cell Biol.* 1993; 120, 577-585.
- 115 Sporn, S. A., Eierman, D. F., Johnson, C. E., Morris, J., Martin, G., Ladner, M. & Haskill, S. Monocyte adherence results in selective induction of novel genes sharing homology with mediators of inflammation and tissue repair. *J Immunol.* 1990; 144, 4434-4441.
- 116 Monick, M. M., Powers, L., Butler, N., Yarovinsky, T. & Hunninghake, G. W. Interaction of matrix with integrin receptors is required for optimal LPS-induced MAP kinase activation. *Am J Physiol Lung Cell Mol Physiol.* 2002; 283, L390-402.
- 117 Hyun, Y. M., Lefort, C. T. & Kim, M. Leukocyte integrins and their ligand interactions. *Immunol Res.* 2009; 45, 195-208.
- 118 Antonov, A. S., Antonova, G. N., Munn, D. H., Mivechi, N., Lucas, R., Catravas, J. D. & Verin, A. D. alphaVbeta3 integrin regulates macrophage inflammatory responses via PI3 kinase/Akt-dependent NF-kappaB activation. *J Cell Physiol.* 2011; 226, 469-476.
- 119 Chen, Z., Ding, X., Jin, S., Pitt, B., Zhang, L., Billiar, T. & Li, Q. WISP1-alphaVbeta3 integrin signaling positively regulates TLR-triggered inflammation response in sepsis induced lung injury. *Sci Rep.* 2016; 6, 28841.
- 120 Kang, Y. H., Lee, C. H., Brummel, S. E., Newball, H. H. & Forrester, J. Effects of endotoxin on expression of VLA integrins by human bronchoalveolar lavage macrophages. *J Leukoc Biol.* 1995; 57, 624-634.
- 121 Caron, E., Self, A. J. & Hall, A. The GTPase Rap1 controls functional activation of macrophage integrin alphaMbeta2 by LPS and other inflammatory mediators. *Curr Biol.* 2000; 10, 974-978.
- 122 Imhof, B. A. & Aurrand-Lions, M. Adhesion mechanisms regulating the migration of monocytes. *Nat Rev Immunol.* 2004; 4, 432-444.
- 123 Bryant, C. E., Gay, N. J., Heymans, S., Sacre, S., Schaefer, L. & Midwood, K. S. Advances in Toll-like receptor biology: Modes of activation by diverse stimuli. *Crit Rev Biochem Mol Biol.* 2015; 50, 359-379.
- 124 Chung, K. J., Mitroulis, I., Wiessner, J. R., Zheng, Y. Y., Siegert, G., Sperandio, M. & Chavakis, T. A novel pathway of rapid TLR-triggered activation of integrin-dependent leukocyte adhesion that requires Rap1 GTPase. *Mol Biol Cell.* 2014; 25, 2948-2955.
- 125 Vereyken, E. J., Heijnen, P. D., Baron, W., de Vries, E. H., Dijkstra, C. D. & Teunissen, C. E. Classically and alternatively activated bone marrow derived macrophages differ in cytoskeletal functions and migration towards specific CNS cell types. *J Neuroinflammation.* 2011; 8, 58.

- 126 Han, C., Jin, J., Xu, S., Liu, H., Li, N. & Cao, X. Integrin CD11b negatively regulates TLR-triggered inflammatory responses by activating Syk and promoting degradation of MyD88 and TRIF via Cbl-b. *Nat Immunol.* 2010; 11, 734-742.
- 127 Perera, P. Y., Mayadas, T. N., Takeuchi, O., Akira, S., Zaks-Zilberman, M., Goyert, S. M. & Vogel, S. N. CD11b/CD18 acts in concert with CD14 and Toll-like receptor (TLR) 4 to elicit full lipopolysaccharide and taxol-inducible gene expression. *J Immunol.* 2001; 166, 574-581.
- 128 Ling, G. S., Bennett, J., Woollard, K. J., Szajna, M., Fossati-Jimack, L., Taylor, P. R., Scott, D., Franzoso, G., Cook, H. T. & Botto, M. Integrin CD11b positively regulates TLR4-induced signalling pathways in dendritic cells but not in macrophages. *Nat Commun.* 2014; 5, 3039.
- 129 Fan, S. T. & Edgington, T. S. Coupling of the adhesive receptor CD11b/CD18 to functional enhancement of effector macrophage tissue factor response. *J Clin Invest.* 1991; 87, 50-57.
- 130 Yee, N. K. & Hamerman, J. A. beta(2) integrins inhibit TLR responses by regulating NF-kappaB pathway and p38 MAPK activation. *Eur J Immunol.* 2013; 43, 779-792.
- 131 Schittenhelm, L., Hilkens, C. M. & Morrison, V. L. beta2 Integrins As Regulators of Dendritic Cell, Monocyte, and Macrophage Function. *Front Immunol.* 2017; 8, 1866.
- 132 Saha, A. K., Dallo, S. F., Detmar, A. L., Osmulski, P., Gaczynska, M., Huang, T. H. & Ramasubramanian, A. K. Cellular cholesterol regulates monocyte deformation. *J Biomech.* 2017; 52, 83-88.
- 133 Saha, A. K., Osmulski, P., Dallo, S. F., Gaczynska, M., Huang, T. H. & Ramasubramanian, A. K. Cholesterol Regulates Monocyte Rolling through CD44 Distribution. *Biophys J.* 2017; 112, 1481-1488.
- 134 Bufen, N., Saitakis, M., Dogniaux, S., Buschinger, O., Bohineust, A., Richert, A., Maurin, M., Hivroz, C. & Asnacios, A. Human Primary Immune Cells Exhibit Distinct Mechanical Properties that Are Modified by Inflammation. *Biophys J.* 2015; 108, 2181-2190.
- 135 Brandt, A. S., Kamper, L., Kukuk, S., Haage, P. & Roth, S. Tamoxifen monotherapy in the treatment of retroperitoneal fibrosis. *Urol Int.* 2014; 93, 320-325.
- 136 Hattar, R., Maller, O., McDaniel, S., Hansen, K. C., Hedman, K. J., Lyons, T. R., Lucia, S., Wilson, R. S., Jr. & Schedin, P. Tamoxifen induces pleiotrophic changes in mammary stroma resulting in extracellular matrix that suppresses transformed phenotypes. *Breast Cancer Res.* 2009; 11, R5.
- 137 Kim, D., Lee, A. S., Jung, Y. J., Yang, K. H., Lee, S., Park, S. K., Kim, W. & Kang, K. P. Tamoxifen ameliorates renal tubulointerstitial fibrosis by modulation of estrogen receptor alpha-mediated transforming growth factor-beta1/Smad signaling pathway. *Nephrol Dial Transplant.* 2014; 29, 2043-2053.
- 138 Kuhn, M. A., Wang, X., Payne, W. G., Ko, F. & Robson, M. C. Tamoxifen decreases fibroblast function and downregulates TGF(beta2) in Dupuytren's affected palmar fascia. *J Surg Res.* 2002; 103, 146-152.
- 139 Perez, B., Henriquez, C., Sarmiento, J., Morales, N., Folch, H., Galesio, J. S., Uberti, B. & Moran, G. Tamoxifen as a new therapeutic tool for neutrophilic lung inflammation. *Respirology.* 2016; 21, 112-118.
- 140 Wong, C. C., Gilkes, D. M., Zhang, H., Chen, J., Wei, H., Chaturvedi, P., Fraley, S. I., Wong, C. M., Khoo, U. S., Ng, I. O., Wirtz, D. & Semenza, G. L. Hypoxia-inducible factor 1 is a master regulator of breast cancer metastatic niche formation. *Proc Natl Acad Sci U S A.* 2011; 108, 16369-16374.

- 141 Pez, F., Dayan, F., Durivault, J., Kaniewski, B., Aimond, G., Le Provost, G. S., Deux, B., Clezardin, P., Sommer, P., Pouyssegur, J. & Reynaud, C. The HIF-1-inducible lysyl oxidase activates HIF-1 via the Akt pathway in a positive regulation loop and synergizes with HIF-1 in promoting tumor cell growth. *Cancer Res.* 2011; 71, 1647-1657.
- 142 Ballehaninna, U. K. & Chamberlain, R. S. The clinical utility of serum CA 19-9 in the diagnosis, prognosis and management of pancreatic adenocarcinoma: An evidence based appraisal. *J Gastrointest Oncol.* 2012; 3, 105-119.
- 143 Kishikawa, T., Otsuka, M., Ohno, M., Yoshikawa, T., Takata, A. & Koike, K. Circulating RNAs as new biomarkers for detecting pancreatic cancer. *World Journal of Gastroenterology.* 2015; 21, 8527-8540.
- 144 Vietsch, E. E., van Eijck, C. H. & Wellstein, A. Circulating DNA and Micro-RNA in Patients with Pancreatic Cancer. *Pancreat Disord Ther.* 2015; 5.
- 145 Bhatti, I., Peacock, O., Lloyd, G., Larvin, M. & Hall, R. I. Preoperative hematologic markers as independent predictors of prognosis in resected pancreatic ductal adenocarcinoma: neutrophil-lymphocyte versus platelet-lymphocyte ratio. *American Journal of Surgery.* 2010; 200, 197-203.
- 146 Fong, Z. V. & Winter, J. M. Biomarkers in pancreatic cancer: diagnostic, prognostic, and predictive. *Cancer J.* 2012; 18, 530-538.
- 147 Tjensvoll, K., Nordgard, O. & Smaaland, R. Circulating tumor cells in pancreatic cancer patients: methods of detection and clinical implications. *Int J Cancer.* 2014; 134, 1-8.
- 148 Kalluri, R. The biology and function of exosomes in cancer. *J Clin Invest.* 2016; 126, 1208-1215.
- 149 Thery, C., Boussac, M., Veron, P., Ricciardi-Castagnoli, P., Raposo, G., Garin, J. & Amigorena, S. Proteomic analysis of dendritic cell-derived exosomes: a secreted subcellular compartment distinct from apoptotic vesicles. *J Immunol.* 2001; 166, 7309-7318.
- 150 Thery, C., Amigorena, S., Raposo, G. & Clayton, A. Isolation and characterization of exosomes from cell culture supernatants and biological fluids. *Curr Protoc Cell Biol.* 2006; Chapter 3, Unit 3 22.
- 151 Kowal, J., Tkach, M. & Thery, C. Biogenesis and secretion of exosomes. *Curr Opin Cell Biol.* 2014; 29, 116-125.
- 152 Stuffers, S., Sem Wegner, C., Stenmark, H. & Brech, A. Multivesicular endosome biogenesis in the absence of ESCRTs. *Traffic.* 2009; 10, 925-937.
- 153 Hessvik, N. P. & Llorente, A. Current knowledge on exosome biogenesis and release. *Cell Mol Life Sci.* 2018; 75, 193-208.
- 154 Harding, C., Heuser, J. & Stahl, P. Endocytosis and intracellular processing of transferrin and colloidal gold-transferrin in rat reticulocytes: demonstration of a pathway for receptor shedding. *Eur J Cell Biol.* 1984; 35, 256-263.
- 155 van Balkom, B. W., Eisele, A. S., Pegtel, D. M., Bervoets, S. & Verhaar, M. C. Quantitative and qualitative analysis of small RNAs in human endothelial cells and exosomes provides insights into localized RNA processing, degradation and sorting. *J Extracell Vesicles.* 2015; 4, 26760.
- 156 Guo, B. B., Bellingham, S. A. & Hill, A. F. The neutral sphingomyelinase pathway regulates packaging of the prion protein into exosomes. *J Biol Chem.* 2015; 290, 3455-3467.

- 157 Andreola, G., Rivoltini, L., Castelli, C., Huber, V., Perego, P., Deho, P., Squarcina, P., Accornero, P., Lozupone, F., Lugini, L., Stringaro, A., Molinari, A., Arancia, G., Gentile, M., Parmiani, G. & Fais, S. Induction of lymphocyte apoptosis by tumor cell secretion of FasL-bearing microvesicles. *J Exp Med.* 2002; 195, 1303-1316.
- 158 Valenti, R., Huber, V., Iero, M., Filipazzi, P., Parmiani, G. & Rivoltini, L. Tumor-released microvesicles as vehicles of immunosuppression. *Cancer Research.* 2007; 67, 2912-2915.
- 159 Skog, J., Wurdinger, T., van Rijn, S., Meijer, D. H., Gainche, L., Sena-Estevés, M., Curry, W. T., Jr., Carter, B. S., Krichevsky, A. M. & Breakefield, X. O. Glioblastoma microvesicles transport RNA and proteins that promote tumour growth and provide diagnostic biomarkers. *Nat Cell Biol.* 2008; 10, 1470-1476.
- 160 Costa-Silva, B., Aiello, N. M., Ocean, A. J., Singh, S., Zhang, H., Thakur, B. K., Becker, A., Hoshino, A., Mark, M. T., Molina, H., Xiang, J., Zhang, T., Theilen, T. M., Garcia-Santos, G., Williams, C., Ararso, Y., Huang, Y., Rodrigues, G., Shen, T. L., Latori, K. J., Lothe, I. M., Kure, E. H., Hernandez, J., Doussot, A., Ebbesen, S. H., Grandgenett, P. M., Hollingsworth, M. A., Jain, M., Mallya, K., Batra, S. K., Jarnagin, W. R., Schwartz, R. E., Matei, I., Peinado, H., Stanger, B. Z., Bromberg, J. & Lyden, D. Pancreatic cancer exosomes initiate pre-metastatic niche formation in the liver. *Nat Cell Biol.* 2015; 17, 816-826.
- 161 Peinado, H., Aleckovic, M., Lavotshkin, S., Matei, I., Costa-Silva, B., Moreno-Bueno, G., Hergueta-Redondo, M., Williams, C., Garcia-Santos, G., Ghajar, C. M., Nitadori-Hoshino, A., Hoffman, C., Badal, K., Garcia, B. A., Callahan, M. K., Yuan, J. D., Martins, V. R., Skog, J., Kaplan, R. N., Brady, M. S., Wolchok, J. D., Chapman, P. B., Kang, Y. B., Bromberg, J. & Lyden, D. Melanoma exosomes educate bone marrow progenitor cells toward a pro-metastatic phenotype through MET. *Nature Medicine.* 2012; 18, 883-+.
- 162 Hoshino, A., Costa-Silva, B., Shen, T. L., Rodrigues, G., Hashimoto, A., Tesic Mark, M., Molina, H., Kohsaka, S., Di Giannatale, A., Ceder, S., Singh, S., Williams, C., Slop, N., Uryu, K., Pharmed, L., King, T., Bojmar, L., Davies, A. E., Ararso, Y., Zhang, T., Zhang, H., Hernandez, J., Weiss, J. M., Dumont-Cole, V. D., Kramer, K., Wexler, L. H., Narendran, A., Schwartz, G. K., Healey, J. H., Sandstrom, P., Latori, K. J., Kure, E. H., Grandgenett, P. M., Hollingsworth, M. A., de Sousa, M., Kaur, S., Jain, M., Mallya, K., Batra, S. K., Jarnagin, W. R., Brady, M. S., Fodstad, O., Muller, V., Pantel, K., Minn, A. J., Bissell, M. J., Garcia, B. A., Kang, Y., Rajasekhar, V. K., Ghajar, C. M., Matei, I., Peinado, H., Bromberg, J. & Lyden, D. Tumour exosome integrins determine organotropic metastasis. *Nature.* 2015; 527, 329-335.
- 163 Hood, J. L., San, R. S. & Wickline, S. A. Exosomes released by melanoma cells prepare sentinel lymph nodes for tumor metastasis. *Cancer Res.* 2011; 71, 3792-3801.
- 164 Zomer, A., Maynard, C., Verweij, F. J., Kamermans, A., Schafer, R., Beerling, E., Schiffelers, R. M., de Wit, E., Berenguer, J., Ellenbroek, S. I., Wurdinger, T., Pegtel, D. M. & van Rheeën, J. In Vivo imaging reveals extracellular vesicle-mediated phenocopying of metastatic behavior. *Cell.* 2015; 161, 1046-1057.
- 165 Al-Nedawi, K., Meehan, B., Micallef, J., Lhotak, V., May, L., Guha, A. & Rak, J. Intercellular transfer of the oncogenic receptor EGFRvIII by microvesicles derived from tumour cells. *Nat Cell Biol.* 2008; 10, 619-624.
- 166 Valadi, H., Ekstrom, K., Bossios, A., Sjostrand, M., Lee, J. J. & Lotvall, J. O. Exosome-mediated transfer of mRNAs and microRNAs is a novel mechanism of genetic exchange between cells. *Nat Cell Biol.* 2007; 9, 654-659.
- 167 Melo, S. A., Sugimoto, H., O'Connell, J. T., Kato, N., Villanueva, A., Vidal, A., Qiu, L., Vitkin, E., Perelman, L. T., Melo, C. A., Lucci, A., Ivan, C., Calin, G. A. & Kalluri, R. Cancer exosomes perform cell-independent microRNA biogenesis and promote tumorigenesis. *Cancer Cell.* 2014; 26, 707-721.

- 168 Deregibus, M. C., Cantaluppi, V., Calogero, R., Lo Iacono, M., Tetta, C., Biancone, L., Bruno, S., Bussolati, B. & Camussi, G. Endothelial progenitor cell derived microvesicles activate an angiogenic program in endothelial cells by a horizontal transfer of mRNA. *Blood*. 2007; 110, 2440-2448.
- 169 Chronopoulos, A., Lieberthal, T. J. & del Río Hernández, A. E. Exosomes as a platform for 'liquid biopsy' in pancreatic cancer. *Converg Sci Phys Oncol*. 2017; 3, 013005.
- 170 Yu, Z., Zhao, S., Ren, L., Wang, L., Chen, Z., Hoffman, R. M. & Zhou, J. Pancreatic cancer-derived exosomes promote tumor metastasis and liver pre-metastatic niche formation. *Oncotarget*. 2017; 8, 63461-63483.
- 171 Kamekar, S., LeBleu, V. S., Sugimoto, H., Yang, S., Ruivo, C. F., Melo, S. A., Lee, J. J. & Kalluri, R. Exosomes facilitate therapeutic targeting of oncogenic KRAS in pancreatic cancer. *Nature*. 2017; 546, 498-503.
- 172 Mulcahy, L. A., Pink, R. C. & Carter, D. R. Routes and mechanisms of extracellular vesicle uptake. *J Extracell Vesicles*. 2014; 3.
- 173 Richards, K. E., Zeleniak, A. E., Fishel, M. L., Wu, J., Littlepage, L. E. & Hill, R. Cancer-associated fibroblast exosomes regulate survival and proliferation of pancreatic cancer cells. *Oncogene*. 2017; 36, 1770-1778.
- 174 Zhao, H., Yang, L., Baddour, J., Achreja, A., Bernard, V., Moss, T., Marini, J. C., Tudawe, T., Seviour, E. G., San Lucas, F. A., Alvarez, H., Gupta, S., Maiti, S. N., Cooper, L., Peehl, D., Ram, P. T., Maitra, A. & Nagrath, D. Tumor microenvironment derived exosomes pleiotropically modulate cancer cell metabolism. *Elife*. 2016; 5, e10250.
- 175 Pang, W., Su, J., Wang, Y., Feng, H., Dai, X., Yuan, Y., Chen, X. & Yao, W. Pancreatic cancer-secreted miR-155 implicates in the conversion from normal fibroblasts to cancer-associated fibroblasts. *Cancer Sci*. 2015; 106, 1362-1369.
- 176 He, M. & Zeng, Y. Microfluidic Exosome Analysis toward Liquid Biopsy for Cancer. *J Lab Autom*. 2016; 21, 599-608.
- 177 Yang, S., Che, S. P., Kurywchak, P., Tavormina, J. L., Gansmo, L. B., Correa de Sampaio, P., Tachezy, M., Bockhorn, M., Gebauer, F., Haltom, A. R., Melo, S. A., LeBleu, V. S. & Kalluri, R. Detection of mutant KRAS and TP53 DNA in circulating exosomes from healthy individuals and patients with pancreatic cancer. *Cancer Biol Ther*. 2017; 18, 158-165.
- 178 Allenson, K., Castillo, J., San Lucas, F. A., Scelo, G., Kim, D. U., Bernard, V., Davis, G., Kumar, T., Katz, M., Overman, M. J., Foretova, L., Fabianova, E., Holcatova, I., Janout, V., Meric-Bernstam, F., Gascoyne, P., Wistuba, I., Varadhachary, G., Brennan, P., Hanash, S., Li, D., Maitra, A. & Alvarez, H. High prevalence of mutant KRAS in circulating exosome-derived DNA from early-stage pancreatic cancer patients. *Ann Oncol*. 2017; 28, 741-747.
- 179 Melo, S. A., Luecke, L. B., Kahlert, C., Fernandez, A. F., Gammon, S. T., Kaye, J., LeBleu, V. S., Mittendorf, E. A., Weitz, J., Rahbari, N., Reissfelder, C., Pilarsky, C., Fraga, M. F., Piwnicka-Worms, D. & Kalluri, R. Glypican-1 identifies cancer exosomes and detects early pancreatic cancer. *Nature*. 2015; 523, 177-182.
- 180 Lai, X., Wang, M., McElyea, S. D., Sherman, S., House, M. & Korc, M. A microRNA signature in circulating exosomes is superior to exosomal glypican-1 levels for diagnosing pancreatic cancer. *Cancer Lett*. 2017; 393, 86-93.
- 181 Yang, K. S., Im, H., Hong, S., Pergolini, I., Del Castillo, A. F., Wang, R., Clardy, S., Huang, C. H., Pille, C., Ferrone, S., Yang, R., Castro, C. M., Lee, H., Del Castillo, C. F. & Weissleder, R. Multiparametric plasma EV profiling facilitates diagnosis of pancreatic malignancy. *Sci Transl Med*. 2017; 9.

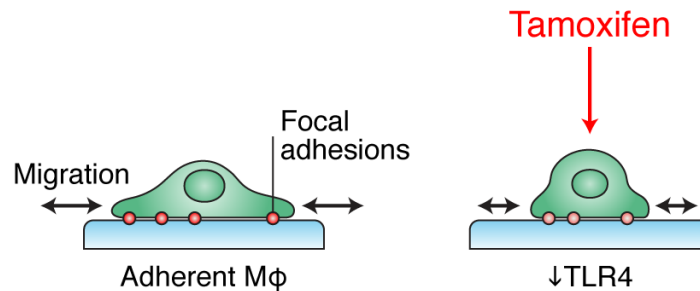


- 182 Ko, J., Carpenter, E. & Issadore, D. Detection and isolation of circulating exosomes and microvesicles for cancer monitoring and diagnostics using micro-/nano-based devices. *Analyst*. 2016; 141, 450-460.
- 183 Whiteside, T. L. The potential of tumor-derived exosomes for noninvasive cancer monitoring. *Expert Rev Mol Diagn*. 2015; 15, 1293-1310.
- 184 Yuana, Y., Boing, A. N., Grootemaat, A. E., van der Pol, E., Hau, C. M., Cizmar, P., Buhr, E., Sturk, A. & Nieuwland, R. Handling and storage of human body fluids for analysis of extracellular vesicles. *J Extracell Vesicles*. 2015; 4, 29260.
- 185 Yamada, T., Inoshima, Y., Matsuda, T. & Ishiguro, N. Comparison of methods for isolating exosomes from bovine milk. *J Vet Med Sci*. 2012; 74, 1523-1525.
- 186 Zlotogorski-Hurvitz, A., Dayan, D., Chaushu, G., Korvala, J., Salo, T., Sormunen, R. & Vered, M. Human saliva-derived exosomes: comparing methods of isolation. *J Histochem Cytochem*. 2015; 63, 181-189.
- 187 Van Deun, J., Mestdagh, P., Sormunen, R., Cocquyt, V., Vermaelen, K., Vandesompele, J., Bracke, M., De Wever, O. & Hendrix, A. The impact of disparate isolation methods for extracellular vesicles on downstream RNA profiling. *J Extracell Vesicles*. 2014; 3.
- 188 Saenz-Cuesta, M., Arbelaiz, A., Oregi, A., Irizar, H., Osorio-Querejeta, I., Munoz-Culla, M., Banales, J. M., Falcon-Perez, J. M., Olascoaga, J. & Otaegui, D. Methods for extracellular vesicles isolation in a hospital setting. *Front Immunol*. 2015; 6, 50.
- 189 Chen, C., Skog, J., Hsu, C. H., Lessard, R. T., Balaj, L., Wurdinger, T., Carter, B. S., Breakefield, X. O., Toner, M. & Irimia, D. Microfluidic isolation and transcriptome analysis of serum microvesicles. *Lab Chip*. 2010; 10, 505-511.
- 190 Davies, R. T., Kim, J., Jang, S. C., Choi, E. J., Gho, Y. S. & Park, J. Microfluidic filtration system to isolate extracellular vesicles from blood. *Lab Chip*. 2012; 12, 5202-5210.
- 191 Shao, H., Chung, J., Balaj, L., Charest, A., Bigner, D. D., Carter, B. S., Hochberg, F. H., Breakefield, X. O., Weissleder, R. & Lee, H. Protein typing of circulating microvesicles allows real-time monitoring of glioblastoma therapy. *Nat Med*. 2012; 18, 1835-1840.
- 192 Rho, J., Chung, J., Im, H., Liong, M., Shao, H., Castro, C. M., Weissleder, R. & Lee, H. Magnetic nanosensor for detection and profiling of erythrocyte-derived microvesicles. *ACS Nano*. 2013; 7, 11227-11233.
- 193 Wang, Z., Wu, H. J., Fine, D., Schmulen, J., Hu, Y., Godin, B., Zhang, J. X. & Liu, X. Ciliated micropillars for the microfluidic-based isolation of nanoscale lipid vesicles. *Lab Chip*. 2013; 13, 2879-2882.
- 194 Kanwar, S. S., Dunlay, C. J., Simeone, D. M. & Negrath, S. Microfluidic device (ExoChip) for on-chip isolation, quantification and characterization of circulating exosomes. *Lab Chip*. 2014; 14, 1891-1900.
- 195 He, M., Crow, J., Roth, M., Zeng, Y. & Godwin, A. K. Integrated immunoisolation and protein analysis of circulating exosomes using microfluidic technology. *Lab Chip*. 2014; 14, 3773-3780.
- 196 Im, H., Shao, H., Park, Y. I., Peterson, V. M., Castro, C. M., Weissleder, R. & Lee, H. Label-free detection and molecular profiling of exosomes with a nano-plasmonic sensor. *Nat Biotechnol*. 2014; 32, 490-495.
- 197 Zhu, L., Wang, K., Cui, J., Liu, H., Bu, X., Ma, H., Wang, W., Gong, H., Lausted, C., Hood, L., Yang, G. & Hu, Z. Label-free quantitative detection of tumor-derived exosomes through surface plasmon resonance imaging. *Anal Chem*. 2014; 86, 8857-8864.

- 198 Vaidyanathan, R., Naghibosadat, M., Rauf, S., Korbie, D., Carrascosa, L. G., Shiddiky, M. J. & Trau, M. Detecting exosomes specifically: a multiplexed device based on alternating current electrohydrodynamic induced nanoshearing. *Anal Chem.* 2014; 86, 11125-11132.
- 199 Santana, S. M., Antonyak, M. A., Cerione, R. A. & Kirby, B. J. Microfluidic isolation of cancer-cell-derived microvesicles from heterogeneous extracellular shed vesicle populations. *Biomed Microdevices.* 2014; 16, 869-877.
- 200 Lee, K., Shao, H., Weissleder, R. & Lee, H. Acoustic purification of extracellular microvesicles. *ACS Nano.* 2015; 9, 2321-2327.
- 201 Dudani, J. S., Gossett, D. R., Tse, H. T., Lamm, R. J., Kulkarni, R. P. & Carlo, D. D. Rapid inertial solution exchange for enrichment and flow cytometric detection of microvesicles. *Biomicrofluidics.* 2015; 9, 014112.
- 202 Akagi, T., Kato, K., Kobayashi, M., Kosaka, N., Ochiya, T. & Ichiki, T. On-chip immunoelectrophoresis of extracellular vesicles released from human breast cancer cells. *PLoS One.* 2015; 10, e0123603.
- 203 Taller, D., Richards, K., Slouka, Z., Senapati, S., Hill, R., Go, D. B. & Chang, H. C. On-chip surface acoustic wave lysis and ion-exchange nanomembrane detection of exosomal RNA for pancreatic cancer study and diagnosis. *Lab Chip.* 2015; 15, 1656-1666.
- 204 Shao, H., Chung, J., Lee, K., Balaj, L., Min, C., Carter, B. S., Hochberg, F. H., Breakefield, X. O., Lee, H. & Weissleder, R. Chip-based analysis of exosomal mRNA mediating drug resistance in glioblastoma. *Nat Commun.* 2015; 6, 6999.
- 205 Jeong, S., Park, J., Pathania, D., Castro, C. M., Weissleder, R. & Lee, H. Integrated Magneto-Electrochemical Sensor for Exosome Analysis. *ACS Nano.* 2016; 10, 1802-1809.
- 206 Zhang, P., He, M. & Zeng, Y. Ultrasensitive microfluidic analysis of circulating exosomes using a nanostructured graphene oxide/polydopamine coating. *Lab Chip.* 2016; 16, 3033-3042.
- 207 Wunsch, B. H., Smith, J. T., Gifford, S. M., Wang, C., Brink, M., Bruce, R. L., Austin, R. H., Stolovitzky, G. & Astier, Y. Nanoscale lateral displacement arrays for the separation of exosomes and colloids down to 20 nm. *Nat Nanotechnol.* 2016; 11, 936-940.
- 208 Zhao, Z., Yang, Y., Zeng, Y. & He, M. A microfluidic ExoSearch chip for multiplexed exosome detection towards blood-based ovarian cancer diagnosis. *Lab Chip.* 2016; 16, 489-496.
- 209 Cho, S., Jo, W., Heo, Y., Kang, J. Y., Kwak, R. & Park, J. Isolation of extracellular vesicle from blood plasma using electrophoretic migration through porous membrane. *Sensors and Actuators B: Chemical.* 2016; 233, 289-297.
- 210 Ko, J., Hemphill, M. A., Gabrieli, D., Wu, L., Yelleswarapu, V., Lawrence, G., Pennycooke, W., Singh, A., Meaney, D. F. & Issadore, D. Smartphone-enabled optofluidic exosome diagnostic for concussion recovery. *Sci Rep.* 2016; 6, 31215.
- 211 Ibsen, S. D., Wright, J., Lewis, J. M., Kim, S., Ko, S. Y., Ong, J., Manouchehri, S., Vyas, A., Akers, J., Chen, C. C., Carter, B. S., Esener, S. C. & Heller, M. J. Rapid Isolation and Detection of Exosomes and Associated Biomarkers from Plasma. *ACS Nano.* 2017; 11, 6641-6651.
- 212 Liu, F., Vermesh, O., Mani, V., Ge, T. J., Madsen, S. J., Sabour, A., Hsu, E. C., Gowrishankar, G., Kanada, M., Jokerst, J. V., Sierra, R. G., Chang, E., Lau, K., Sridhar, K., Bermudez, A., Pitteri, S. J., Stoyanova, T., Sinclair, R., Nair, V. S., Gambhir, S. S. & Demirci, U. The Exosome Total Isolation Chip. *ACS Nano.* 2017; 11, 10712-10723.
- 213 Shin, S., Han, D., Park, M. C., Mun, J. Y., Choi, J., Chun, H., Kim, S. & Hong, J. W. Separation of extracellular nanovesicles and apoptotic bodies from cancer cell culture broth using tunable microfluidic systems. *Sci Rep.* 2017; 7, 9907.

- 214 Kang, Y. T., Kim, Y. J., Bu, J., Cho, Y. H., Han, S. W. & Moon, B. I. High-purity capture and release of circulating exosomes using an exosome-specific dual-patterned immunofiltration (ExoDIF) device. *Nanoscale*. 2017; 9, 13495-13505.
- 215 Wu, M., Ouyang, Y., Wang, Z., Zhang, R., Huang, P. H., Chen, C., Li, H., Li, P., Quinn, D., Dao, M., Suresh, S., Sadovsky, Y. & Huang, T. J. Isolation of exosomes from whole blood by integrating acoustics and microfluidics. *Proc Natl Acad Sci U S A*. 2017; 114, 10584-10589.
- 216 Liu, C., Guo, J., Tian, F., Yang, N., Yan, F., Ding, Y., Wei, J., Hu, G., Nie, G. & Sun, J. Field-Free Isolation of Exosomes from Extracellular Vesicles by Microfluidic Viscoelastic Flows. *ACS Nano*. 2017; 11, 6968-6976.
- 217 Hu, J., Sheng, Y., Kwak, K. J., Shi, J., Yu, B. & Lee, L. J. A signal-amplifiable biochip quantifies extracellular vesicle-associated RNAs for early cancer detection. *Nat Commun*. 2017; 8, 1683.
- 218 Liang, L. G., Kong, M. Q., Zhou, S., Sheng, Y. F., Wang, P., Yu, T., Inci, F., Kuo, W. P., Li, L. J., Demirci, U. & Wang, S. An integrated double-filtration microfluidic device for isolation, enrichment and quantification of urinary extracellular vesicles for detection of bladder cancer. *Sci Rep*. 2017; 7, 46224.
- 219 Ishihara, R., Nakajima, T., Uchino, Y., Katagiri, A., Hosokawa, K., Maeda, M., Tomooka, Y. & Kikuchi, A. Rapid and Easy Extracellular Vesicle Detection on a Surface-Functionalized Power-Free Microchip toward Point-of-Care Diagnostics. *ACS Omega*. 2017; 2, 6703-6707.
- 220 Fang, S., Tian, H., Li, X., Jin, D., Li, X., Kong, J., Yang, C., Yang, X., Lu, Y., Luo, Y., Lin, B., Niu, W. & Liu, T. Clinical application of a microfluidic chip for immunocapture and quantification of circulating exosomes to assist breast cancer diagnosis and molecular classification. *PLoS One*. 2017; 12, e0175050.

## Chapter 2: Tamoxifen modulates biomechanical phenotype of macrophages and TLR4 in the tumor microenvironment<sup>†</sup>



The tumor microenvironment is a complex milieu of diverse cell types, interconnected cytokine networks, and dysregulated extracellular matrix (ECM). In pancreatic ductal adenocarcinoma (PDAC) and other solid carcinomas, the stroma is a strong contributor to the progression of the disease: it is both a product of and a regulator of stromal myofibroblasts, which influences the invasiveness of cancer cells. Drug targeting of the stroma or myofibroblasts to reduce the pronounced fibroinflammatory reaction has therefore emerged as a potential therapeutic strategy. This approach arose from the observation that the mechanical stiffness of the tissue induces a reciprocal change in cell biomechanics; as such, we have previously used the anti-estrogen drug tamoxifen to reduce fibrosis by targeting the biomechanical properties of myofibroblasts. It is unclear, however, whether other stromal cell types like macrophages are similarly affected by ECM mechanics. Here we explore the use of tamoxifen for regulating the biomechanics of macrophages in RAW264.7 and THP-1 cells. We demonstrate that tamoxifen induces morphological changes consistent with substrate stiffness regulation. This is associated with regulation of focal adhesion dynamics, cytoskeletal activity, and migratory behavior. We also find that tamoxifen downregulates toll-like receptor 4 (TLR4) *in vitro* and in a mouse model of pancreatic cancer.

<sup>†</sup> Adapted from Lieberthal, T. J. & Del Rio Hernandez, A. Tamoxifen modulates biomechanical phenotype of macrophages and TLR4 in the tumor microenvironment. 2017. In review.

## 2.1 Introduction

The contribution of the tumor stroma – its architecture, composition, and mechanics – is now recognized as a major facet of solid carcinomas in breast, pancreas, and liver. In pancreatic ductal adenocarcinoma (PDAC), the stromal microenvironment features a stiff fibroinflammatory reaction containing myofibroblasts, which are activated by and perpetuate the tissue tension. This tissue fibrosis, or desmoplastic reaction, is thought to impair drug delivery and promote neoplastic transformation, yet has also been shown to restrain tumor growth and metastasis<sup>1-3</sup>. Our group and others have devoted significant attention towards therapeutic approaches that ameliorate tissue fibrosis via myofibroblast deactivation<sup>1</sup>, by for example all-trans retinoic acid, which beneficially reprograms pancreatic stellate cells to normalize the extracellular matrix (ECM)<sup>4,5</sup>. We have previously investigated the use of tamoxifen, an anti-estrogen receptor chemotherapeutic typically deployed in breast cancer patients, in pancreatic cancer. Tamoxifen modulates myofibroblast phenotype in pancreatic cancer and breaks the feedback loop between the mechanically stiff ECM and cell activation (unpublished data). Tamoxifen acts through the G-protein coupled estrogen receptor (GPER, GPR30) in myofibroblasts, and GPER expression is reduced in PDAC (**Figure 1-6**). Yet, understanding of the tumor stroma is incomplete and perhaps hindered by the lack of a full understanding of the various stromal cell types, all of which contribute to the disordered ECM with complex networks of cytokines, chemokines, proteolytic proteins, and crosslinkers.

Macrophages constitute a major component of the stroma and are integral to the progression of the disease. They are enriched in peritumoral areas in comparison to normal pancreas tissue, and the presence of immunosuppressive polarized macrophages correlates with reduced survival<sup>6</sup>. By suppressing T cell response, macrophages contribute to immune evasion of PDAC<sup>7</sup>. Previous work has focused on preventing monocyte-derived macrophage accumulation; for example, a recent study found CCR2 inhibition to be an effective adjuvant<sup>8</sup>. Given macrophages phenotypic plasticity, reprogramming macrophages to acquire anti-tumor immunity has also been suggested<sup>9-11</sup>.

Our previous work indicated that the effects of tamoxifen were not limited to deactivation of pancreatic myofibroblasts. We therefore asked whether macrophages

might be analogously activated by the biomechanical properties of the tumor microenvironment, and whether tamoxifen can beneficially intervene. However, the interplay between the mechanics of the ECM and macrophage biology is largely unknown as a general mechanism and in the tumor microenvironment specifically. Several studies have addressed substrate stiffness modulation of macrophage phenotype<sup>12-17</sup>, but agreement between them is lacking. One study in breast cancer found that macrophages tend to accumulate at the stiff invasive front of the tumor<sup>18</sup>, which may indicate a role for macrophage mechanobiology in cancer fibrosis.

Here we document the direct action of tamoxifen on RAW264.7 murine macrophages and THP-1 monocyte-derived macrophages. We show that, like in myofibroblasts, tamoxifen induces changes in macrophage morphology and spreading. We use polyacrylamide gels of different stiffnesses to demonstrate that these morphological changes can be recapitulated by fibrotic-like environments. Tamoxifen regulation of morphology is concomitant with changes in focal adhesion dynamics and cytoskeletal activity, which also inhibits migration. Finally, we determined that these morphological changes are related to tamoxifen induced inhibition of TLR4 *in vivo* and *in vitro*.

## 2.2 Materials and Methods

### 2.2.1 Cells and reagents

RAW264.7 murine macrophages were maintained in Dulbecco's Modified Eagle's Medium (DMEM) with 4.5 g/L glucose, L-glutamine, 10% fetal bovine serum (FBS; Sigma Aldrich), and 1% penicillin/streptomycin. THP-1 human monocytes were maintained in RPMI-1640 with 10% heat inactivated FBS (Invitrogen) and 1% penicillin/streptomycin. Pancreatic cancer cell lines BxPC-3 and SUIT2 were maintained in RPMI-1640 (with sodium pyruvate) and DMEM, respectively. Pancreatic stellate cells (PSCs) were maintained in DMEM F12/HAM with 10% heat inactivated FBS and 1% penicillin/streptomycin. Cell lines and origin are shown in **Table 3**. Cells were routinely tested for mycoplasma contamination.

**Table 3.** Cell lines used in this study.

Cell Line	Cell Type	Origin
RAW264.7	Adherent macrophage	Mouse leukemia virus transformed
THP-1	Monocyte	Human monocytic leukemia
BxPC-3	Pancreatic epithelial (carcinoma)	Female human adenocarcinoma
SUIT-2	Pancreatic epithelial (carcinoma)	Male human liver metastasis
PSC (primary)	PSC	Healthy human primary

One day prior to tamoxifen treatment, cell culture media was replaced with phenol red free DMEM F12/HAM or phenol red free RPMI-1640 with 10% double charcoal stripped serum (DCSS). The serum (DCSS) used 24 hours prior to and during tamoxifen treatment is stripped of endogenous estrogens that can interfere with signaling; phenol red is also removed due to mild estrogen-like behavior. Unless otherwise indicated, cells were treated with 5  $\mu$ M tamoxifen in respective media with 5% DCSS under dim light conditions; control cells were cultured in media containing ethanol vehicle (<0.1%). Kdo2-lipid A (KLA; Santa Cruz Biotech, Santa Cruz, CA) was used at 100 ng/mL. Cell viability was determined after indicated culture times and tamoxifen concentration by resazurin (Sigma Aldrich, St. Louis, MO), which is converted to fluorescent resorforin in the presence of viable cells. After treatment, 0.015 mg/mL of resazurin in 10% DCSS was added to cell cultures and incubated for 4 hours, after which fluorescence intensity (560 nm excitation, 590 nm emission) of 100  $\mu$ L of the solution was read.

### 2.2.2 Animals

All animal experiments were performed under UK Home Office license and approved by the University of Glasgow Animal Welfare and Ethical Review Board. KPC mice (Pdx-1 CreERT, KRas<sup>G12D/+</sup>, p53<sup>R172H/+</sup>) were injected intraperitoneally with oil vehicle (n=3) or 5 mg of tamoxifen (n=3) daily for two weeks beginning after detection of the primary tumor. After treatment, mice were sacrificed and pancreatic tissues harvested and frozen in optimal cutting temperature (OCT) medium.

### 2.2.3 Collection of conditioned media

THP-1 were seeded in T75 flasks at a concentration of 0.5 million/mL and differentiated into adherent macrophages with 100 nM phorbol 12-myristate 13-

acetate (PMA) for 24 hours at 37°C and 5% CO<sub>2</sub>. Cells were carefully washed three times with phosphate buffered saline (PBS) to remove PMA and cultured for a further 24 hours in phenol red free 10% DCSS prior to tamoxifen treatment. Following 24 or 48 hour treatment, cells were carefully washed three times with PBS to remove tamoxifen before replacing with phenol red free RPMI-1640 with 5% DCSS and cultured for 24 hours to generate CM. After culture, CM was collected and centrifuged at 10,000 x g for 5 min at 4°C to remove detached cells. The supernatant was snap frozen in liquid nitrogen and stored in -80°C. CM collection protocol is depicted in **Figure 2-1**.

**Figure 2-1.**

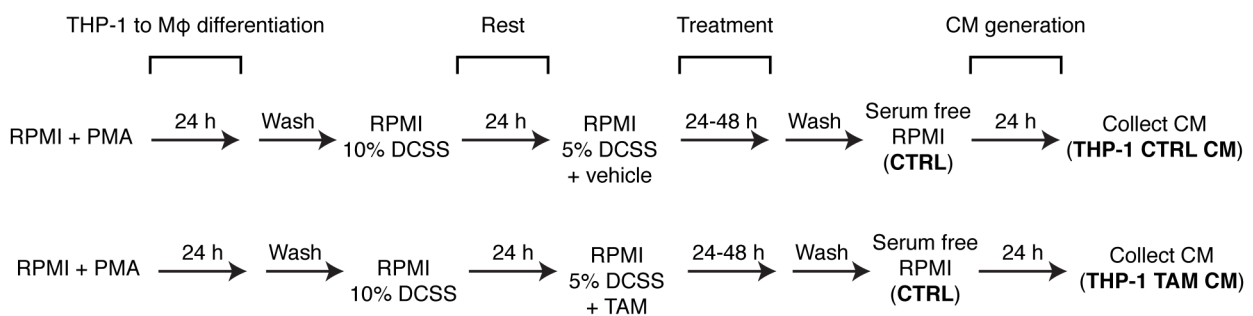


**Figure 2-1.** Preparation of CM from tamoxifen treated cells, media changes involved, and their purpose. The three types of media that were then used to culture SUIT-2, BxPC-3, and PSCs are shown in bold (CTRL, THP-1 CTRL CM, and THP-1 TAM CM).

SUIT-2 and BxPC-3 cancer cell lines were seeded into 48 well plates at a concentration of 10,000/mL; PSCs were seeded at 30,000/mL and allowed to attach for 16 hours. CM was diluted 1:1 in either serum-free DMEM or RPMI. Control media was prepared by diluting 5% DCSS in either RPMI or DMEM. Cells were washed once with PBS and cultured in diluted CM or control media for 48 hours. Resazurin was used to determine cell viability after the 48 hour culture period.

#### 2.2.4 2D migration

Glass coverslips were coated with 10 µg/mL fibronectin for 1 hour at 37°C and washed with PBS. Cells were seeded on coverslips at a density of approximately  $1 \times 10^4$  cm<sup>-2</sup> and allowed to attach overnight before tamoxifen or vehicle treatment. After 24 hours of treatment, migration was monitored over a period of 16 hours in at least three fields of view and three coverslips with brightfield microscopy (Nikon Ti-E) in a heated 5% CO<sub>2</sub> environmental chamber. Migration was monitored while cells were under tamoxifen treatment. Trajectories and migration velocity were determined using the ImageJ plug-in Manual Tracking. Migration trajectories were then plotted in MATLAB



by centering the initial coordinate at the origin and applying a color to each point to indicate the time point.

### 2.2.5 Polyacrylamide gel substrates

Polyacrylamide gels are often used to explore the cellular response to substrate rigidity as polyacrylamide can be easily mechanically tuned by varying pre-polymer components and can be functionalized with various ECM proteins. Cells were grown on polyacrylamide gels as previously described<sup>19</sup>. Briefly, 13 mm glass coverslips were functionalized with 4.0% (3-aminopropyl)triethoxysilane (APTES; Sigma Aldrich, St. Louis, MO) and 2.5% glutaraldehyde (Sigma Aldrich, St. Louis, MO). A polyacrylamide gel was formed on the coverslip by mixing acrylamide/bisacrylamide (29:1), tetramethylethylenediamine, and 10% ammonium persulfate in PBS. The acrylamide concentration of soft gels (1.3 kPa) and stiff gels (25.5 kPa) was 2.7% and 9.7%, respectively. The Young's modulus of these formulations was verified by shear rheology previously. Gels were subsequently functionalized with fibronectin (Sigma Aldrich, St. Louis, MO) at the indicated concentration via a sulfosuccinimidyl 6-(4'-azido-2'-nitrophenylamino)hexanoate crosslinker (Sulfo-SANPAH; Sigma Aldrich, St. Louis, MO). This protocol and key chemical reactions are depicted in **Figure 2-2**. Macrophages were seeded onto gels at a concentration of  $10^5$ /mL and incubated in 37°C, 5% CO<sub>2</sub> for 24 and 48 hours.

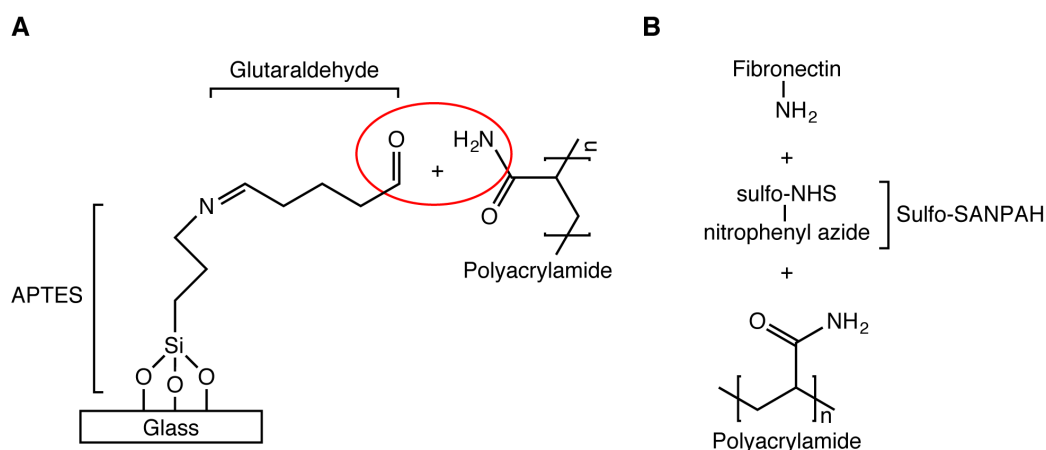


**Figure 2-2.** Formation of polyacrylamide gel substrates for cell culture. **(A)** Attachment of polyacrylamide gel to a glass coverslip via APTES and glutaraldehyde. Red circle indicates reaction. **(B)** Conjugation of biomolecules (i.e. fibronectin) with a sulfo-SANPAH UV-activatable crosslinker.

### 2.2.6 Immunofluorescence

Cells seeded on coverslips were fixed with 37°C 4% paraformaldehyde for 10 minutes, washed twice with PBS for 5 minutes, and blocked/permeabilized with 2% bovine

serum albumin (BSA)/0.1% Triton X100 (Sigma Aldrich, St. Louis, MO). Cells were incubated with anti-talin (ab7133 1/100; Abcam, Cambridge, UK) for 1 hour at room temperature in 2% BSA (Sigma Aldrich, St. Louis, MO), followed by goat anti-rabbit Alexa Fluor 488 secondary antibody incubation for 45 min (1/400; ThermoFisher) or stained for F-actin with Alexa Fluor 546 phalloidin (1/500, ThermoFisher). Coverslips were mounted with Prolong Gold Antifade Reagent containing 4',6-diamidino-2-phenylindole (DAPI) (Thermo Fisher Scientific) and imaged with an inverted epifluorescent microscope (Nikon Eclipse Ti). Total internal reflectance fluorescence (TIRF) microscopy was used to visualize the focal adhesion structure of adherent cells. TIRF is an imaging technique by which a light source illuminates the sample above the internal reflectance critical angle of the incident light. Although the light is not transmitted through the sample, an evanescent wave extends ~100 nm into the sample and therefore illuminates only the fluorophores within this region (i.e. the focal adhesion proteins). Fixed cells were mounted in PBS and imaged with a 60x objective with 1.5 zoom. Quantification was conducted using ImageJ (NIH, Bethesda, MD). For morphological analysis, F-actin stained cells were thresholded and quantified using the built-in ImageJ circularity plug-in where a perfect circle is given a value of 1. For analysis of talin-containing focal adhesions, automatic thresholds were applied and the Analyze Particles function was used to determine focal adhesion geometric parameters.

For immunofluorescence of tissues, OCT-embedded 6  $\mu\text{m}$  sections were fixed in 4% paraformaldehyde for 15 minutes and washed with PBS. Sections were blocked with 10% goat serum (Sigma Aldrich, St. Louis, MO) for 1 hour followed by 20  $\mu\text{g}/\text{mL}$  AffiniPure Fab goat anti-mouse IgG fragment (Jackson ImmunoResearch Laboratories, Suffolk, UK) for 30 min. Sections were washed in PBS and incubated with anti-TLR4 (ab22048 1/300; Abcam, Cambridge, UK) and anti-F4/80 (ab6640 1/100; Abcam, Cambridge, UK) in 1% BSA for 16 hours at 4°C. Primary antibodies were washed with PBS and incubated with goat anti-mouse Alexa Fluor 546 (1/200) and goat anti-rat Alexa Fluor 488 (1/200) for 1 hour at room temperature. Secondaries were washed with 0.1% Triton X-100 (Sigma Aldrich, St. Louis, MO). Nuclei were stained with Hoechst 33342 (1/10,000; Life Technologies). Slides were mounted with Prolong Gold (Life Technologies).

### 2.2.7 Scanning electron microscopy

Cells were fixed on coverslips with 3% EM grade glutaraldehyde (Sigma Aldrich, St. Louis, MO) in 0.1 M PBS for 15 minutes at 37°C. Coverslips were washed with PBS and stained with 1% osmium tetroxide (Sigma Aldrich, St. Louis, MO) in PBS for 1 hour at room temperature before washing and dehydrating in an ethanol series (30-100%). Coverslips were air dried overnight and coated with 10 nm chromium. Imaging was conducted with a Zeiss Sigma 300 microscope operating at an electron acceleration voltage of 2 kV.

### 2.2.8 Fluorescence recovery after photobleaching (FRAP) microscopy

In FRAP microscopy, live cells transfected with a fluorescently tagged protein are selectively photobleached with a high powered confocal. Subsequent time-lapse imaging of the bleached region results in recovery of fluorescence due to diffusion/recruitment of the protein from unbleached regions to the bleached region. The rate of recovery therefore indicates the rate of protein recruitment in the examined cell. RAW264.7 macrophages were transfected with mEGFP-Lifeact-7 (gift from Michael Davidson, Addgene plasmid # 54610) using JetPrime reagent (Polypus, Bioparc, France) according to manufacturer's instructions. After transfection, cells were cultured for 24 hours in phenol red-free media prior to tamoxifen treatment for a further 24 hours. TIRF microscopy as previously described was used to collect fluorescence intensity at the glass substrate interface. After high-powered confocal photobleaching, TIRF was used to collect fluorescence recovery over a period of 3 minutes. ImageJ was used to quantify recovery of the entire bleached region. Data is normalized to fluorescence prior to bleaching; events where bleaching efficiency was less than 50% were excluded from analysis. Significant differences between conditions were determined by multi-point t-tests at each time point after bleaching. Half recovery time ( $t_{1/2}$ ) was calculated by fitting curves to a one-phase association exponential function  $y = \text{span}(1 - e^{-kx}) + \text{bottom}$ , where  $t_{1/2} = \ln(2) / k$ .

### 2.2.9 Western Blot

Cells were washed in 6-well plates with ice-cold PBS and lysed with radioimmunoprecipitation assay (RIPA) buffer (Sigma Aldrich, St. Louis, MO) with protease inhibitors on ice. Lysate supernatant protein concentration was determined by the DC Protein Assay (Biorad). Proteins were separated in a 10% polyacrylamide

gel under reducing conditions and transferred to a nitrocellulose membrane (GE Healthcare). The membrane was blocked with 5 wt% skim milk in Tris-buffered saline with 0.1% Tween-20 (TBST; Sigma Aldrich, St. Louis, MO) for 30 minutes and incubated with the primary antibodies anti-TLR4 (1/250 ab22046; Abcam, Cambridge, UK) and anti-GAPDH (1/5000 sc-32233; Santa Cruz Biotechnology, Santa Cruz, CA) in blocking buffer overnight at 4°C. The membrane was washed in TBST and incubated with HRP secondary antibodies for 2 hours at room temperature prior to washing and developing with horseradish peroxidase (HRP) substrate (Millipore). TLR4 and GAPDH bands are cropped from the same gel with different exposures. Exposure time for each band was selected automatically using the blot development software.

#### 2.2.10 Quantitative RT-PCR

RNA was extracted from cells with QIAshredder and RNeasy Mini kits (Qiagen, Crawley, UK); cDNA was transcribed with a high capacity RNA-to-cDNA kit (Applied Biosystems, Foster City, CA). RT-PCR was performed using KiCqStart® primers (Sigma Aldrich), SYBR green master mix (Life Technologies, USA), and 100 ng of cDNA input on a StepOnePlus™ system (Applied Biosystems, Foster City, CA). Fold differences in expression were computed using the housekeeping gene TATA-binding protein (TBP) and the  $2^{-\Delta\Delta Ct}$  method. Primer sequences are as follows:

TBP forward GTTCTTAGACTTCAAGATCCAG

TBP reverse TTCTGGGTTTGATCATTCTG

TLR4 forward GATCAGAAACTCAGCAAAGTC

TLR reverse TGTTTCAATTCACACCTGG

TNF- $\alpha$  forward CTATGTCTCAGCCTCTTCTC

TNF- $\alpha$  reverse CATTGGGAACTTCTCATCC

IL-1 $\beta$  forward GGATGATGATGATAACCTGC

IL-1 $\beta$  reverse CATGGAGAATATCACTTGTTGG.

#### 2.2.11 Statistics

Differences between control and tamoxifen groups were compared by two-tailed Student's t-test (GraphPad Prism, San Diego, CA). For analysis of cell area, circularity, and velocity, a Mann-Whitney nonparametric t-test was used. For multigroup

comparisons of cell area and circularity, a Kruskal-Wallis ANOVA with Dunn's multiple comparisons post-test was used. A p-value of less than 0.05 was regarded as significant. Significance is denoted as \* $p < 0.05$ , \*\* $p < 0.01$ , \*\*\* $p < 0.001$ , \*\*\*\* $p < 0.0001$ . Error bars are standard errors of mean (SEM).

## 2.3 Results

### 2.3.1 Tamoxifen reduces cell spread area and increases circularity

In previously investigating tamoxifen action on stromal cells, we used tamoxifen at a concentration of 5  $\mu\text{M}$ . At this concentration RAW264.7 macrophages maintain >95% viability in comparison to vehicle (ethanol) treated cells at 24 hours (**Figure 2-3A**) and non-significantly reduces proliferation at 48 hours (**Figure 2-3B**). Unless otherwise indicated, tamoxifen is used here at 5  $\mu\text{M}$  over 24 hours.

To determine if tamoxifen can regulate cell biomechanics, we first analyzed morphological changes of cells cultured on fibronectin functionalized glass. When seeded at a low density, RAW264.7 macrophages can adopt a mesenchymal-like phenotype with a large cell spread area and low circularity (i.e. polarized shape or many filopodial extensions). After tamoxifen treatment, cells reduced adhesion area and increased in circularity as determined by F-actin immunofluorescence (**Figure 2-3C** and **Figure 2-3D**). To investigate more detailed changes in structure, we used scanning electron microscopy (SEM) on tamoxifen treated cells. SEM imaging also shows tamoxifen-induced reduction in cell spread area with a concomitant increase in cell height (**Figure 2-3E**). Additionally, among control and tamoxifen-treated cells of similar cell shape, control cells exhibit more extensive branching of filopodial networks at the cell edge whereas tamoxifen-treated cells contain fewer of these extensions (**Figure 2-3E**, boxes). These differences in morphology are more evident by 48 hours (**Figure 2-3F**). Furthermore, by 48 hours, many cells become partially detached by tamoxifen (**Figure 2-3F** inset), perhaps indicating a defect in adhesion to fibronectin.

### 2.3.2 Morphological changes are recapitulated in fibrotic-like in vitro environments

We hypothesized that tamoxifen could interfere with cell mechanosensing and the response to fibrotic environments, which feature increased mechanical stiffness (Young's modulus) and ECM deposition. To confirm that macrophage spreading and circularity are normally regulated by substrate mechanics, we seeded cells on

polyacrylamide gels of low (1.2 kPa) and high (25 kPa) stiffness and functionalized with low (10  $\mu\text{g/mL}$ ) and high (50  $\mu\text{g/mL}$ ) fibronectin to achieve different ligand densities. Consistent with previous reports<sup>12,13</sup>, softer substrates produce more cell rounding and less cell spread area (**Figure 2-4A**).

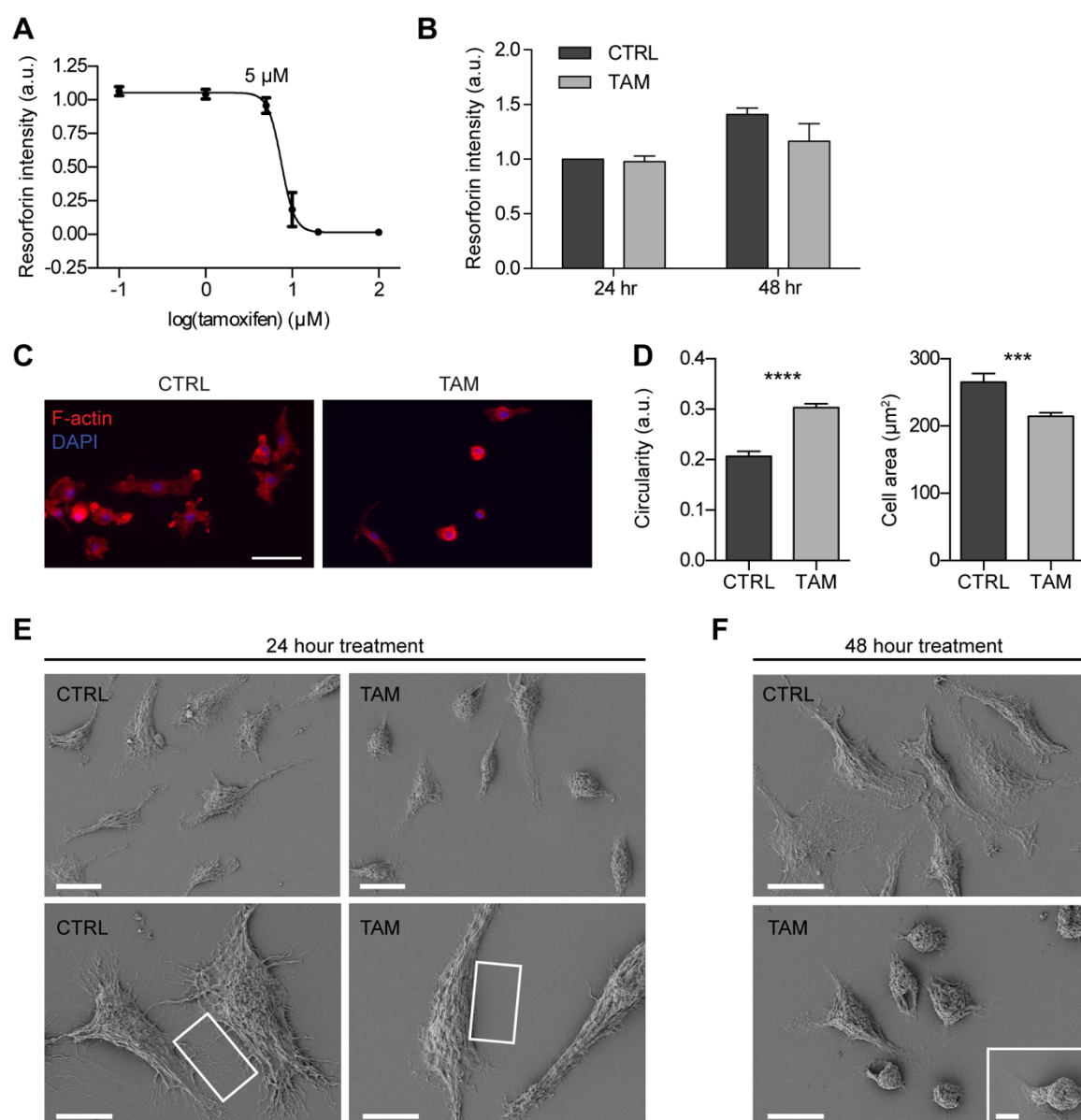


**Figure 2-3.** Tamoxifen (TAM) induces morphological changes in RAW264.7 macrophages. **(A)** Tamoxifen is used at (5  $\mu\text{M}$ ) without accumulating significant cytotoxicity at 24 hours ( $n=6$ ) and at **(B)** 48 hours ( $n=3$ ). **(C)** F-actin staining of treated macrophages on fibronectin coated glass reveals that tamoxifen reduces **(D)** cell circularity and **(E)** cell spread area at 24 hours ( $n>100$  cells per condition; scale bar is 50  $\mu\text{m}$ ). **(E)** Scanning electron microscopy confirms morphological changes. Tamoxifen tends to produce more round and less flat cells (upper figures). In comparing CTRL and TAM cells with similar mesenchymal spreading (lower figures, boxes), TAM reduces dynamic filipodial extensions. Scale bars are 20  $\mu\text{m}$ . **(F)** Shape changes are more pronounced at 48 hour treatment. Scale bars are 20  $\mu\text{m}$ . Additionally, some cells become partially detached or semi-adherent by tamoxifen (lower figure, inset). Inset scale bar is 5  $\mu\text{m}$ . Data represents mean  $\pm$  SEM. \*\*\* $p < 0.001$ , \*\*\*\* $p < 0.0001$ .

We also report a similar response to decreased fibronectin functionalization of the soft substrate; specifically, cell spread area decreases and cell circularity increases for 1 kPa substrates with low fibronectin density in comparison to high fibronectin density (Figure 2-4B). These trends are also observed over a 48 hour culture time (Figure 2-5). The effect of fibronectin is not observed for stiff (25 kPa) substrates likely due to the overriding influence of substrate stiffness.

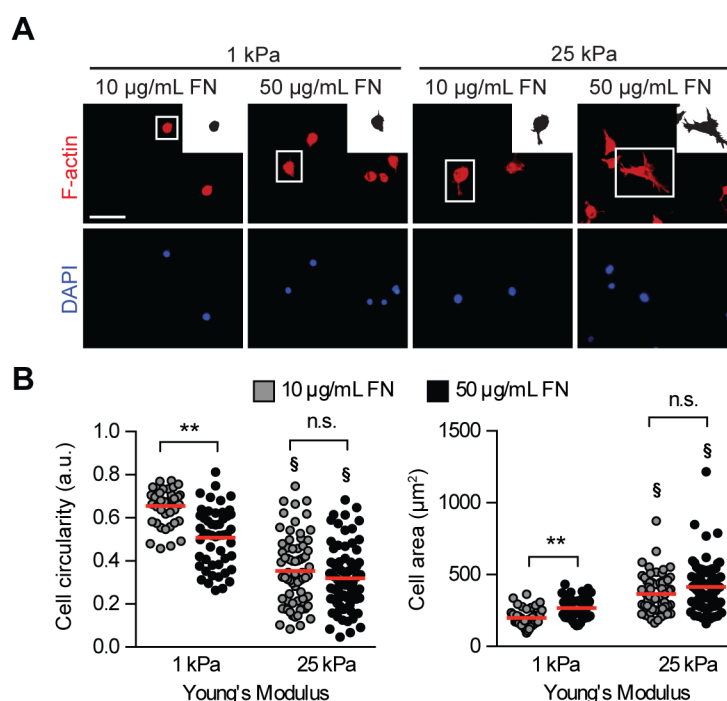


**Figure 2-4.** Macrophages respond to substrates mimicking fibrotic environments. (A) Macrophages were seeded on soft (1.2 kPa) or stiff (25.5 kPa) polyacrylamide substrates conjugated with low (10 µg/mL) or high (50 µg/mL) soluble fibronectin (FN) for 24 hours. F-actin immunofluorescence staining shows a gradual increase in cell spread area and polarity with increasing FN and stiffness. Inset shows binary masks used to quantify circularity and area. Scale bar is 50 µm. (B) Quantification of immunofluorescence images in A. Each point represents a cell ( $n \geq 44$  cells per condition) with the horizontal bar representing the mean. \*\*  $p < 0.01$ , §  $p < 0.0001$  in comparison to softer substrate at same FN concentration.

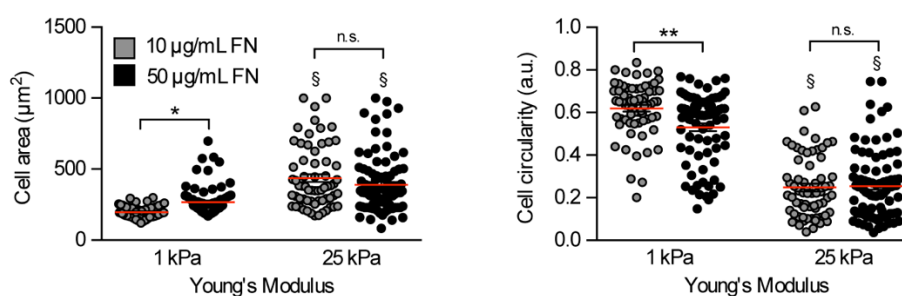


**Figure 2-5.** Macrophage cell spread area and circularity on soft (1.2 kPa) or stiff (25 kPa) polyacrylamide gels conjugated with low (10 µg/mL) or high (50 µg/mL) fibronectin (FN) 48 hours after seeding.

Consistent with previous results<sup>13</sup>, we also observe a reduction in actin intensity for cells grown on soft low fibronectin substrates (**Figure 2-6**). Thus, macrophages are responsive to the two hallmark features of fibrosis, high stiffness and ECM concentration (**Figure 2-4**), and tamoxifen modulates this response in an extremely high substrate stiffness environment (tissue culture polystyrene; **Figure 2-3**).

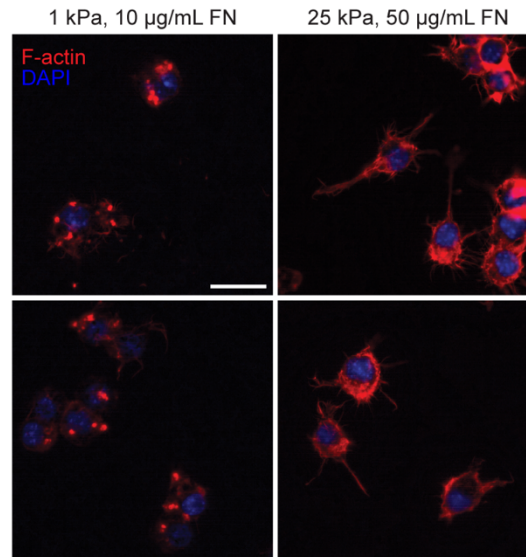


**Figure 2-6.** Confocal microscopy of F-actin stained macrophages grown on substrates mimicking little fibrosis (low stiffness, low FN) or high fibrosis (high stiffness, high FN).

### 2.3.3 Tamoxifen regulates talin-containing podosomes, cytoskeleton, and migration

Changes in cell spread area and circularity may be a result of altered focal adhesion organization. Macrophages contain specialized focal adhesion-like structures called podosomes, which consist of an actin core that co-localizes with typical focal adhesion proteins like paxillin, vinculin, and talin-1 (ref 20). Importantly, macrophage podosomes have been shown mechanosensitive elements that respond to substrate stiffness<sup>21,22</sup>, which is consistent with substrate modulation of macrophage morphology<sup>13</sup> and traction stresses<sup>23</sup>. Talin in particular is a well-described mechanosensitive protein<sup>24</sup>, the dysregulation of which can play a role in various disease states<sup>25</sup>. Thus, we used TIRF microscopy on immunostained coverslips to characterize talin-containing focal adhesions. Tamoxifen reduced the number of focal adhesions per cell, which is attributable to a reduction in cell spread area (**Figure 2-7A** and **Figure 2-7B**). There was also no significant difference in size of individual focal adhesions. However, the fluorescent intensity of talin in focal adhesions was reduced



upon tamoxifen treatment, perhaps indicating a defect in focal adhesion protein recruitment, but not assembly.

The structural integrity of macrophage podosomes is dependent on a tensional homeostasis between the adhesion proteins and actin core. Inhibition of talin, for example, inhibits actin polymerization at podosomes and reduces protrusion force<sup>21</sup>. To investigate protein recruitment to the podosomes, we used FRAP microscopy to monitor live cell cytoskeletal dynamics by transfecting macrophages with fluorescent actin (mEGFP-Lifeact-7). After photobleaching, the F-actin recovery plateau was impaired in tamoxifen treated cells compared to control cells ( $p < 0.05$ , **Figure 2-7C**), whereas the rate of mobile actin recruited to bleached regions did not significantly differ ( $t_{1/2}$  half recovery time). The inhibited recovery of actin in tamoxifen treated cells indicates a more stable immobile fraction of actin (0.35 in control vs. 0.44 in TAM) and thus a more stable F-actin network. Although  $t_{1/2}$  was similar between the two conditions, bleaching locations were not recorded within the lamellipodium (the lack of polarization in tamoxifen-treated cells prevents the appearance of a leading edge), and the retention of actin within the cell body may be coupled to a reduction in polymerization at the leading edge through sequestration and inhibited disassembly<sup>26,27</sup>. Additionally, actin flow and turnover is governed by cell traction forces and myosin II<sup>28</sup>, which have previously been shown to be inhibited by tamoxifen in PSCs.

Regulation of cell morphology, podosomes, and actin polymerization dynamics have direct implications on cell migratory behavior. In mesenchymal migrating cells, active actin polymerization at the polarized leading edge of the lamella acts in concert with newly formed focal adhesions and disassembled focal adhesions at the rear. Using polyacrylamide gels, Patel *et al.* (2012) found that substrate stiffness can differentially regulate gene expression in RAW264.7 macrophages<sup>13</sup>. Using the transcriptome profiling of macrophages cultured on soft (1.2 kPa) and stiff (150 kPa) substrates (data set GSE36878), several ontological terms relating to cell migration are enriched in regulated genes (**Figure 2-8**). However, regulation of macrophage velocity on different substrate stiffnesses has only been observed for short time points<sup>12</sup> and dependent on exogenous stimulus<sup>14</sup>.

To determine the net effect of tamoxifen-induced changes in morphology, focal adhesion parameters, and actin stability, we plated cells on fibronectin-coated glass and determined random migration trajectories and velocities over 16 hours.

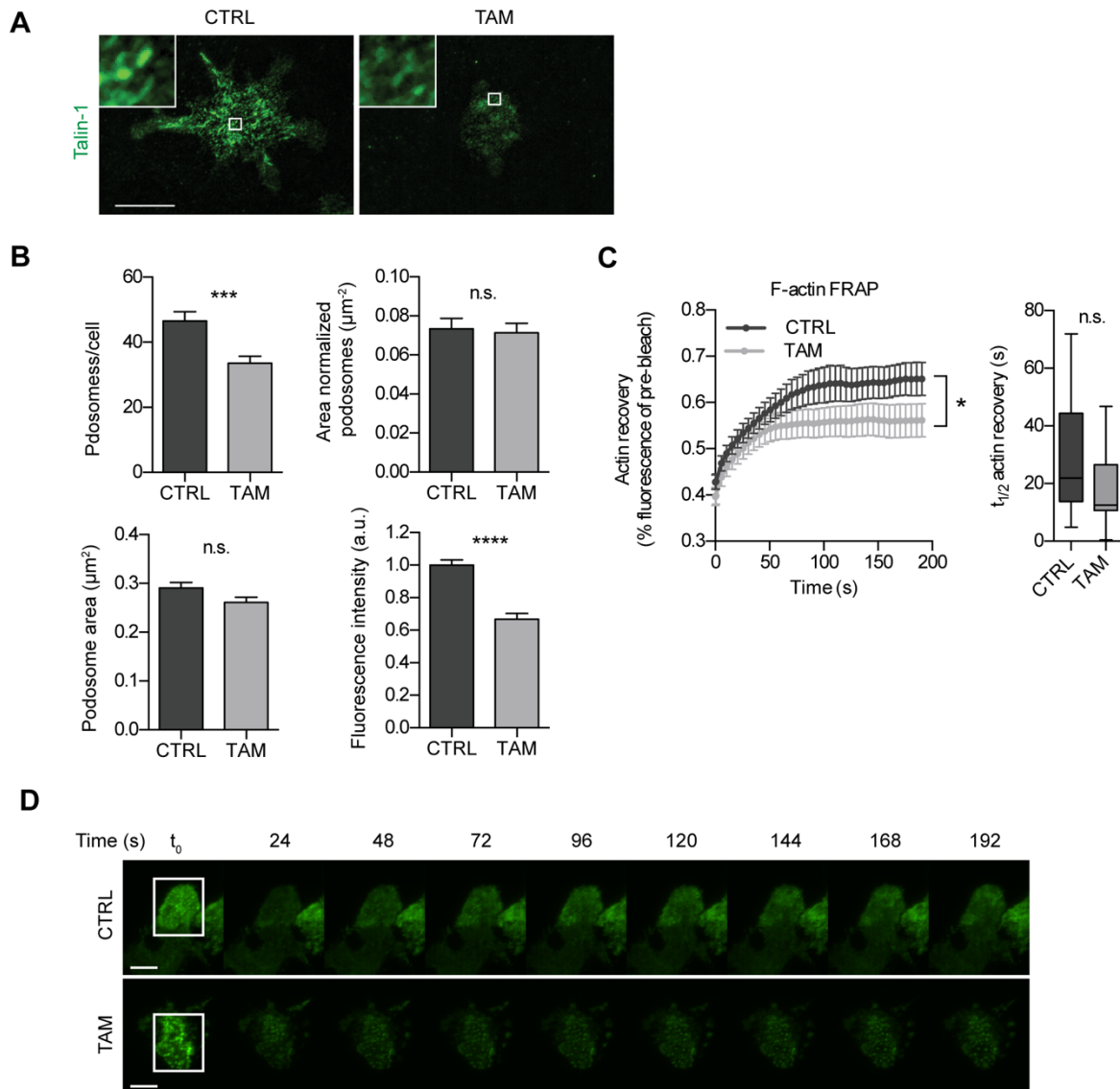


**Figure 2-7.** Tamoxifen regulates focal adhesion dynamics and cell migration. **(A)** Macrophages seeded on fibronectin-coated glass were immunostained for talin-1 and imaged by TIRF microscopy after 24 hours treatment. Scale bar is 50  $\mu\text{m}$ . **(B)** Focal adhesion parameters were quantified by automatic thresholding the ImageJ Analyze Particles plug-in. Tamoxifen reduced the number of podosomes per cell, which can be attributable to the reduction in cell spread area (see area normalized number of podosomes). While the size of focal adhesions did not significantly differ, the fluorescence intensity was reduced in tamoxifen-treated cells. **(C)** Podosome structure regulation is associated with reduced actin plateau but unchanged half recovery time ( $t_{1/2}$ ) as measured by FRAP microscopy ( $n = 15-17$  cells). **(D)** Representative FRAP images in which TAM-treated cells demonstrate impaired fluorescence recovery. Boxes represent the bleached region. Scale bar is 10  $\mu\text{m}$ . Data represents mean  $\pm$  SEM. \* $p < 0.05$  \*\*\* $p < 0.001$ , \*\*\*\* $p < 0.0001$ .

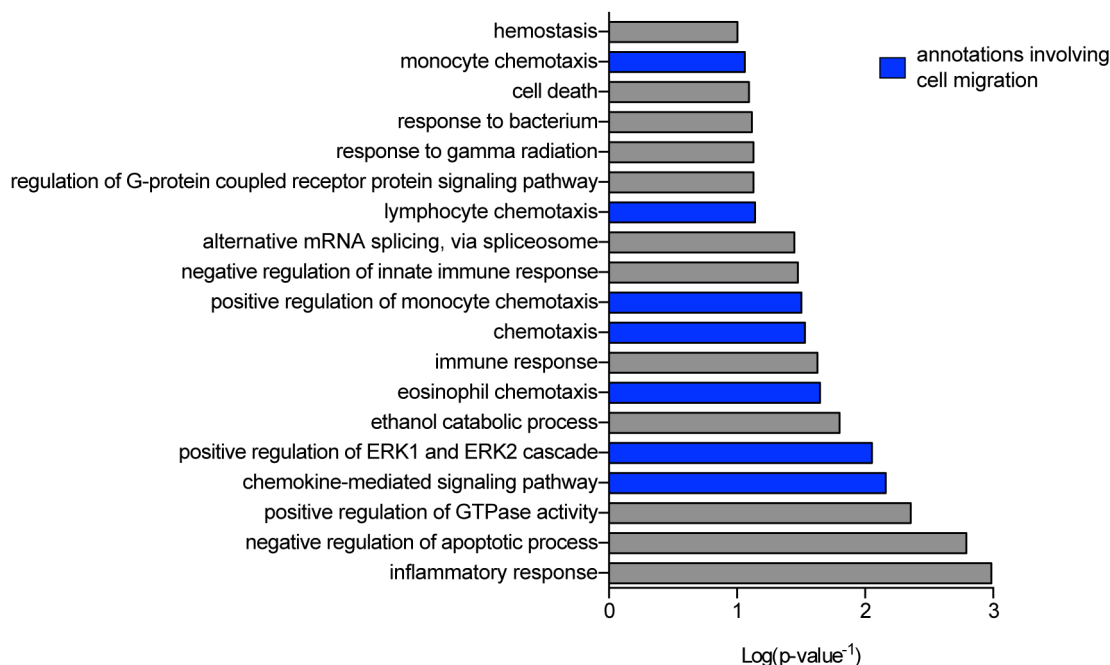


**Figure 2-8.** Gene ontology enrichment of RAW264.7 macrophages cultured on soft (1.2 kPa) and stiff (150 kPa) substrates (data set GSE36878 (ref 13)). Blue annotations indicate involvement in cell migration. Enrichment was determined using the NIH DAVID Bioinformatics 6.8 functional annotation tool.

Tamoxifen reduced cell migration speed and distance (**Figure 2-9**). Additionally, about 15% of tamoxifen treated cells exhibited a transient detachment from the substrate, perhaps an indication of a defect in adhesion (see also **Figure 2-3F** inset). Thus, we observe that tamoxifen regulation of focal adhesions is associated with inhibited actin polymerization, both of which can contribute to inhibited migratory ability.

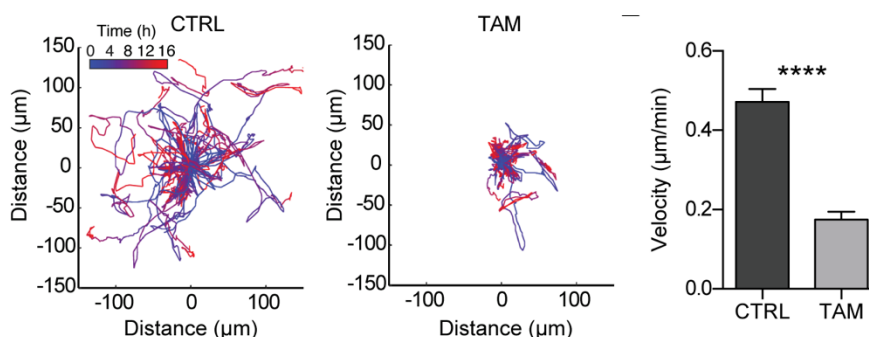


**Figure 2-9.** 2D migration distance and speed of macrophages is inhibited by tamoxifen. Macrophages were seeded on fibronectin-coated glass prior to treatment for 24 hours. Migration was imaged over 16 hours and velocities were computed using manual tracking in ImageJ. Migration trajectories represent 30 cell tracks. Data represents mean  $\pm$  SEM. \*\*\*\* $p < 0.0001$ .

In support of this observed transient detachment, the density of macrophages adherent on fibronectin-coated glass was determined after F-actin/DAPI staining (**Figure 2-10**; also see microscopy images in **Figure 2-3C**). Tamoxifen reduces the adherent density of macrophages; yet, curiously, cell viability/number as measured by resazurin does not significantly differ at this dose and these selected time points (see viability in **Figure 2-3D**). The observed discrepancy is likely due to removal of loosely attached tamoxifen-treated cells during the immunofluorescence staining process, which involves several washing steps that normally do not dislodge properly adhered cells. This further indicates that tamoxifen-treated cells do not have as robust focal adhesions as control cells and can become dislodged.

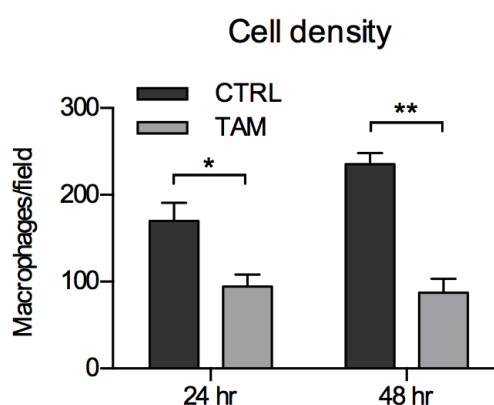


**Figure 2-10.** Tamoxifen reduces macrophage adherent density on fibronectin-coated glass, likely due to shear-induced detachment during staining. Compare to Figure 2-3B where 24-48 hr TAM treated cells do not significantly differ in viability. Number of macrophages were counted in a Data represents mean  $\pm$  SEM (n=3). \*p < 0.05 \*\*p < 0.01.

#### 2.3.4 Tamoxifen regulates TLR4 and downstream cytokines

It has previously been shown that biomechanical regulation of macrophages via substrate stiffness involves increased expression and signaling of TLR4, a pattern recognition receptor activated by lipopolysaccharide (LPS) that regulates a robust inflammatory response under control of the transcription factor NF $\kappa$ B<sup>15</sup>. Stimulation of RAW264.7 with LPS also promotes cell spreading<sup>29</sup>, and treatment of macrophages with LPS/IFN- $\gamma$  increases membrane stiffness<sup>13,30</sup>. In studies involving various cell types and inflammatory conditions, tamoxifen has been shown to influence LPS responsiveness, elements of TLR4 pathways, or cytokines regulated by TLR4<sup>31-33</sup>. Thus, we hypothesized that the macrophage biomechanical phenotype under control of tamoxifen was related to TLR4 regulation.

Indeed, tamoxifen reduced expression of TLR4 and downstream pro-inflammatory cytokines TNF- $\alpha$  and IL-1 $\beta$  (**Figure 2-11A**). TLR4 regulation was also observed over 24 and 48 hours by immunoblotting (**Figure 2-11B**). To confirm tamoxifen downregulation of TLR4, we used a mouse model of pancreatic cancer (KPC; KRas<sup>G12D/+</sup>, p53<sup>R172H/+</sup>; Pdx-1 CreERT), which recreates the hallmark histopathological features of the tumor stroma<sup>34</sup>. Mice were injected intraperitoneally with vehicle (oil) or 5 mg of tamoxifen daily for two weeks, after which tissues were harvested and frozen. We have previously observed that macrophage infiltration to the tumor stroma was reduced in tamoxifen treated mice and tamoxifen ameliorates the desmoplastic stroma (unpublished data). Immunofluorescent staining of pancreas tissues for F4/80<sup>+</sup> tumor associated macrophages and TLR4 revealed a reduction in TLR4 staining intensity for tamoxifen treated mice (**Figure 2-11C**).

To determine if tamoxifen can desensitize macrophages to TLR4 stimulation, we seeded cells on fibronectin-coated coverslips and pretreated them with tamoxifen for 24 hours prior to stimulation with Kdo2-lipid A (KLA) for 4 hours. KLA is a more chemically well-defined and potent natural product derivative of LPS, a TLR4 agonist<sup>35,36</sup>. Stimulation of control cells by KLA reduced circularity (not significant,  $p > 0.05$ ), but the most prominent effect was seen in an increase in cell spread area (**Figure 2-11D**) as expected from the role of TLR4 in regulating the actin cytoskeleton and integrin-mediated adhesion<sup>37</sup>. The increase in cell spread area with KLA is consistent with increased macrophage spreading on stiff substrates (**Figure 2-4**), which involves TLR4 expression<sup>15</sup>. Tamoxifen significantly abrogated KLA-induced morphology changes: tamoxifen reduced the cell spread area of KLA-treated cells by about 70%, indicating a loss of TLR4 agonist sensitivity. We also note that tamoxifen significantly reversed nuclear enlargement as a result of TLR4 stimulation. Thus, tamoxifen downregulates TLR4 and blocks TLR4 agonist-induced morphology changes.

#### 2.3.5 TLR4 downregulation does not affect paracrine cytotoxicity

Reprogramming macrophages to adopt a classical inflammatory phenotype (e.g. secretion of TNF- $\alpha$  and IL-1) has been suggested to promote tumor cytotoxicity<sup>38</sup>. Given that LPS is commonly used in combination with IFN- $\gamma$  to induce the inflammatory phenotype, and LPS acts primarily through TLR4, we sought to

determine if tamoxifen downregulation of TLR4 would instead be tumor cell growth permissive.

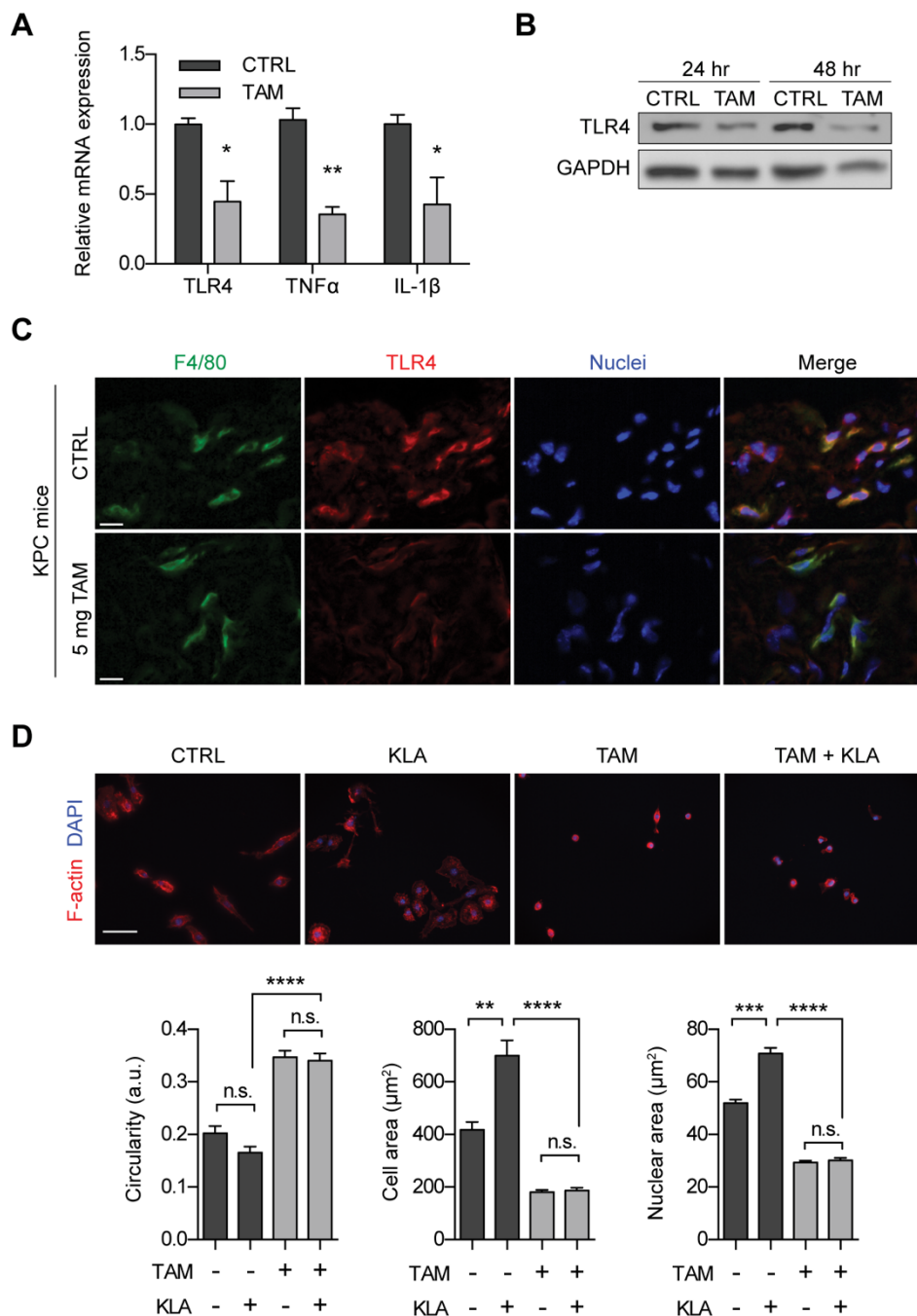


**Figure 2-11.** Tamoxifen downregulates TLR4. **(A)** TLR4 and cytokines induced by TLR4 activation, TNF- $\alpha$  and IL-1 $\beta$ , are downregulated after 24 hours of tamoxifen treatment. Data represent mean  $\pm$  SEM (n=3). **(B)** Representative immunoblots of TLR4 in macrophages treated for 24 or 48 hours of tamoxifen. Bands are cropped from the same gel and developed using automatic exposure. **(C)** Representative immunohistochemistry staining of KPC mice treated with 5 mg tamoxifen or vehicle (oil) for F4/80 macrophages and TLR4. Expression of TLR4 by staining intensity is reduced with tamoxifen treatment. Scale bar is 50  $\mu\text{m}$ . **(D)** Macrophages were pretreated for 24 hours with tamoxifen prior to stimulation with the TLR4 agonist KLA (100 ng/mL) for 4 hours. Tamoxifen abrogated KLA-induced cell spreading and nuclear enlargement. Scale bar is 50  $\mu\text{m}$ . \*  $p < 0.05$  \*\*  $p < 0.01$  \*\*\*  $p < 0.001$  \*\*\*\*  $p < 0.0001$ .

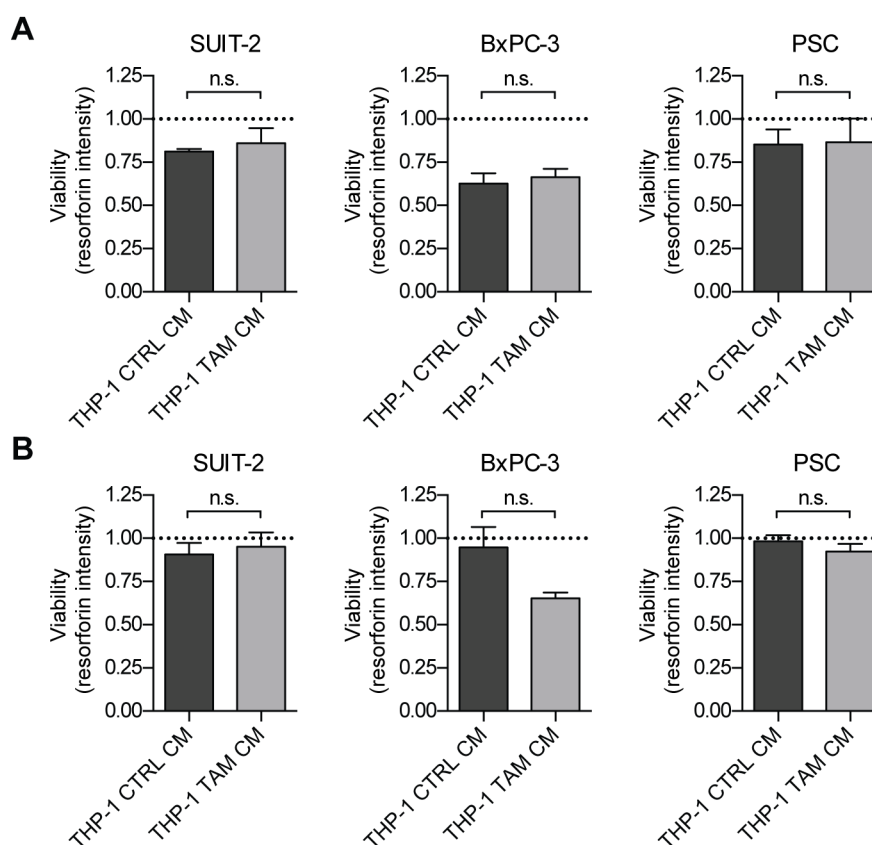


**Figure 2-12.** Tamoxifen treatment and TLR4 inhibition is not associated with increased SUIT-2, BxPC-3, or PSC I cell proliferation. THP-1 monocyte derived macrophages were cultured for **(A)** 24 or **(B)** 48 hours with 5  $\mu$ M tamoxifen (THP-1 TAM CM) or vehicle control (THP-1 CTRL CM). Conditioned media was generated over a 24 hour period following treatment. Data is normalized to cell viability in normal growth media. Data represents mean  $\pm$  SEM.

To determine how tamoxifen could impact cancer cell growth through macrophages, we used PMA-differentiated THP-1 human monocytes (i.e. monocyte derived macrophages) and treated them with tamoxifen. The cells were then incubated for a further 24 hours to generate conditioned medium (CM). We cultured an invasive pancreatic cancer cell line and less invasive epithelial cell line (SUIT-2 and BxPC-3, respectively) and pancreatic stellate cell myofibroblasts, which are responsible for orchestrating tissue fibrosis<sup>39</sup>. Cells were cultured in 1:1 diluted THP-1 CM for 48 hours. Both vehicle and tamoxifen treated THP-1 CM reduced viability of all three cell types. However, there was no difference in viability between the two CM conditions (**Figure 2-12A**). We also treated cancer cells and PSCs with 24 hour CM from 48 hour treated THP-1 (**Figure 2-12B**). Interestingly, SUIT-2, BxPC-3, and PSC viability was mostly maintained when cultured with CM in contrast to 24 hour treatment, yet there

was also no significant difference in cell viability between vehicle THP-1 CM and tamoxifen THP-1 CM. Therefore, we suggest that tamoxifen treatment of macrophages is not associated with pro-tumorigenic growth *in vitro*.

## 2.4 Discussion

Here we provide evidence that tamoxifen modulates macrophage cell mechanics with implications in the tumor microenvironment. Previously we have determined that tamoxifen reduces fibrosis in pancreatic cancer by targeting and deactivating pancreatic myofibroblasts in a biomechanically-dependent manner<sup>‡</sup>. Macrophages, like myofibroblasts, can sense substrate rigidity; on fibrotic-like substrates (stiff and high ligand density), they become more spread and polarized. We find that tamoxifen also works to change macrophage morphology by possibly inhibiting substrate stiffness mechanosensing. Indeed, focal adhesion structure and cytoskeletal dynamics were affected by tamoxifen treatment, as was the ability to migrate on fibronectin-coated surfaces. We further suggest that this biomechanical regulation by tamoxifen is a result of inhibited TLR4 expression and TLR4 agonist sensitivity.

### 2.4.1 Substrate stiffness modulation of macrophage phenotype

Several open questions exist regarding the role of ECM mechanics and structure in altering macrophage phenotype and how to design therapeutics to beneficially reprogram macrophage immunity. It is unclear, for example, if stiff gradients in the tumor microenvironment promote invasion via mechanosensitive podosome elements, and whether modes of migration depend on ECM organization *in vivo*<sup>40</sup>. Van Goethem *et al* used gelled matrices to demonstrate that different ECM substrates regulate macrophage migration mode in 3D<sup>41</sup>. These adaptations may be important in the dynamic changes that occur in the ECM as neoplastic lesions develop. We speculate that given the regulatory nature of the ECM and the marked ECM changes observed in tamoxifen-treated mice, tamoxifen stromal reprogramming via stellate cells in PDAC might also have secondary indirect effects on macrophages in addition to the direct effects outlined here, which has previously been shown in mammary tissue of tamoxifen-treated mice<sup>42</sup>. The inhibited expression of collagen crosslinkers

---

<sup>‡</sup> Unpublished data: Cortes E., Sarper M., Robinson B., Chronopoulos A., Lachowski D., Attwood S., Haining A. W., Karim S., Lieberthal T. J., Morton J., Del Rio Hernandez, A. GPER: A mechano-regulator of pancreatic stellate cells and the tumor microenvironment. 2017.



from PSCs could, for example, alter collagen topology and porosity which regulate macrophage migration behavior.

How modulation of TLR4 expression, signaling, or agonist sensitivity might influence common pathways related to substrate stiffness sensing is unclear. Here we find that tamoxifen produces a more stable actin network while reducing expression of TLR4. Consistent with this, TLR4 stimulation with LPS leads to actin disassembly, particularly at podosomes, likely to free actin for endocytosis<sup>43</sup>. Concurrently, stimulation of macrophages via TLR4 increases expression of integrins and synergizes with integrin-mediated inflammatory responses as a possible link to mechanotransduction pathways<sup>44-48</sup>. These observations thus support a role for TLR4 in enhancing mechanotransduction through integrins; accordingly, TLR4 receptor downregulation or inhibition of the components of the TLR4 pathway would negatively regulate mechanosignaling.

Future work might also examine the effect of tamoxifen not only on primary monocyte-derived macrophages, but also different monocyte subsets. Recent evidence suggests tissue resident yolk-sac derived macrophages rather than inflammatory monocytes are the main drivers of PDAC progression via expression of a transcriptomic program that facilitates fibrosis<sup>49</sup>. We previously used tamoxifen to modulate the pro-fibrosis program of pancreatic stellate cells; whether tamoxifen also modulates the transcriptome of key macrophage populations will be necessary to determine the full therapeutic effects of tamoxifen as a PDAC adjuvant treatment.

#### 2.4.2 Role of TLR4 in PDAC

We found that tamoxifen downregulated TLR4, which is a well-described receptor of the innate immune system and is linked to substrate stiffness-induced pro-inflammatory cytokine production<sup>15</sup>. Tamoxifen has been implicated in TLR4 signaling previously. In a mouse model of brain hemorrhage, tamoxifen abrogated inflammation associated TLR4/NF $\kappa$ B axis upregulation along with downstream cytokines TNF- $\alpha$ , IL-1 $\beta$ , and IL-6, although the cells of origin were not determined<sup>31</sup>. Tamoxifen has also been shown to interfere with dendritic cell differentiation due to inhibited LPS responsiveness, although independent of TLR4 expression at the concentrations used<sup>32</sup>.

While some have suggested using TLR4 agonists as a therapeutic intervention, in many different cancers TLR4 has been found to have both anti-tumor and pro-tumor activities<sup>50,51</sup>. In PDAC, TLR4 is overexpressed, reduces survival, and has been suggested to lead to increased hypoxia inducible factor-1 $\alpha$  (HIF-1 $\alpha$ ) expression. Interestingly, we also found that HIF-1 $\alpha$  was downregulated in tamoxifen treated KPC mice pancreata (**Figure 2-13**)<sup>§</sup>. Ochi *et al.* found that different leukocyte populations in the stroma also overexpress TLR4, and the MyD88-independent TLR4 pathway drives pancreatic carcinogenesis from benign precursor lesions. Inhibition of this TLR4 pathway in dendritic cells prevented carcinogenesis.

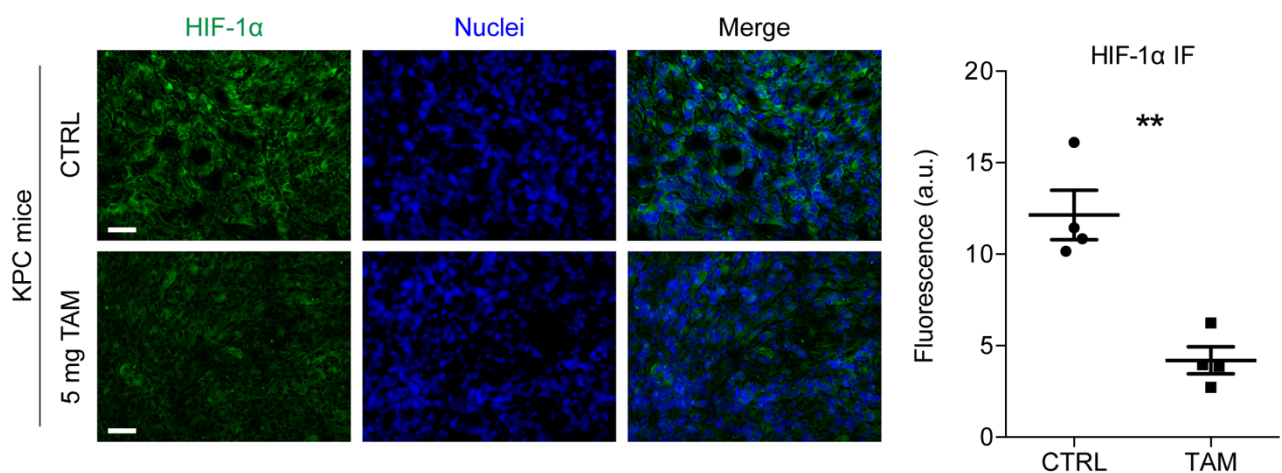


**Figure 2-13.** Expression of HIF-1 $\alpha$  in pancreas tissue of KPC vehicle CTRL mice and mice treated with 5 mg tamoxifen by immunofluorescence (IF). Positively stained area is significantly reduced with tamoxifen treatment. Data represents mean  $\pm$  SEM (n = 4). Scale bar is 50  $\mu$ m. \*\* p < 0.01. Unpublished data.

TLR4 expression independent of the presence of LPS (the cognate ligand of TLR4) or bacterial pathogens is relevant to the tumor environment given that PDAC tumors were found to express high levels of endogenous TLR4 agonists, which stimulate sterile inflammation<sup>52</sup>. However, recent studies found that human pancreatic tumors do in fact contain bacterial derived LPS whereas healthy pancreas does not; intratumoral bacteria can metabolize chemotherapeutics and stimulate TLRs to promote tumor growth<sup>53,54</sup>. Exogenous stimulation of TLR4 may also result from off-target effects of chemotherapy: paclitaxel chemoresistance in breast cancer was traced to stimulation of TLR4 and mobilization of bone marrow derived myeloid

<sup>§</sup> Unpublished data: Cortes E, Robinson E, Sarper M, Lachowski D, Teppo J, Thorpe S, Lieberthal T. J., Iwamoto K., Karim S., Haining A. W., Chronopoulos A., Lee D., Okada-Hatakeyama M., Varjosalo M., Morton J., & Del Rio Hernandez, A. The biomechanical signature of tamoxifen in the architecture of the tumor microenvironment.

progenitors<sup>55</sup>. Liu *et al* also found that in IL-4 polarized macrophages, TLR4/IL-10 signaling induced expression of epithelial to mesenchymal transition (EMT) markers in pancreatic carcinoma cells<sup>56</sup>.

## 2.5 Conclusions

In summary, the benefit of tamoxifen as a chemotherapy may extend beyond its use in targeting myofibroblasts and act more generally to affect other stromal cell type in a mechanically-dependent manner. Here we suggest a potential role for tamoxifen in targeting macrophages based on its observed effect on cell biomechanics: tamoxifen modulates macrophage adhesion/spreading, focal adhesion structures, the cytoskeleton, and migration. Downregulation of TLR4 by tamoxifen is consistent with these biomechanical changes. Future work will focus on the relevance of modulating macrophage mechanobiology with tamoxifen *in vivo*, paracrine interactions with cancer cells and other stromal cell types, and the effects on ECM organization.

## 2.6 Contributions and Acknowledgements

TJL generated hypotheses, designed experiments, conducted experiments, collected and analyzed data. TJL and ADRH wrote and reviewed the manuscript. This study was supported by the European Research Council (ERC 282051). TJL is supported by the James Dyson Foundation. We would like to thank Kevin Woollard for helpful discussions.

## 2.7 References

- 1 Ozdemir, B. C., Pentcheva-Hoang, T., Carstens, J. L., Zheng, X., Wu, C. C., Simpson, T. R., Laklai, H., Sugimoto, H., Kahlert, C., Novitskiy, S. V., De Jesus-Acosta, A., Sharma, P., Heidari, P., Mahmood, U., Chin, L., Moses, H. L., Weaver, V. M., Maitra, A., Allison, J. P., LeBleu, V. S. & Kalluri, R. Depletion of carcinoma-associated fibroblasts and fibrosis induces immunosuppression and accelerates pancreas cancer with reduced survival. *Cancer Cell*. 2014; 25, 719-734.
- 2 Rhim, A. D., Oberstein, P. E., Thomas, D. H., Mirek, E. T., Palermo, C. F., Sastra, S. A., Dekleva, E. N., Saunders, T., Becerra, C. P., Tattersa, I. W., Westphalen, C. B., Kitajewski, J., Fernandez-Barrena, M. G., Fernandez-Zapico, M. E., Iacobuzio-Donahue, C., Olive, K. P. & Stanger, B. Z. Stromal Elements Act to Restrain, Rather Than Support, Pancreatic Ductal Adenocarcinoma. *Cancer Cell*. 2014; 25, 735-747.
- 3 Olive, K. P., Jacobetz, M. A., Davidson, C. J., Gopinathan, A., McIntyre, D., Honess, D., Madhu, B., Goldgraben, M. A., Caldwell, M. E., Allard, D., Frese, K. K., Denicola, G., Feig, C., Combs, C., Winter, S. P., Ireland-Zecchini, H., Reichelt, S., Howat, W. J., Chang, A., Dhara, M., Wang, L., Ruckert, F., Grutzmann, R., Pilarsky, C., Izeradjene, K., Hingorani, S. R., Huang, P., Davies, S. E., Plunkett, W., Egorin, M., Hruban, R. H., Whitebread, N., McGovern, K., Adams, J., Iacobuzio-Donahue, C., Griffiths, J. & Tuveson, D. A. Inhibition of Hedgehog signaling

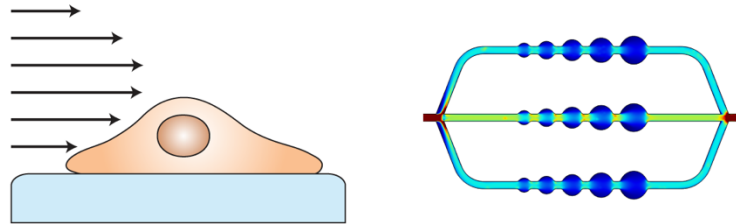
- enhances delivery of chemotherapy in a mouse model of pancreatic cancer. *Science*. 2009; 324, 1457-1461.
- 4 Sarper, M., Cortes, E., Lieberthal, T. J. & Del Rio Hernandez, A. ATRA modulates mechanical activation of TGF-beta by pancreatic stellate cells. *Sci Rep*. 2016; 6, 27639.
  - 5 Chronopoulos, A., Robinson, B., Sarper, M., Cortes, E., Auernheimer, V., Lachowski, D., Attwood, S., Garcia, R., Ghassemi, S., Fabry, B. & Del Rio Hernandez, A. ATRA mechanically reprograms pancreatic stellate cells to suppress matrix remodelling and inhibit cancer cell invasion. *Nat Commun*. 2016; 7, 12630.
  - 6 Ino, Y., Yamazaki-Itoh, R., Shimada, K., Iwasaki, M., Kosuge, T., Kanai, Y. & Hiraoka, N. Immune cell infiltration as an indicator of the immune microenvironment of pancreatic cancer. *Br J Cancer*. 2013; 108, 914-923.
  - 7 Allavena, P., Sica, A., Solinas, G., Porta, C. & Mantovani, A. The inflammatory micro-environment in tumor progression: the role of tumor-associated macrophages. *Crit Rev Oncol Hematol*. 2008; 66, 1-9.
  - 8 Nywening, T. M., Wang-Gillam, A., Sanford, D. E., Belt, B. A., Panni, R. Z., Cusworth, B. M., Toriola, A. T., Nieman, R. K., Worley, L. A., Yano, M., Fowler, K. J., Lockhart, A. C., Suresh, R., Tan, B. R., Lim, K. H., Fields, R. C., Strasberg, S. M., Hawkins, W. G., DeNardo, D. G., Goedegebuure, S. P. & Linehan, D. C. Targeting tumour-associated macrophages with CCR2 inhibition in combination with FOLFIRINOX in patients with borderline resectable and locally advanced pancreatic cancer: a single-centre, open-label, dose-finding, non-randomised, phase 1b trial. *Lancet Oncol*. 2016; 17, 651-662.
  - 9 De Palma, M. & Lewis, C. E. Macrophage regulation of tumor responses to anticancer therapies. *Cancer Cell*. 2013; 23, 277-286.
  - 10 Mantovani, A., Marchesi, F., Malesci, A., Laghi, L. & Allavena, P. Tumour-associated macrophages as treatment targets in oncology. *Nat Rev Clin Oncol*. 2017; 14, 399-416.
  - 11 Beatty, G. L., Chiorean, E. G., Fishman, M. P., Saboury, B., Teitelbaum, U. R., Sun, W., Huhn, R. D., Song, W., Li, D., Sharp, L. L., Torigian, D. A., O'Dwyer, P. J. & Vonderheide, R. H. CD40 agonists alter tumor stroma and show efficacy against pancreatic carcinoma in mice and humans. *Science*. 2011; 331, 1612-1616.
  - 12 Adlerz, K. M., Aranda-Espinoza, H. & Hayenga, H. N. Substrate elasticity regulates the behavior of human monocyte-derived macrophages. *Eur Biophys J*. 2016; 45, 301-309.
  - 13 Patel, N. R., Bole, M., Chen, C., Hardin, C. C., Kho, A. T., Mih, J., Deng, L., Butler, J., Tschumperlin, D., Fredberg, J. J., Krishnan, R. & Koziel, H. Cell elasticity determines macrophage function. *PLoS One*. 2012; 7, e41024.
  - 14 Previtera, M. L., Peterman, K., Shah, S. & Luzuriaga, J. Lipid rafts direct macrophage motility in the tissue microenvironment. *Ann Biomed Eng*. 2015; 43, 896-905.
  - 15 Previtera, M. L. & Sengupta, A. Substrate Stiffness Regulates Proinflammatory Mediator Production through TLR4 Activity in Macrophages. *PLoS One*. 2015; 10, e0145813.
  - 16 Blakney, A. K., Swartzlander, M. D. & Bryant, S. J. The effects of substrate stiffness on the in vitro activation of macrophages and in vivo host response to poly(ethylene glycol)-based hydrogels. *J Biomed Mater Res A*. 2012; 100, 1375-1386.
  - 17 Irwin, E. F., Saha, K., Rosenbluth, M., Gamble, L. J., Castner, D. G. & Healy, K. E. Modulus-dependent macrophage adhesion and behavior. *J Biomater Sci Polym Ed*. 2008; 19, 1363-1382.

- 18 Acerbi, I., Cassereau, L., Dean, I., Shi, Q., Au, A., Park, C., Chen, Y. Y., Liphardt, J., Hwang, E. S. & Weaver, V. M. Human breast cancer invasion and aggression correlates with ECM stiffening and immune cell infiltration. *Integr Biol (Camb)*. 2015; 7, 1120-1134.
- 19 Lachowski, D., Cortes, E., Pink, D., Chronopoulos, A., Karim, S. A., J, P. M. & Del Rio Hernandez, A. E. Substrate Rigidity Controls Activation and Durotaxis in Pancreatic Stellate Cells. *Sci Rep*. 2017; 7, 2506.
- 20 Linder, S. The matrix corroded: podosomes and invadopodia in extracellular matrix degradation. *Trends Cell Biol*. 2007; 17, 107-117.
- 21 Bouissou, A., Proag, A., Bourg, N., Pingris, K., Cabriel, C., Balor, S., Mangeat, T., Thibault, C., Vieu, C., Dupuis, G., Fort, E., Leveque-Fort, S., Maridonneau-Parini, I. & Poincloux, R. Podosome Force Generation Machinery: A Local Balance between Protrusion at the Core and Traction at the Ring. *ACS Nano*. 2017; 11, 4028-4040.
- 22 Labernadie, A., Bouissou, A., Delobelle, P., Balor, S., Voituriez, R., Proag, A., Fourquaux, I., Thibault, C., Vieu, C., Poincloux, R., Charriere, G. M. & Maridonneau-Parini, I. Protrusion force microscopy reveals oscillatory force generation and mechanosensing activity of human macrophage podosomes. *Nat Commun*. 2014; 5, 5343.
- 23 Hind, L. E., Dembo, M. & Hammer, D. A. Macrophage motility is driven by frontal-towing with a force magnitude dependent on substrate stiffness. *Integr Biol (Camb)*. 2015; 7, 447-453.
- 24 del Rio, A., Perez-Jimenez, R., Liu, R., Roca-Cusachs, P., Fernandez, J. M. & Sheetz, M. P. Stretching single talin rod molecules activates vinculin binding. *Science*. 2009; 323, 638-641.
- 25 Haining, A. W., Lieberthal, T. J. & Del Rio Hernandez, A. Talin: a mechanosensitive molecule in health and disease. *FASEB J*. 2016; 30, 2073-2085.
- 26 Pollard, T. D. & Borisy, G. G. Cellular motility driven by assembly and disassembly of actin filaments. *Cell*. 2003; 112, 453-465.
- 27 Borisy, G. G. & Svitkina, T. M. Actin machinery: pushing the envelope. *Curr Opin Cell Biol*. 2000; 12, 104-112.
- 28 Svitkina, T. M., Verkhovskiy, A. B., McQuade, K. M. & Borisy, G. G. Analysis of the actin-myosin II system in fish epidermal keratocytes: mechanism of cell body translocation. *J Cell Biol*. 1997; 139, 397-415.
- 29 Saxena, R. K., Vallyathan, V. & Lewis, D. M. Evidence for lipopolysaccharide-induced differentiation of RAW264.7 murine macrophage cell line into dendritic like cells. *J Biosci*. 2003; 28, 129-134.
- 30 Bafi, N., Saitakis, M., Dogniaux, S., Buschinger, O., Bohineust, A., Richert, A., Maurin, M., Hivroz, C. & Asnacios, A. Human Primary Immune Cells Exhibit Distinct Mechanical Properties that Are Modified by Inflammation. *Biophys J*. 2015; 108, 2181-2190.
- 31 Sun, X., Ji, C., Hu, T., Wang, Z. & Chen, G. Tamoxifen as an effective neuroprotectant against early brain injury and learning deficits induced by subarachnoid hemorrhage: possible involvement of inflammatory signaling. *J Neuroinflammation*. 2013; 10, 157.
- 32 Nalbandian, G., Paharkova-Vatchkova, V., Mao, A., Nale, S. & Kovats, S. The selective estrogen receptor modulators, tamoxifen and raloxifene, impair dendritic cell differentiation and activation. *J Immunol*. 2005; 175, 2666-2675.
- 33 Cerciati, M., Unkila, M., Garcia-Segura, L. M. & Arevalo, M. A. Selective estrogen receptor modulators decrease the production of interleukin-6 and interferon-gamma-inducible protein-10 by astrocytes exposed to inflammatory challenge in vitro. *Glia*. 2010; 58, 93-102.

- 34 Guerra, C. & Barbacid, M. Genetically engineered mouse models of pancreatic adenocarcinoma. *Mol Oncol.* 2013; 7, 232-247.
- 35 Saito, O., Svensson, C. I., Buczynski, M. W., Wegner, K., Hua, X. Y., Codeluppi, S., Schaloske, R. H., Deems, R. A., Dennis, E. A. & Yaksh, T. L. Spinal glial TLR4-mediated nociception and production of prostaglandin E(2) and TNF. *Br J Pharmacol.* 2010; 160, 1754-1764.
- 36 Raetz, C. R., Garrett, T. A., Reynolds, C. M., Shaw, W. A., Moore, J. D., Smith, D. C., Jr., Ribeiro, A. A., Murphy, R. C., Ulevitch, R. J., Fearn, C., Reichart, D., Glass, C. K., Benner, C., Subramaniam, S., Harkewicz, R., Bowers-Gentry, R. C., Buczynski, M. W., Cooper, J. A., Deems, R. A. & Dennis, E. A. Kdo2-Lipid A of *Escherichia coli*, a defined endotoxin that activates macrophages via TLR-4. *J Lipid Res.* 2006; 47, 1097-1111.
- 37 Wenzel, J., Held, C., Palmisano, R., Teufel, S., David, J. P., Wittenberg, T. & Lang, R. Measurement of TLR-Induced Macrophage Spreading by Automated Image Analysis: Differential Role of Myd88 and MAPK in Early and Late Responses. *Front Physiol.* 2011; 2, 71.
- 38 Prakash, H., Nadella, V., Singh, S. & Schmitz-Winnenthal, H. CD14/TLR4 priming potentially recalibrates and exerts anti-tumor efficacy in tumor associated macrophages in a mouse model of pancreatic carcinoma. *Sci Rep.* 2016; 6, 31490.
- 39 Apte, M. V. & Wilson, J. S. Dangerous liaisons: pancreatic stellate cells and pancreatic cancer cells. *J Gastroenterol Hepatol.* 2012; 27 Suppl 2, 69-74.
- 40 Kai, F., Laklai, H. & Weaver, V. M. Force Matters: Biomechanical Regulation of Cell Invasion and Migration in Disease. *Trends Cell Biol.* 2016; 26, 486-497.
- 41 Van Goethem, E., Poincloux, R., Gauffre, F., Maridonneau-Parini, I. & Le Cabec, V. Matrix architecture dictates three-dimensional migration modes of human macrophages: differential involvement of proteases and podosome-like structures. *J Immunol.* 2010; 184, 1049-1061.
- 42 Hattar, R., Maller, O., McDaniel, S., Hansen, K. C., Hedman, K. J., Lyons, T. R., Lucia, S., Wilson, R. S., Jr. & Schedin, P. Tamoxifen induces pleiotrophic changes in mammary stroma resulting in extracellular matrix that suppresses transformed phenotypes. *Breast Cancer Res.* 2009; 11, R5.
- 43 West, M. A., Wallin, R. P., Matthews, S. P., Svensson, H. G., Zaru, R., Ljunggren, H. G., Prescott, A. R. & Watts, C. Enhanced dendritic cell antigen capture via toll-like receptor-induced actin remodeling. *Science.* 2004; 305, 1153-1157.
- 44 Sporn, S. A., Eierman, D. F., Johnson, C. E., Morris, J., Martin, G., Ladner, M. & Haskill, S. Monocyte adherence results in selective induction of novel genes sharing homology with mediators of inflammation and tissue repair. *J Immunol.* 1990; 144, 4434-4441.
- 45 Antonov, A. S., Antonova, G. N., Munn, D. H., Mivechi, N., Lucas, R., Catravas, J. D. & Verin, A. D. alphaVbeta3 integrin regulates macrophage inflammatory responses via PI3 kinase/Akt-dependent NF-kappaB activation. *J Cell Physiol.* 2011; 226, 469-476.
- 46 Caron, E., Self, A. J. & Hall, A. The GTPase Rap1 controls functional activation of macrophage integrin alphaMbeta2 by LPS and other inflammatory mediators. *Curr Biol.* 2000; 10, 974-978.
- 47 Kang, Y. H., Lee, C. H., Brummel, S. E., Newball, H. H. & Forrester, J. Effects of endotoxin on expression of VLA integrins by human bronchoalveolar lavage macrophages. *J Leukoc Biol.* 1995; 57, 624-634.
- 48 Chen, Z., Ding, X., Jin, S., Pitt, B., Zhang, L., Billiar, T. & Li, Q. WISP1-alphaVbeta3 integrin signaling positively regulates TLR-triggered inflammation response in sepsis induced lung injury. *Sci Rep.* 2016; 6, 28841.

- 49 Zhu, Y., Herndon, J. M., Sojka, D. K., Kim, K. W., Knolhoff, B. L., Zuo, C., Cullinan, D. R., Luo, J., Bearden, A. R., Lavine, K. J., Yokoyama, W. M., Hawkins, W. G., Fields, R. C., Randolph, G. J. & DeNardo, D. G. Tissue-Resident Macrophages in Pancreatic Ductal Adenocarcinoma Originate from Embryonic Hematopoiesis and Promote Tumor Progression. *Immunity*. 2017; 47, 323-338 e326.
- 50 Mai, C. W., Kang, Y. B. & Pichika, M. R. Should a Toll-like receptor 4 (TLR-4) agonist or antagonist be designed to treat cancer? TLR-4: its expression and effects in the ten most common cancers. *Onco Targets Ther*. 2013; 6, 1573-1587.
- 51 Huang, B., Zhao, J., Unkeless, J. C., Feng, Z. H. & Xiong, H. TLR signaling by tumor and immune cells: a double-edged sword. *Oncogene*. 2008; 27, 218-224.
- 52 Ochi, A., Nguyen, A. H., Bedrosian, A. S., Mushlin, H. M., Zarbakhsh, S., Barilla, R., Zambirinis, C. P., Fallon, N. C., Rehman, A., Pylayeva-Gupta, Y., Badar, S., Hajdu, C. H., Frey, A. B., Barsagi, D. & Miller, G. MyD88 inhibition amplifies dendritic cell capacity to promote pancreatic carcinogenesis via Th2 cells. *J Exp Med*. 2012; 209, 1671-1687.
- 53 Pushalkar, S., Hundeyin, M., Daley, D., Zambirinis, C. P., Kurz, E., Mishra, A., Mohan, N., Aykut, B., Usyk, M., Torres, L. E., Werba, G., Zhang, K., Guo, Y., Li, Q., Akkad, N., Lall, S., Wadowski, B., Gutierrez, J., Kochen Rossi, J. A., Herzog, J. W., Diskin, B., Torres-Hernandez, A., Leinwand, J., Wang, W., Taunk, P. S., Savadkar, S., Janal, M., Saxena, A., Li, X., Cohen, D., Sartor, R. B., Saxena, D. & Miller, G. The Pancreatic Cancer Microbiome Promotes Oncogenesis by Induction of Innate and Adaptive Immune Suppression. *Cancer Discov*. 2018; 8, 403-416.
- 54 Geller, L. T., Barzily-Rokni, M., Danino, T., Jonas, O. H., Shental, N., Nejman, D., Gavert, N., Zwang, Y., Cooper, Z. A., Shee, K., Thaiss, C. A., Reuben, A., Livny, J., Avraham, R., Frederick, D. T., Ligorio, M., Chatman, K., Johnston, S. E., Mosher, C. M., Brandis, A., Fuks, G., Gurbatri, C., Gopalakrishnan, V., Kim, M., Hurd, M. W., Katz, M., Fleming, J., Maitra, A., Smith, D. A., Skalak, M., Bu, J., Michaud, M., Trauger, S. A., Barshack, I., Golan, T., Sandbank, J., Flaherty, K. T., Mandinova, A., Garrett, W. S., Thayer, S. P., Ferrone, C. R., Huttenhower, C., Bhatia, S. N., Gevers, D., Wargo, J. A., Golub, T. R. & Straussman, R. Potential role of intratumor bacteria in mediating tumor resistance to the chemotherapeutic drug gemcitabine. *Science*. 2017; 357, 1156-1160.
- 55 Volk-Draper, L., Hall, K., Griggs, C., Rajput, S., Kohio, P., DeNardo, D. & Ran, S. Paclitaxel therapy promotes breast cancer metastasis in a TLR4-dependent manner. *Cancer Res*. 2014; 74, 5421-5434.
- 56 Liu, C. Y., Xu, J. Y., Shi, X. Y., Huang, W., Ruan, T. Y., Xie, P. & Ding, J. L. M2-polarized tumor-associated macrophages promoted epithelial-mesenchymal transition in pancreatic cancer cells, partially through TLR4/IL-10 signaling pathway. *Lab Invest*. 2013; 93, 844-854.

### Chapter 3: A multishear microfluidic device for determining cell adhesion strength



Integrin attachments to the extracellular matrix (ECM) are the crucial links between a cell and its environment. Perturbation of integrin attachments by changing substrate stiffness can induce phenotypic changes in adherent cells. The traction forces generated by cells is therefore a determinant of phenotypic homeostasis which may be disrupted in disease states such as cancer. Thus, it is beneficial to understand the strength of cell adhesion and how therapeutics modulate cell traction forces. Here we develop a new microfluidic device for determining cell adhesion strength. In contrast to previous devices, this relies on channel width non-uniformity to test multiple shear stresses under a single flow rate. The device was modeled using COMSOL and tested with macrophages. We speculate that this device could be used for further interrogation of focal adhesion dynamics under shear stress force application and testing of chemotherapeutic adjuvants that target cell mechanobiology pathways.



### 3.1 Introduction

Substrate stiffness is now understood as an important driver of cell behavior from stem cell differentiation to cancer development<sup>1-3</sup>. The substrate stiffness and composition can differentially regulate integrin-mediated signaling<sup>3</sup>; however, it should be noted that, particularly in *in vitro* environments, substrates do not apply forces to the cells: it is cell-generated traction forces that allows for focal adhesion maturation and focal adhesion protein phosphorylation. Thus, cell adhesion strength is an important parameter for understanding cell biomechanics and mechanobiology as well as the influence of substrate mechanics. In fibrotic cancers such as pancreatic ductal adenocarcinoma (PDAC) and hepatocellular carcinoma (HCC), myofibroblasts become activated by the tissue stiffness and further perpetuate fibrosis by secreting extracellular matrix (ECM) and mechanically activating and responding to latent growth factors such as transforming growth factor  $\beta$  (TGF- $\beta$ )<sup>4,5</sup>. Our group has previously investigated regulators of stromal remodeling that target these activated myofibroblasts such as all-trans retinoic acid (ATRA) and tamoxifen<sup>6</sup>. In both cases, the traction forces of pancreatic stellate cells (PSCs) and hepatic stellate cells (HSCs) on polyacrylamide gels is reduced under drug treatment<sup>6\*\*</sup>. Regulation of traction forces is associated with changes in focal adhesion dynamics in these studies. In particular, tamoxifen-treated macrophages exhibited reduced recruitment of talin, a focal adhesion protein and mechanosensor, and inhibited actin polymerization (**Chapter 2, Section 2.3.3**).

Several microfluidic approaches for determining cell adhesion strength have been described in which fluid flow applies sufficient shear stress to detach cells. The first of such were constant width linear microfluidic channels with rectangular cross-sections<sup>7,8</sup>. Because of fixed channel geometry, shear stress variation for a given fluid can only be achieved by controlling the flow rate, which varies linearly with shear stress. Subsequent work utilized these linear channels with flow rate variation or multiplexing linear channels with different lengths or widths to achieve variable pressure drops<sup>9-13</sup>. Determining adhesion strength in these channels requires stepwise ramping of flow rates which may bias later (higher) flow rate measurements due to the accumulated effect of previously applied shear. Depending on the cell type

---

\*\* Effects of ATRA on HSCs and tamoxifen on both HSCs and PSCs are unpublished.

and ramp schedule, early low flow rate measurements may induce a response that confounds later measurements; leukocytes for example can rearrange their cytoskeleton within seconds in response to chemokines<sup>14</sup>. Additionally, it is difficult to make comparisons between experiments that use different ramp protocols because the length of the time intervals for a single flow rate may influence the apparent critical shear stress for detachment.

Alternatively, rectangular cross section channels can be tapered or gradually widened to adjust the velocity of the fluid under a constant volumetric flow rate, thereby adjusting shear stress spatially rather than temporally<sup>15-19</sup>. Variations of this concept may involve variable channel height or non-rectangular cross-sections<sup>20</sup>. For many of these geometry changes, computation of wall shear stress may involve trivial adjustments to equations governing microfluidic flow. However, to precisely map areas within microfluidic channels during microscopy to the corresponding shear stress value, it may be necessary to include an additional field finder grid for image registration<sup>15</sup> or whole device imaging with a motorized stage<sup>16</sup>.

In this work, we describe an alternative channel geometry to apply multiple shear stresses to adherent cells using single flow rates with simple image registration. We demonstrate proof-of-concept development of the device and suggest further uses for such a device.

## 3.2 Materials and Methods

### 3.2.1 Device fabrication

Microfluidic channels composed of PDMS were fabricated using standard soft photolithography techniques. The overall process is depicted in **Figure 3-1**. Silicon molds were fabricated in-house.

The following process was used to fabricate SU-8 molds and PDMS microfluidic channels:

1. First, SU-8 2050 photoresist (A-Gas EM, Warwickshire, UK) was spin coated onto a 4" silicon wafer at 500 rpm 15 sec, 2000 rpm 30 sec which creates ~75  $\mu\text{m}$  thick features. Bubbles formed during the pouring process can remain after spin coating, thus disrupting the homogeneity of the thin film. SU-8 2050 is very

viscous (~6x the viscosity of honey) and should be poured as close to the surface of the silicon as possible. Only a small volume of photoresist is required.

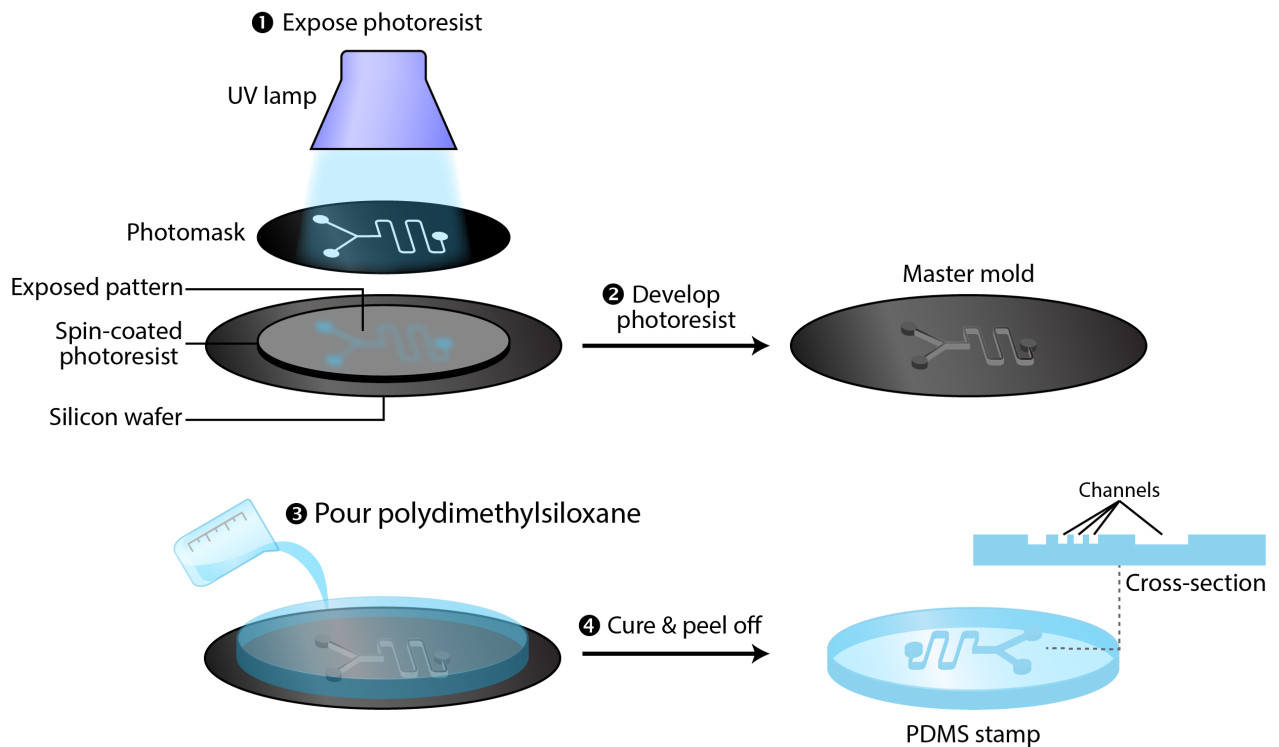


**Figure 3-1.** Fabrication of microfluidic channels using photolithography. (1) SU-8 photoresist is spin-coated onto a silicon wafer, soft baked, and exposed to UV light through the photomask. (2) After hard baking, uncrosslinked photoresist that had not been exposed to UV light is dissolved by a developer. (3) PDMS base and crosslinker (10:1) are mixed thoroughly and poured over the mold. (4) After degassing the PDMS to remove bubbles, the PDMS can be cured at various temperatures and times. The PDMS can be demolded and bonded to glass or other substrate to form channels.

- The wafer was soft baked at 80°C for 20 min to evaporate the photoresist solvent.
- Resist was exposed to UV light (Karl Suss MBJ3 mask aligner Garching, Germany) under a 50,800 dpi laser printed photomask (Fineline Imaging, Colorado Springs, CO) for 30 sec.
- After a 5 min post-exposure bake at 80°C, the wafer was developed in propylene glycol monomethyl ether acetate (Sigma-Aldrich, St. Louis, MO). Both the post-exposure bake and soft bake time/temperature are crucial to maintain resist structures that do not delaminate or crack<sup>21</sup>.

- The mold was then hard baked at 90°C for 5 minutes to strengthen the resist and anneal any cracks. Heating steps should ideally be ramped to reduce thermal stress in SU-8 layers.

Features on the SU-8 mold were 75  $\mu\text{m}$  thick as measured by a Dektak profilometer. Photomask and SU-8 mold are shown in **Figure 3-2**. PDMS (Sylgard 184, Dow Corning) base was mixed 10:1 with crosslinker and poured over the master mold. Following curing at 80°C for 60 min, the PDMS stamp was removed. Holes were punched in the inlet and outlet ports with a 2 mm biopsy punch (Miltex, York, PA). PDMS and glass were sonicated for 10 min in distilled water, then washed with isopropyl alcohol and distilled water. PDMS was bonded to glass by oxygen plasma exposure at 0.4 mbar for 12 seconds at 3.5 power. Devices were sterilized by UV exposure ( $\lambda = 265 \text{ nm}$ ) for at least an hour prior to use for culturing cells.

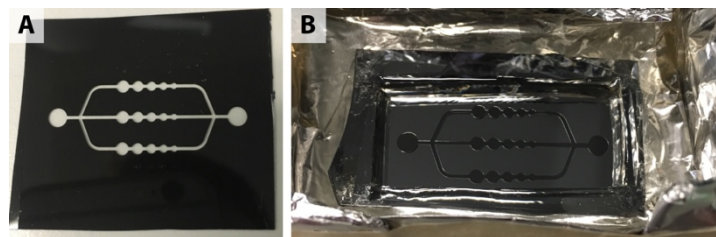


**Figure 3-2.** Mask and mold required to reproduce PDMS channels. (A) Laser printed photomask with channel design. UV exposure through photomask crosslinks the photoresist, resulting in an SU-8 mold (B).

### 3.2.2 Cell culture

RAW264.7 murine macrophages were maintained in Dulbecco's Modified Eagle's Medium (DMEM) with 4.5 g/L glucose, L-glutamine, 10% fetal bovine serum (FBS; Sigma Aldrich), and 1% penicillin/streptomycin. After device bonding and sterilization, channels were coated with 10  $\mu\text{g}/\text{mL}$  fibronectin for 1 hour at 37°C and washed with at least 2 mL PBS. Cells were collected and suspended at  $2 \times 10^6 \text{ mL}^{-1}$ . A high concentration is required given the small volume of the microfluidic channels. This was found to be sufficient to populate surfaces with enough cells for quantification, yet remain single separated cells. The cell solution was pipetted into the inlet ( $\sim 20 \mu\text{L}$ ). Devices were placed in a sterile chamber humidified by moist kimwipes to prevent the devices from drying and placed in a 37°C incubator overnight.

### 3.2.3 Experimental set-up and Imaging

Microfluidic chips were removed from the incubator and inlet and outlet tubing (Cole-Parmer, London, UK) prefilled with PBS were inserted into the ports taking care not to introduce bubbles, the presence of which can significantly disrupt cell adhesion. Inlet tubing was connected to a 50 mL syringe filled with PBS and fitted into a syringe pump cassette (Harvard Apparatus, Holliston, MA). Brightfield imaging was conducted on a Nikon Ti-E with an environmental chamber (37°C, 5% CO<sub>2</sub>). Stage positions were initialized for each well centroid. Images were taken at these locations within the microfluidic channel once every 30 seconds for 2 minutes. The sequence of images was arranged such that wells of the same diameter in each channel were captured before proceeding to the larger diameter wells. One sequence of images (i.e. 15 locations) requires under 10 seconds to complete. The first image in the series was captured without the application of shear to initialize cell number. After, (at  $t \approx 10$  sec) the flow rate of PBS was increased by the syringe pump as noted. To quantify cell density, image stacks were imported into ImageJ and cropped to a 400  $\mu\text{m} \times 400 \mu\text{m}$  area. Cell numbers were counted manually.

### 3.2.4 COMSOL simulations

Incompressible laminar no-slip ( $\vec{u} = 0$  at the walls) fluid flow within microfluidic channels was modeled in COMSOL Multiphysics 5.1 (Burlington, MA) using a water dynamic viscosity of  $8.90 \times 10^{-4}$  Pa·s and default laminar flow constitutive equations representing Navier-Stokes incompressible laminar flow. The inlet boundary condition was set to laminar inflow at a rate of 15 mL/min while outlet pressure was set to 0 Pa. The model was discretized with a physics controlled triangular mesh using the fine setting. The planar velocity map was taken from a slice along the middle of the channel (37.5  $\mu\text{m}$  height) and the wall shear stress was taken from the bottom of the channel. Area averaged shear stress was calculated in MATLAB.

## 3.3 Results

### 3.3.1 Device design

The microfluidic device is symmetric in design and contains three identical channels. In each channel, there are five equally spaced circular reservoirs/openings (i.e. a resistance “well”) of increasing diameter from 1 mm to 2 mm in 0.25 mm increments (**Figure 3-3A**). Using the Ohm’s law analogy of fluidic resistance, we can apply the

relation  $\Delta P = QR$ , where  $\Delta P$  is the pressure drop,  $Q$  is the flow rate, and  $R$  is fluidic resistance (i.e. analogy to  $\Delta V = iR$ ). To maintain equal volumetric flow rate ( $Q$ ) across all five wells within a channel, the fluid velocity is higher in the smaller diameter wells. Although the channels are equal in design, the middle channel is shorter than the other two; as a result,  $R$  is lower in the middle channel and the fluid velocity under a constant  $\Delta P$  is increased (**Figure 3-3B**). The wall shear stress is a direct result of the velocity map with the highest shear stress occurring in the small circular openings of the middle channel (**Figure 3-3C**). In **Figure 3-3D** we plot the shear stress map of the bottom channel along the dotted line in **Figure 3-3C** to show the successive decrease in shear stresses with increasing circular diameter (blue line).

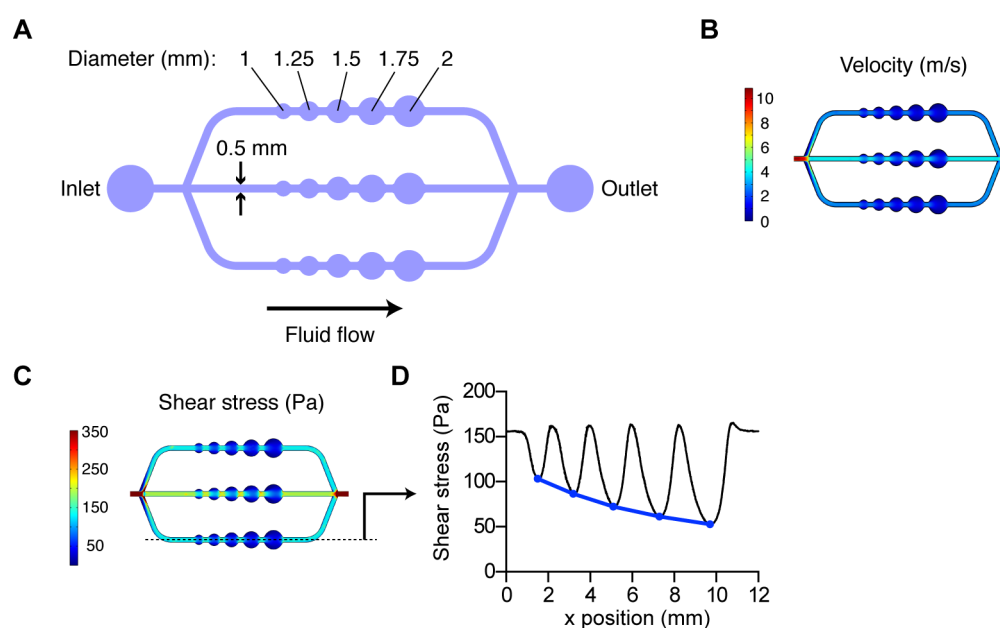


**Figure 3-3.** Design of variable shear microfluidic device. **(A)** The device contains three channels that contain circular widenings (“wells”) with increasing diameters from 1 mm to 2 mm. **(B)** Velocity profile at the plane mid-way between the ceiling and floor of the channels ( $Q = 15$  mL/min). **(C)** Wall shear stress profile and **(D)** average shear stress along the dotted line. Simulations were computed in COMSOL Multiphysics 5.1 with the laminar flow module using a height of  $75\ \mu\text{m}$ .

The benefit of this design for applying controlled shear stress to attached cells is twofold. Instead of a linear gradient, the wells allow discrete regions of increasing shear stress with a single flow rate. With one channel and five wells, five shear stresses can be achieved at the center of each circle; with multiple channels of different lengths, up to an additional five shear stress values per channel can be achieved. In this particular design, the upper and lower channels are identical, which can be used to verify internal device consistency.

A drawback of irregularly shaped channels is a non-uniform shear stress distribution. For example, the shear stress increases exponentially from the circle center along  $x$  and decays along  $y$  towards the wall. For the purposes of optimal data collection, a large field of view is preferable in order to capture as many adherent cells as possible; however, all cells within the data collection region should be exposed to approximately the same shear stress if a single value is used. To investigate this further, we define a square region centered within each circular well with widths between 100  $\mu\text{m}$  and 600  $\mu\text{m}$  to establish optimal boundaries (**Figure 3-4A**). Shear stresses were spatially averaged within increasing width squares and plotted with their standard deviations (SD) (**Figure 3-4B**). As the square width increases, wall effects become more significant and the average shear stress drops. Smaller wells are more susceptible to wall effects due to the proximity of the walls, and the variability in shear stress is significant for 600  $\mu\text{m}$  square areas. A 400  $\mu\text{m}$  square provides a large enough field of view to capture a representative population of cells seeded at a sufficient density without much variability. As a measure of shear stress heterogeneity in 400  $\mu\text{m}$  squares, we compute the coefficient of variation (CV), which is  $\sim 6\%$  in all cases at this flow rate (**Figure 3-4C**). The shear stress averages in 400  $\mu\text{m}$  regions for all wells is plotted in **Figure 3-4D**. Note that, with one flow rate, 10 different discrete regions of shear stress can be achieved, spanning values from 50 Pa to 150 Pa.

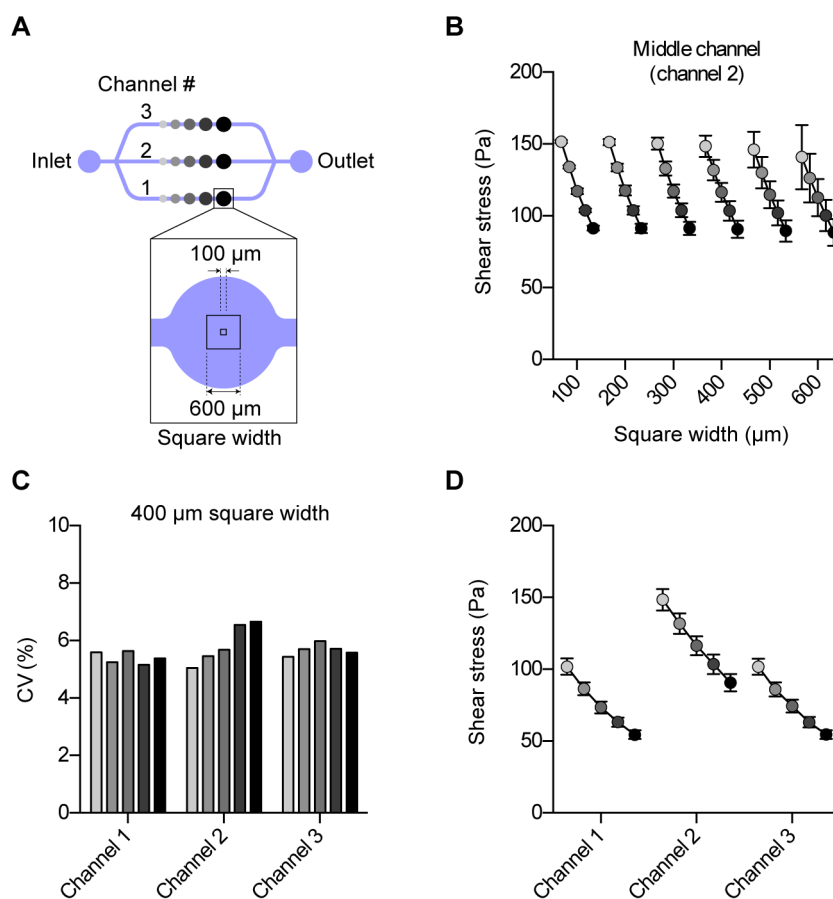


**Figure 3-4.** Uniformity of shear stress in wells. **(A)** Notation and color scheme used in subsequent panels. Wells of increasing size are given increasingly dark grey values. Square regions with widths between 100  $\mu\text{m}$  and 600  $\mu\text{m}$  are centered within each well. **(B)** Spatially averaged shear stress values within each square region of channel 2. **(C)** Coefficient of variation (CV) for shear stress values averaged within a 400  $\mu\text{m}$  square in channel 2. **(D)** Average shear stress values within each well of all three channels using a 400  $\mu\text{m}$  area. Data represents mean  $\pm$  SD.

### 3.3.2 Adhesion strength of RAW264.7 macrophages

To demonstrate the functionality of the device, surfaces were coated with fibronectin and seeded with macrophages. Cells were allowed to attach overnight prior to moving to a temperature controlled Nikon Ti-E microscope and assembled with tubing as described in **Section 3.2.1**. Lu *et al.* used a relatively high shear stress to detach WT NR6 fibroblasts in linear channels coated with fibronectin, finding linear detachment at a constant shear stress of  $\sim 270$  Pa over 12 minutes<sup>8</sup>. Christ *et al.* in contrast found the mean cell adhesion strength of NIH3T3 fibroblasts seeded on fibronectin to be in the range of  $\sim 120$  Pa over 3 minutes of a stepwise ramp<sup>11</sup>. Fibroblast adhesion on glass is typically weaker with a  $\tau_{50}$  of 80 Pa (ref 12). Given the differences in morphology and cell spread area between fibroblasts and macrophages, a lower shear stress range was selected. Macrophage detachment in a cropped region of channel 2



well 2 is shown in **Figure 3-5A**. As expected, cells that had a larger cell spread area demonstrated a longer retention time. The number of detached cells in each well and shear stress reveals a linear correlation (**Figure 3-5B**).

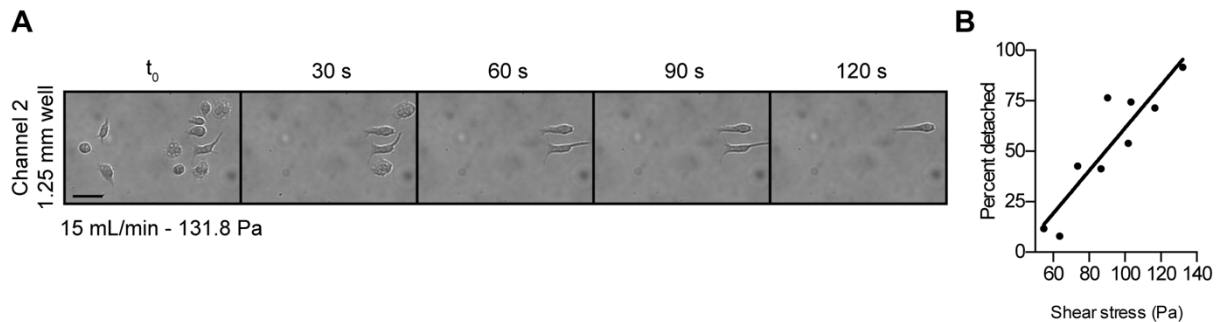


**Figure 3-5.** Detachment of RAW264.7 macrophages in microfluidic channels under shear. **(A)** Detachment of cells in the 1.25 mm diameter well of channel 2 (using notation of **Figure 3-4A**) over the 2 min acquisition period. Scale bar is 50  $\mu\text{m}$ . **(B)** Representative relationship between number of detached cells at the end of 2 min and shear stress in one device.

### 3.4 Discussion

In this study, we demonstrate the proof-of-concept utility of a multishear adhesion strength microfluidic device. This microfluidic device allows for the development of many shear stress regimes across the device with a single flow rate and easy image registration of those areas with the cell locations. If necessary, the device could be modified to include a wider range of shear stresses available by incorporation of additional wells and/or by changing the resistance of individual channels by changing channel length. We suggest that this device can be used to assess the effect of therapeutics that target cell traction forces or focal adhesion dynamics and structure. This device is readily amenable to a more detailed analysis of focal adhesion dynamics under shear by, for example, total internal reflectance microscopy (TIRF), provided the PDMS is bonded to a coverslip substrate.

We also suggest this could be a platform for studying force application on a whole-cell scale. Studying how applied force affects mechanosensitive elements in the cell is typically restricted to tweezer instruments where beads attached to cell surface proteins are actuated with known forces (e.g. magnetic, optical, or acoustic tweezers)<sup>22-24</sup>, or by single molecule atomic force microscopy on isolated proteins<sup>25</sup>. Applied shear stress under flow may also be a method for introducing force to subcellular elements via transmission of shear stress throughout the cell. If we consider a non-motile cell, traction forces are balanced by the opposite forces exerted

by the substrate (**Figure 3-6**, upper panels). These forces are transmitted across integrin-substrate attachments and through to focal adhesion adapter proteins and the cytoskeleton. For an applied shear stress that does not detach the cell, an additional compensatory force is required at the substratum (**Figure 3-6**, lower panels), which redistributes apparent traction forces in magnitude and direction. On the molecular scale, in the case of traction forces that are parallel to the applied shear, the fluid flow acts as an additional force across the elements of the actomyosin apparatus (**Figure 3-6**, lower inset). Unidirectional shear stress allows for different in- and out-of-plane focal adhesion strains, given that the cell attachment points are in tension upstream and in compression downstream<sup>26</sup>.

Typically, microfluidic devices built for cell culture under the application of shear investigate genomic and morphological changes that occur under prolonged exposure to shear (i.e. hours – days). Shorter timescale experiments might be used for investigating leukocyte rolling on the endothelium, for example<sup>27</sup>. We suggest instead that short time scale shear stress application to adherent cells might be used as a method of subjecting focal adhesions to additional loads in addition to endogenous actomyosin contraction to investigate mechanobiological phenomena. Over longer timescales, integrin clustering and mobility might also be observed.

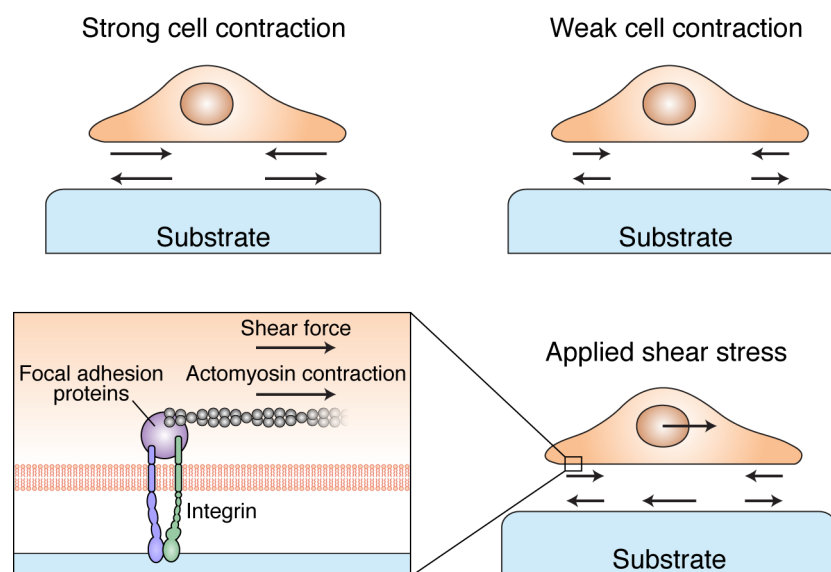


**Figure 3-6.** Proposed model for utilization of the device as a force applicator. Cell-generated traction forces are balanced by the opposite force by the substrate. Application of shear stress redistributes these forces for a cell in translational equilibrium. Shear stress is transmitted through the cell to the cell-substrate contacts (i.e. integrin attachments), which in turn transmits forces across to the cytoskeleton.

In summary, we designed and tested a multishear microfluidic device for assessing cell adhesion strength and propose uses in testing therapeutics and observing focal adhesion dynamics under force application.

### 3.5 Contributions and Acknowledgements

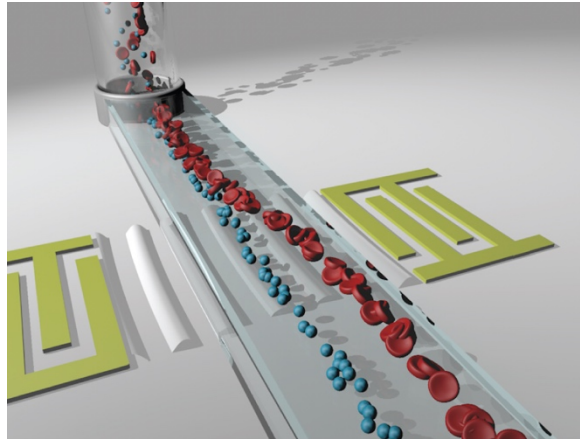
TJL generated designed and generated the prototype, simulated with COMSOL, conducted experiments, collected and analyzed data. This study was supported by the European Research Council (ERC 282051). TJL is supported by the James Dyson Foundation.

### 3.6 References

- 1 Engler, A. J., Sen, S., Sweeney, H. L. & Discher, D. E. Matrix elasticity directs stem cell lineage specification. *Cell*. 2006; 126, 677-689.
- 2 Levental, K. R., Yu, H., Kass, L., Lakins, J. N., Egeblad, M., Erler, J. T., Fong, S. F., Csiszar, K., Giaccia, A., Wenginger, W., Yamauchi, M., Gasser, D. L. & Weaver, V. M. Matrix crosslinking forces tumor progression by enhancing integrin signaling. *Cell*. 2009; 139, 891-906.
- 3 Paszek, M. J., Zahir, N., Johnson, K. R., Lakins, J. N., Rozenberg, G. I., Gefen, A., Reinhart-King, C. A., Margulies, S. S., Dembo, M., Boettiger, D., Hammer, D. A. & Weaver, V. M. Tensional homeostasis and the malignant phenotype. *Cancer Cell*. 2005; 8, 241-254.
- 4 Sarper, M., Cortes, E., Lieberthal, T. J. & Del Rio Hernandez, A. ATRA modulates mechanical activation of TGF-beta by pancreatic stellate cells. *Sci Rep*. 2016; 6, 27639.
- 5 Leight, J. L., Wozniak, M. A., Chen, S., Lynch, M. L. & Chen, C. S. Matrix rigidity regulates a switch between TGF-beta1-induced apoptosis and epithelial-mesenchymal transition. *Mol Biol Cell*. 2012; 23, 781-791.
- 6 Chronopoulos, A., Robinson, B., Sarper, M., Cortes, E., Auernheimer, V., Lachowski, D., Attwood, S., Garcia, R., Ghassemi, S., Fabry, B. & Del Rio Hernandez, A. ATRA mechanically reprograms pancreatic stellate cells to suppress matrix remodelling and inhibit cancer cell invasion. *Nat Commun*. 2016; 7, 12630.
- 7 Usami, S., Chen, H. H., Zhao, Y., Chien, S. & Skalak, R. Design and construction of a linear shear stress flow chamber. *Ann Biomed Eng*. 1993; 21, 77-83.
- 8 Lu, H., Koo, L. Y., Wang, W. M., Lauffenburger, D. A., Griffith, L. G. & Jensen, K. F. Microfluidic shear devices for quantitative analysis of cell adhesion. *Anal Chem*. 2004; 76, 5257-5264.
- 9 Young, E. W., Wheeler, A. R. & Simmons, C. A. Matrix-dependent adhesion of vascular and valvular endothelial cells in microfluidic channels. *Lab Chip*. 2007; 7, 1759-1766.
- 10 Chau, L., Doran, M. & Cooper-White, J. A novel multishear microdevice for studying cell mechanics. *Lab Chip*. 2009; 9, 1897-1902.
- 11 Christ, K. V., Williamson, K. B., Masters, K. S. & Turner, K. T. Measurement of single-cell adhesion strength using a microfluidic assay. *Biomed Microdevices*. 2010; 12, 443-455.

- 12 Christophis, C., Grunze, M. & Rosenhahn, A. Quantification of the adhesion strength of fibroblast cells on ethylene glycol terminated self-assembled monolayers by a microfluidic shear force assay. *Phys Chem Chem Phys*. 2010; 12, 4498-4504.
- 13 Booth, R., Noh, S. & Kim, H. A multiple-channel, multiple-assay platform for characterization of full-range shear stress effects on vascular endothelial cells. *Lab Chip*. 2014; 14, 1880-1890.
- 14 Samstag, Y., Eibert, S. M., Klemke, M. & Wabnitz, G. H. Actin cytoskeletal dynamics in T lymphocyte activation and migration. *J Leukoc Biol*. 2003; 73, 30-48.
- 15 Plouffe, B. D., Njoka, D. N., Harris, J., Liao, J., Horick, N. K., Radisic, M. & Murthy, S. K. Peptide-mediated selective adhesion of smooth muscle and endothelial cells in microfluidic shear flow. *Langmuir*. 2007; 23, 5050-5055.
- 16 Gutierrez, E. & Groisman, A. Quantitative measurements of the strength of adhesion of human neutrophils to a substratum in a microfluidic device. *Anal Chem*. 2007; 79, 2249-2258.
- 17 Rupprecht, P., Gole, L., Rieu, J. P., Vezy, C., Ferrigno, R., Mertani, H. C. & Riviere, C. A tapered channel microfluidic device for comprehensive cell adhesion analysis, using measurements of detachment kinetics and shear stress-dependent motion. *Biomicrofluidics*. 2012; 6, 14107-1410712.
- 18 Huang, C., Smith, J. P., Saha, T. N., Rhim, A. D. & Kirby, B. J. Characterization of microfluidic shear-dependent epithelial cell adhesion molecule immunocapture and enrichment of pancreatic cancer cells from blood cells with dielectrophoresis. *Biomicrofluidics*. 2014; 8, 044107.
- 19 Kim, M. J., Doh, I., Bae, G. Y., Cha, H. J. & Cho, Y. H. Cell-matrix adhesion characterization using multiple shear stress zones in single stepwise microchannel. *Applied Physics Letters*. 2014; 105.
- 20 Kim, H. W., Han, S., Kim, W., Lim, J. & Kim, D. S. Modulating wall shear stress gradient via equilateral triangular channel for in situ cellular adhesion assay. *Biomicrofluidics*. 2016; 10, 054119.
- 21 Keller, S., Blagoi, G., Lillemose, M., Haefliger, D. & Boisen, A. Processing of thin SU-8 films. *Journal of micromechanics and microengineering*. 2008; 18, 125020.
- 22 Fan, Z., Sun, Y., Di, C., Tay, D., Chen, W., Deng, C. X. & Fu, J. Acoustic tweezing cytometry for live-cell subcellular modulation of intracellular cytoskeleton contractility. *Sci Rep*. 2013; 3, 2176.
- 23 Choquet, D., Felsenfeld, D. P. & Sheetz, M. P. Extracellular matrix rigidity causes strengthening of integrin-cytoskeleton linkages. *Cell*. 1997; 88, 39-48.
- 24 Wang, N., Butler, J. P. & Ingber, D. E. Mechanotransduction across the cell surface and through the cytoskeleton. *Science*. 1993; 260, 1124-1127.
- 25 Neuman, K. C. & Nagy, A. Single-molecule force spectroscopy: optical tweezers, magnetic tweezers and atomic force microscopy. *Nat Methods*. 2008; 5, 491-505.
- 26 Ferko, M. C., Bhatnagar, A., Garcia, M. B. & Butler, P. J. Finite-element stress analysis of a multicomponent model of sheared and focally-adhered endothelial cells. *Ann Biomed Eng*. 2007; 35, 208-223.
- 27 Lieberthal, T. J., Cohen, H. C. & Kao, W. J. Poly(ethylene glycol)-containing hydrogels modulate alpha-defensin release from polymorphonuclear leukocytes and monocyte recruitment. *J Biomed Mater Res A*. 2015; 103, 3772-3780.

## Chapter 4: Engineering a microfluidic diagnostic device for extracellular vesicle isolation and analysis<sup>††</sup>



Pancreatic cancer is the fourth-leading cause of cancer related mortality and is predicted to be the second leading cause of cancer death by 2030. Widely regarded as a death sentence, pancreatic cancer carries a 5-year survival rate of only 3% in the UK, and this figure has not changed over the past four decades due to lack of specific therapies and inability to detect it early. Recently, submicron-sized vesicles (exosomes and microvesicles) shed by the tumor and found in the bloodstream, have emerged as powerful circulating biomarkers possessing extremely high sensitivity and specificity, thus paving the way for a new era of non-invasive cancer diagnostics. However, the current process of extracellular vesicle isolation and detection is not only highly inefficient, but also technically challenging and inaccessible to hospital laboratories, clinical facilities, and resource-poor settings. To address technological constraints limiting extracellular vesicle utilization as a clinical biomarker, we develop methods in acoustophoretic separation of vesicles and detection of vesicular membrane proteins using a graphene field effect transistor.

---

<sup>††</sup> Selected data in this chapter adapted from Tsang D. H. K., Lieberthal T. J., Del Rio Hernandez, A., & Klein, N. Chemically functionalised graphene FET with double conductance minima for the microfluidic sensing of exosomes. *Submitted*.

## 4.1 Introduction

In **Chapter 3**, microfluidic channels were used to culture cells and apply fluid shear stress. However, microfluidics has been used in numerous applications ranging from on-chip PCR, immunoassays, cell sorting, biochemical analysis, drug screening, *in vitro* modeling, and many more. Microfabricated channels made of polydimethylsiloxane (PDMS) via soft photolithography manufacturing were invented and popularized by George Whitesides in the late 1990s and 2000s following a trend of miniaturization<sup>1,2</sup>. Published work in microfluidics, microelectromechanical systems (MEMS), and micro total analysis systems ( $\mu$ TAS) has grown markedly since: microfluidics publications have increased ~5-fold between 2003 and 2013 (ref 3). A benefit of microfluidics and miniaturized systems is a low operating volume, which is conducive to development of diagnostic technologies that may utilize small volumes of biofluids.

In **Section 1.6: PDAC biomarkers and diagnostics**, the potential of exosomal biomarkers for early PDAC diagnostics was discussed and several engineered solutions for exosomal isolation and detection were reviewed. In particular, various exosomal proteins (e.g. glypican-1 and MIF) and nucleic acids (e.g. miRNAs) have been identified as having promising potential as biomarkers or therapeutic targets in PDAC. However, difficulties in isolating and analyzing exosomes poses an obstacle in widespread clinical use. In this chapter, we describe acoustophoresis and graphene technologies and employ MEMS technology, microfluidics, and rapid prototyping for applications in PDAC exosomal diagnostics. We develop acoustophoresis methods for biofluid processing and a graphene biosensor for exosome sensing as solutions to the shortcomings of conventional extracellular vesicle processing and analysis equipment. In this introductory section, we introduce the principles governing acoustic waves and graphene field effect transistors.

### 4.1.1 Surface acoustic waves and interdigital transducers

We adopted a method of particle separation called acoustophoresis, which operates via generation of acoustic (sound) waves. Acoustic waves adopt various modes of travel through a medium depending on the orientation of the source and the properties of the medium (**Figure 4-1**). Two major classifiers are waves that travel throughout the bulk of the medium or just the surface layers. Naturally, waves that are confined

to the surface of a plate are called surface acoustic waves (SAWs). For the purposes of developing sensors, three modes of SAWs are employed, named after the people who formalized the mathematics: Rayleigh, Love, and Lamb<sup>4</sup>. Rayleigh waves are a combination shear waves in the vertical (z) direction, which propagate along the plate (x) direction due to a longitudinal wave. Displacement (strain) of the surface decays rapidly in the z direction; Rayleigh waves only penetrate to the depth of a wavelength. Lamb (plate flexural) waves are a case of Rayleigh waves in which the thickness (z) of the plate is on the order of the wavelength (low frequencies), in which case the wave propagates through the bulk in symmetric or antisymmetric configurations.

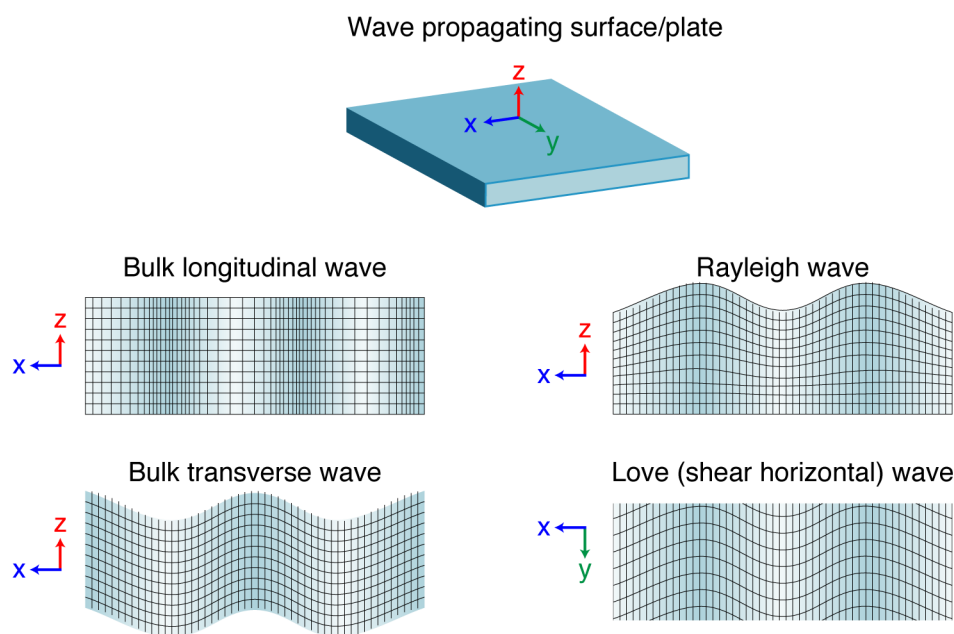


**Figure 4-1.** Modes of acoustic waves and their orientations. Rayleigh waves propagate along the surface of the plate due to combined longitudinal (x) and vertical (z) shear waves. Love waves are shear horizontal waves that propagate within a thin guided layer (e.g. SiO<sub>2</sub> or PMMA) that is deposited on top of the surface.

SAWs can be generated by depositing thin film interdigital transducer (IDT) electrodes on a piezoelectric surface. Piezoelectric materials have the property of electromechanical coupling in which electric fields can induce mechanical strain in the material and *vice versa*. This property arises from a crystal structure that lacks a center of inversion symmetry<sup>5</sup>. Common piezoelectric crystals used for SAW generation are quartz, lithium niobate (LiNbO<sub>3</sub>), and lithium tantalate (LiTaO<sub>3</sub>). Piezoelectric thin films of lead zirconate titanate (PZT), zinc oxide (ZnO), and aluminum nitride (AlN) on which IDTs are deposited can also be used. The IDTs are comb-like in design and contain interwoven digits or “fingers.” Upon excitation of the electrodes at the resonant

frequency and establishment of an electric field, mechanical displacements on the order of 1 nm are induced in the fingers, thereby creating acoustic waves<sup>6</sup>.

The first IDTs used for the propagation of surface elastic waves were invented by White and Voltmer in 1965 with a thin film of cadmium sulfide on quartz<sup>7</sup>. Utilization of SAW technology is widespread; it is used for filters in integrated circuits, wireless telecommunications technology, signal processing, and touch screens<sup>8-10</sup>. Another early use for IDTs is to non-destructively test defects (e.g. cracks) in materials. By transmitting the acoustic signal across the surface, defects are detected via changes in the wave properties<sup>11</sup>. Similarly, SAW chemical sensors operate by creating a transmitter and receiver of waves in a delay line configuration. Between the transmitter and receiver, a chemical recognition (sensing) element is placed. As the SAWs propagate across the surface, changes in mass due to the sensing element results in a frequency shift or insertion loss of the wave, which is recorded via the receiving element<sup>12</sup>. Rayleigh SAW sensors cannot operate in fluid because the evanescent wave efficiently leaks into the fluid as a compression wave; however, this makes it useful for actuation. Love SAWs can be employed in liquid environments, given that particle motion in the wave is within the plane of the surface and is not attenuated by the liquid above it<sup>12</sup>.

For maximum SAW generation in any application, IDTs should be excited by an RF signal at their resonant frequency ( $f_R$ ), which is a function of the SAW wavelength ( $\lambda$ ) and velocity ( $v$ ) of sound in the medium:  $f_R = v/\lambda$ . The most straightforward IDT design features constant digits and spacing and therefore a constant wavelength and resonant frequency. Both chirped and slanted IDTs are variations in IDT design in which the resonant frequency and wavelength can be varied. Focused IDTs may also be used to narrow and focus the acoustic aperture (**Figure 4-2**). Such variations in IDT design are tuned for the application; chirped IDTs can be utilized in cases where a wide bandwidth is required at a range of excitation frequencies. Similarly, slanted IDTs allow spatial variation in the transmitted SAW depending on the frequency applied to them; in an acoustofluidic application, this can be used to continuously change the direction of particles or droplets by modifying the frequency<sup>13</sup>. Other standard design modifications can be useful in controlling reflections and wave directionality such as single phase unidirectional transducers, distributed acoustic reflecting transducers, and floating electrode unidirectional transducers<sup>13</sup>.



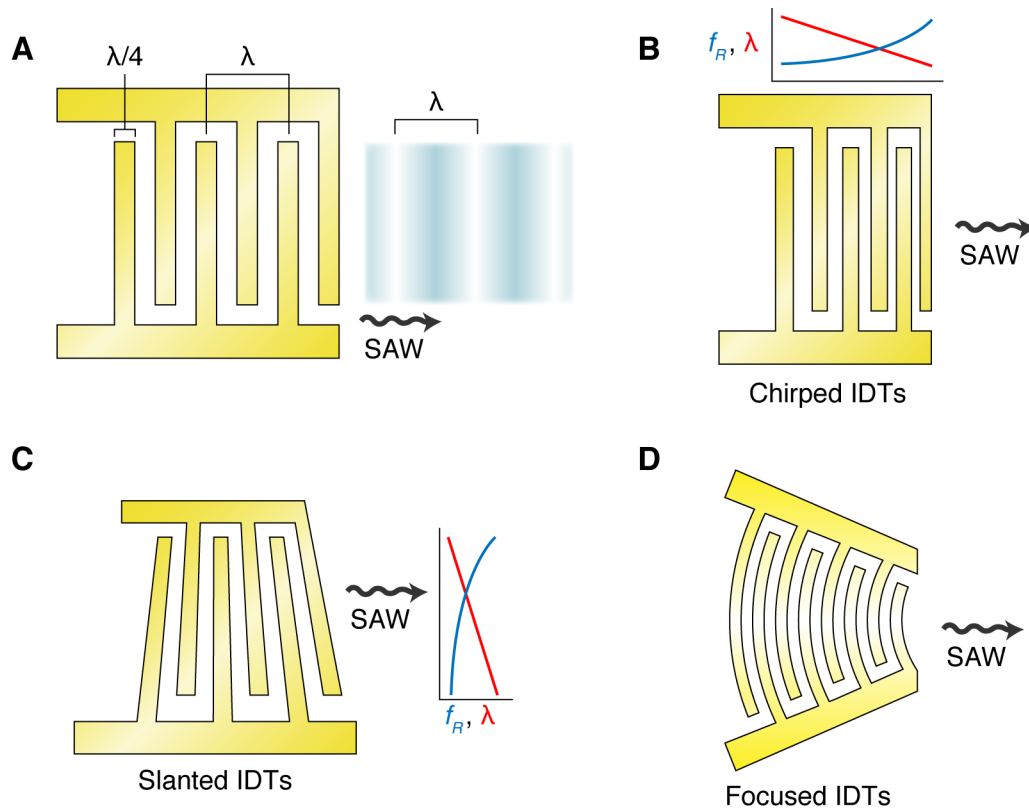


**Figure 4-2.** Common modifications of IDTs. **(A)** The simplest IDT design is a constant digit and frequency transducer. The digit size and spacing determine the wavelength ( $\lambda$ ) of the SAW. **(B)** Chirped IDTs have variable digit widths. By exciting chirped IDTs with a variable resonant frequency ( $f_R$ ), waves with corresponding variable wavelengths can be created. The effect of this design is to increase the allowable bandwidth, meaning the frequency of the SAW can be tuned for the purpose. **(C)** Slanted IDTs allow spatial control of the SAW aperture by choosing a resonant frequency that excites the IDTs with a particular width. **(D)** Focused IDTs narrow the acoustic aperture and amplifies the signal. Focused IDTs can also be chirped.

#### 4.1.2 Acoustophoresis

The coupling of a Rayleigh SAW into liquid can be useful for acoustophoresis (“sound separation”) of particles suspended in the liquid. For this application, Rayleigh SAWs can be further classified as traveling or standing (TSAW and SSAW, respectively), which are depicted in **Figure 4-3**. The IDT configuration of SSAWs is identical to the two-port set-up of SAW sensors and filters. However, instead of powering one pair of IDTs to generate a wave and using the other pair of IDTs to collect the signal, SSAWs are created by powering both sets of IDTs. The IDTs then emit traveling waves in opposing directions, which then interfere to create a standing wave. When there is only one pair of IDTs, a traveling wave is created. Standing waves can also be established with one IDT if the wave is reflected back either by a dedicated reflector or an acoustically reflective bonded material.

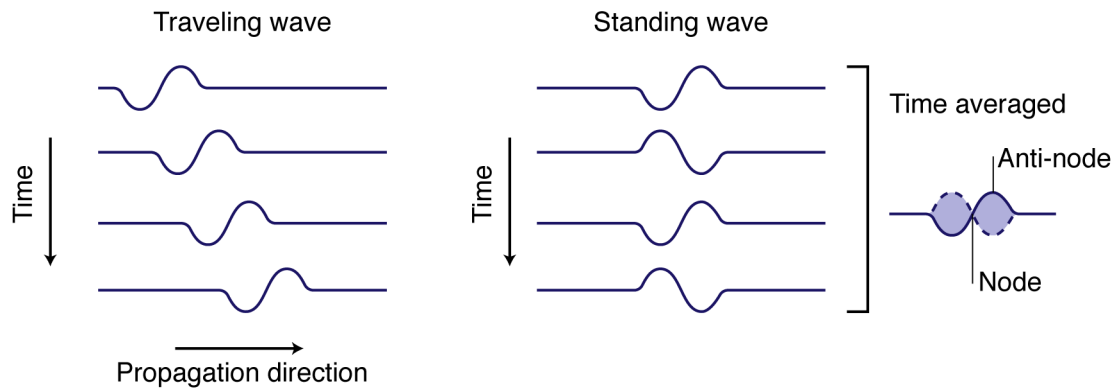


**Figure 4-3.** Simplified depiction of traveling and standing waves. In both cases of SAWs, a particle within the surface of the plate follows an elliptical path except for at the nodes of standing waves where there is no displacement. Traveling waves are created by one pair of IDTs (from the left-hand side). Standing waves are created by having an IDT on both the right- and left-hand sides. Time-averaged SSAWs contain a node, in which no movement occurs, and an antinode.

As discussed in **Section 4.1.1**, Rayleigh SAWs are a combination of vertical shear and longitudinal waves (see also **Figure 4-1**). Materials that are bonded on top or cover the piezoelectric substrate generally cause unwanted attenuation of the vertical shear wave and an insertion loss. Wave energy couples efficiently into liquid to create pressure distributions that can be used for manipulating particle position. In the case of SSAWs, leaking of the SAW into the liquid creates nodes and antinodes in the liquid as well.

Particles subjected to SSAWs can migrate towards nodes depending on the acoustic radiation force, which in turn depends on the characteristics of the wave (e.g. frequency), the interfacial interactions (e.g. fluid-solid boundary) and fluid properties. Importantly, the acoustic radiation force is proportional to the cube of the radius of the particle, described by the acoustic radiation force equation (Equation 1)<sup>14</sup>:

$$F = -\frac{2}{3}\pi \frac{P^2 r^3 \beta_m}{\lambda} \phi(\beta, \rho) \sin(2kx) \quad (1)$$

where  $\phi(\beta, \rho) = \frac{5\rho_p - 2\rho_m}{2\rho_p + \rho_m} - \frac{\beta_p}{\beta_m}$  and

where  $P$  is the pressure amplitude,  $r$  is the particle radius,  $\beta$  is the compressibility of the medium ( $m$ ) and particle ( $p$ ),  $\rho$  is the density,  $k$  is the wave vector,  $\lambda$  is the wavelength, and  $x$  is the distance from a node.

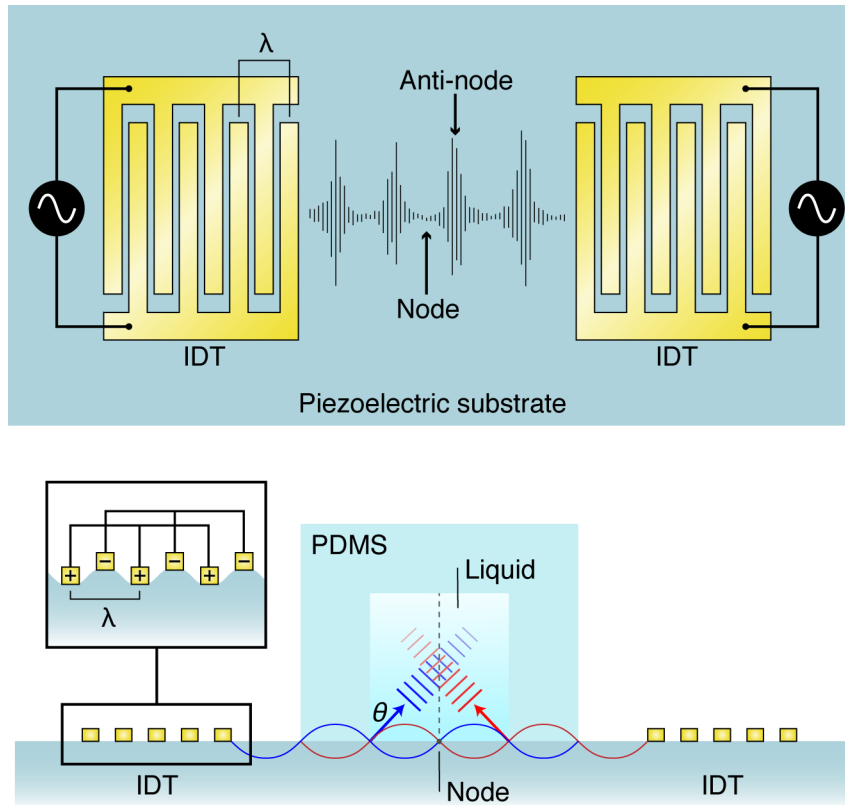


**Figure 4-4.** Generation of standing surface acoustic waves (sSAWs) with interdigital transducers (IDTs). The frequency/wavelength of SSAWs created depends on the pitch ( $\lambda$ ) of IDT digits, thereby creating periodic pressure nodes and antinodes. Both IDTs are excited by RF signal at the resonant frequency of the IDTs as determined by the pitch and velocity of the wave in the substrate. Bottom: side view of IDTs with PDMS microfluidic channel bonded in-between them. Inset: oscillations in the IDT digits due to the electric field set up by RF excitation creates the acoustic wave. Each IDT creates a traveling wave that combines with the opposing wave to create a standing wave. Upon encountering the liquid environment in the microfluidic channel, waves refract into the liquid as a longitudinal compression wave at the Rayleigh angle ( $\theta$ ) and recombine with the opposing wave. The node that forms as a result of interference from the opposing waves in the liquid is directly above the original node in the plate. Note that waves will suffer an insertion loss due to the microfluidic element (not depicted). Figure adapted in part from Ding et al. *Lab Chip*. 2013; 13, 3626-3649 (ref 6).

With this method, particles suspended in fluid are separated in a size-dependent manner (according to Equation 1) by SSAWs generated from IDTs patterned on a  $\text{LiNbO}_3$ . Upon application of electrical current, IDTs produce ultrasonic traveling waves; if paired with an opposing IDT, interference creates a standing wave with pressure nodes and antinodes inside microfluidic channels (**Figure 4-4**). Depending on particle size and acoustic radiation force, particles may be forced into nodes. In combination with microfluidic flows, these nodal lines can be redirected such that particles are separated from a mixture. Thus, acoustophoresis can act as a size-based filtration device.

Because circulating tumor cells are larger than other blood cells, acoustophoresis has previously been employed as a high pass filter to isolate circulating tumor cells from whole blood in tandem with microfluidics<sup>15</sup>. Microfluidic channels can be bonded between IDTs, and the SSAWs propagating orthogonal to the direction of fluid flow allows continuous separation of particles. Lee *et al* (2015) demonstrated the first use of acoustophoresis to separate extracellular vesicles from cells in microfluidic channels<sup>16</sup>. A microfluidic channel was positioned between two IDTs such that the channel contained two nodal lines parallel to the fluid flow. Larger microvesicles (size cut-off 300 nm) and/or cells (size cut-off 450 nm) migrated towards the nodes, thus leaving the vesicles in the center of the channel to be collected. Using polystyrene beads of different sizes, they determined that this method was highly efficient (>90% recovery) and could be used with unprocessed packed red blood cell units. However, because the acoustophoresis acts as a low-pass filter in this application, extracellular vesicles in addition to serum proteins are isolated. Taller *et al.* (2015) also used SAWs, not for acoustophoresis, but to produce Rayleigh waves that are scattered within a liquid droplet to produce an acoustic streaming force, high Reynolds numbers, and mechanical stress gradients<sup>17</sup>. This was used to lyse pancreatic tumor derived exosomes from which exosomal RNA can be collected and analyzed.

One limitation of SSAWs is that nodal lines need to be precisely aligned parallel to the fluidic channel. Further, for a single node device, the separation distance is limited to one quarter of the wavelength. For a two-node device, the nodes are separated by one half of a wavelength within the channel. However, this limitation can be overcome by using tilted SSAWs (tSSAWs) in which the IDTs and therefore nodal lines are at an angle relative to the direction of the microfluidic channel<sup>15,18</sup>. This allows multiple nodes within a channel and increases separation distance across the entire channel. When particles flow through the nodes, they may be deflected along the angle of the node depending on their size. Larger particles (e.g. red blood cells) will experience a larger acoustic radiation force and be deflected while smaller particles (e.g. extracellular vesicles will pass through the nodes unaffected). Wu *et al.* (2017) recently applied tSSAWs to separate exosomes in two stages: (1) cells were removed from all extracellular vesicles and (2) exosomes and microvesicles were separated. However, like with Lee *et al.* (2015)<sup>16</sup>, exosomes in addition to serum proteins are isolated. It is likely that without additional isolation mechanisms, these protein contaminants could

interfere with further analysis. For applications in which vesicles are used for therapeutic research purposes, these proteins may confound further use. Nevertheless, these reports of using acoustophoresis with low size cut-offs motivates further investigation into SAW-based technology for vesicle processing.

Here we describe acoustophoresis in combination with a graphene biosensor in microfluidic channels to isolate, purify, and detect exosomes. In the first stage, we develop the acoustophoretic mechanism, which creates standing surface acoustic waves and could be used to separate small nanovesicles from other whole blood components. The overall objective is to create a diagnostic chip capable of interrogating the biomarker potential of extracellular vesicle membrane proteins.

#### 4.1.3 Graphene field effect transistors

To address the analysis of vesicular proteins, we developed a sensor based on graphene as a field effect transistor (FET). A FET is a transistor in which an applied electric field induces the movement of either negative charge carriers (electrons) or positive charge carriers (holes) across a semi-conductor. Electron or hole conduction can occur in n-type or p-type semi-conductor channels, respectively. The flow of charge carriers through the channel from the source to the drain is tuned by an additional terminal, called the gate. The gate controls the size and shape of the conduction channel and therefore the current that passes through it. Graphene, a single 2D sheet of  $sp^2$ -hybridized carbon, is an ideal material for transistors and transistor-based sensors due to high thermal stability, high density of electric current, and high tensile strength, among other characteristics<sup>19</sup>. Graphene is the subject of extensive investigations in materials science and electronics; since its introduction in 2004 (ref 20), graphene is posed to revolutionize the electronics industry.

A graphene FET, as with other FETs, includes source (S), drain (D), and gate (G) electrodes. The graphene forms a channel between the source and drain, along which current flows. The gate voltage ( $V_g$ ) is formed between the gate and the source. The magnitude and sign of  $V_g$  modulates the current flow between S and D ( $I_{DS}$ ). Sweeping  $V_g$  and measuring  $I_{DS}$  reveals a characteristic curve resembling a convex parabola (in an  $I_{DS}$  vs  $V_g$  plot). The minimum point in the curve is called the Dirac point, the gate voltage at which an increase or decrease in voltage would increase  $I_{DS}$  and conductivity. Beginning from the Dirac point, a more negative (leftward) change in  $V_g$

increases  $I_{DS}$  due to hole filling conduction whereas a more positive (rightward) change in  $V_g$  increases  $I_{DS}$  due to electron conduction<sup>21</sup>. Naturally, the Dirac point represents the voltage at which electrons and holes are in equilibrium. The symmetry of the  $I_{DS}$ - $V_g$  curve thus reflects the ambipolar nature of graphene (i.e. either n- or p-type conduction). The absolute position of the Dirac point can be shifted by doping the graphene – either donating to or removing electrons from graphene. P-doping thus shifts the curve right while n-doping shifts the curve left.

One area of application of graphene FETs is in the development of sensors. The sensing mechanism relies on the analyte effectively doping the graphene. For example, Kim *et al.* (2013) developed a reduced graphene oxide FET to detect a prostate specific antigen (PSA) complex. Adsorption of the PSA onto the graphene in a basic solution shifts the Dirac point left due to an n-type effect whereas the curve is shifted right under acidic conditions. The basic and acidic pH were selected to be above and below the isoelectric point of PSA, respectively, thereby switching the type of charge carrier. With this sensor, they were able to demonstrate a ~1 fM detection limit<sup>22</sup>. The doping effect is thought to be either a result of direct charge transfer to/from the graphene or due to an electrostatic effect, which produce opposite shifts for a similarly charged particle. In practice however, the apparent sensing mechanism may not be consistent with theoretical predictions<sup>23</sup>.

Thus far, graphene FET sensors have been used in detecting gaseous chemicals, pH, metal ions, nucleic acids, proteins, small molecules, bacteria, and cells<sup>21</sup>. To our knowledge, there are no reports of graphene FETs used as an extracellular vesicle biosensor. We can hypothesize that the interaction between graphene and vesicles would be much the same as the interaction with protein given that vesicles contain proteins within the membrane. The membrane itself may contribute to n-doping of the graphene due to negative charges.

#### 4.1.4 Design considerations

Device considerations for vesicle separation and/or purification must address (1) the complexity of the unprocessed biofluid, (2) difficulty of operation and number of components needed for full functionality, and (3) expected downstream applications of the isolated vesicles. Here we explore these considerations with regard to the proposed acoustophoretic and graphene platform.

1. *Complexity of biofluid.* In addition to extracellular vesicles, whole blood contains a variety of cell types, proteins, and biomolecules. Exclusive purification of the exosome fraction may be desired, for example, in cases where an exosomal membrane protein is also expressed in a blood cell subset, in microvesicles, or exists as a serum protein – all of which could lead to false positive detection. These three main non-protein/lipid constituents (cells, microvesicles, and exosomes) are most readily distinguished by size. Depending on the sensor design and detection modality, reduction in the complexity of the biofluid may be beneficial to increase the usability of the device and prevent confounding information from other blood components. As a general-purpose tool for interrogating extracellular vesicle membrane proteins, size-based separation may facilitate identification of key vesicle subsets involved in diverse physiological processes. Recent field-flow fractionation of extracellular vesicles revealed three vesicle populations distinguished by size and with unique proteomic signatures and biodistribution<sup>24</sup>. Acoustic-based separation can therefore be used to process whole blood and isolate the specific size range of particles under investigation. Some blood components overlap in size with exosomes, such as lipoproteins (5-80 nm) and chylomicrons (100-1000 nm); fortunately, they differ in acoustic contrast factor with exosomes, which makes it possible to separate them using this parameter<sup>25</sup>.
2. *Difficulty of operation and constituent components.* Surface acoustic wave devices integrate well with microfluidic devices due to similar size and same manufacturing methods (photolithography). A major advantage of SAWs is the ability to mechanically manipulate particles and/or fluids in a contact- and label-free manner. This is particularly important for a fluid such as whole blood, which can coagulate and lead to biofouling of surfaces. One early microfluidic device that used a nanomembrane filter for sieving whole blood to collect vesicles clogged after only ~4  $\mu\text{L}$  of filtrate was collected<sup>26</sup>. Label-free methods may also reduce the need for antibodies or functionalized nanoparticles/beads, which – besides introducing further required reagents and expense – make the device more cumbersome to operate and require additional steps and incubation times. The time required for operation is also an important factor in designing new devices, given the long processing times required of conventional ultracentrifugation. Acoustophoretic particle separation and

microfluidic separation techniques in general requires low flow rates, which – depending on the sample size and yield requirements – may limit throughput. For the applications relevant to this work, this depends on the vesicle concentration required to surpass the limit of detection of the biosensor.

3. *Expected downstream applications.* The required yield and purity for downstream applications dictates whether the device may be feasibly used. Off-chip analysis, particularly Western Blot of vesicle lysates, may be confounded by the presence of plasma proteins that are not easily separated from vesicles and is a major concern in the field. Applications in which native or engineered vesicles are used as a therapeutic intervention may require concentration above levels found in blood and a strict plasma protein-free sample. Concentration of vesicles on-chip has largely depended on filtration methods (see **Table 2**, page 38). Immunocapture and release has also been recently reported<sup>27</sup>. However, acoustic methods for separating mixtures of exosomes and microvesicles have demonstrated ~98% purity of isolated exosomes<sup>25</sup>.

Device considerations particular to biosensing also include whether detection is label-free and the limit of detection. Most extracellular vesicle sensors involve a labeling system, conventionally by a tagged secondary antibody for fluorescent or colorimetric detection. However, the most important concerns for a sensor are its sensitivity, limit of detection, and multiplexing capability. Graphene FET biosensors for proteins have demonstrated low limits of detection; thus, we hypothesized that it may improve upon the sensitivity of existing sensors.

For any biosensor, the method of chemical (protein) recognition and the properties of the solvent carrying the analyte must be considered. Chemical recognition of specific proteins for biosensors is almost exclusively achieved with antibodies or antibody derivatives (e.g. Fab fragments) directed against the protein of interest. Aptamers are a notable exception<sup>28</sup>. A secondary consideration is conjugation of the antibody to the surface of the sensor via physical or chemical means.

For a graphene sensor, the solvent in which the analyte (i.e. vesicle) is suspended must be considered due to Debye-Hückel screening, which affects any FET biosensor<sup>29</sup>. In short, the electrostatic gating effect of the analyte can be screened or



shielded from the FET due to the presence of aqueous ions; the graphene is therefore not affected by the analyte due to the more immediate layer of ions covering the surface. The Debye length – the maximum distance at which the analyte can affect the conductivity of the FET – can be analytically determined from the concentration and valence of ions<sup>30</sup>. As ion concentration increases, the Debye length decreases, and biosensing becomes difficult. For 1x PBS, the Debye length is less than 1 nm, which would screen charges for most applications<sup>30</sup>. Thus, an ideal solution should have as low an ion concentration as possible. Additionally, the pH of the solution should be considered. As described in **Section 4.1.3**, the Dirac point shift direction can be controlled by choosing the pH of the solvent above or below the isoelectric point of PSA. A solvent that neutralizes the charges of the analyte would be unhelpful. For this reason, implementation of microfluidics is especially advantageous: the biofluid can be perfused across the surface of the sensor and be replaced with a different fluid with optimal ion concentration and pH.

Given these considerations, we proposed an extracellular vesicle isolation and detection device based on acoustophoresis and a graphene FET biosensor (**Figure 4-5**). Separation is achieved through tSSAWs, which has been shown to remove cells from extracellular vesicles with nearly 100% purity<sup>25</sup>. Vesicles can then be detected via Dirac point shifts on an antibody-conjugated graphene FET.

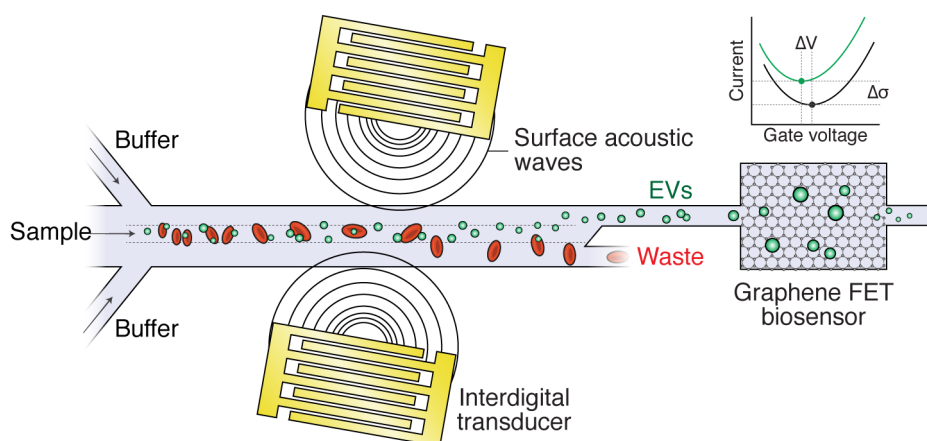


**Figure 4-5.** Schematic detailing the proposed isolation and detection of extracellular vesicles (EVs). Isolation is achieved through SSAW acoustophoresis, which separates vesicles from other whole blood or other biofluid components. Isolates are then detected by an antibody-conjugated graphene FET biosensor where shifts in the Dirac point indicate vesicle binding. Note that in the current prototype, the modules are not housed within the same chip due to substrate incompatibilities.

## 4.2 Materials and Methods

### 4.2.1 Photolithography

Microfluidic channels composed of PDMS were fabricated using an SU-8 mold fabricated as described in detail in **Section 3.2.1**. To create microfluidic channels, PDMS (Sylgard 184, Dow Corning) base was mixed 10:1 with crosslinker and poured over the master mold. Mixing introduces bubbles, so the pre-polymer mix must be degassed in a desiccator for at least 45 min. Following curing at 80°C for 90 min, the PDMS stamp was removed. Holes were punched in the inlet and outlet ports with a 2 mm biopsy punch (Miltex, York, PA). PDMS and glass or lithium niobate surfaces were sonicated for 10 min in distilled water, then washed with isopropyl alcohol and distilled water. PDMS was bonded to glass by oxygen plasma treatment at 0.4 mbar for 12 seconds at 3.5 power. Tygon tubing (Cole-Parmer, London, UK) was fitted into the inlet ports and connected to a syringe pump (Harvard Apparatus, Holliston, MA) via 3 mL glass syringes (Fortuna Optima, Sigma-Aldrich, St. Louis, MO). For low flow rates, glass syringes are required to prevent the effects of plastic compliance. Large (2  $\mu\text{m}$ ) latex beads (Sigma-Aldrich, St. Louis MO) and small (200 nm) latex beads (Invitrogen FluoSpheres<sup>®</sup>, Carlsbad, CA) were used for flow experiments. Microfluidic devices were positioned on a fluorescent microscope for image acquisition.

### 4.2.2 Interdigital transducer fabrication

IDTs were created with photolithography followed by gold evaporation and a lift-off process (**Figure 4-6**). The pitch of the IDT digits, which determines the wavelength of the acoustic wave, varied in the first iterations of the prototype, having a pitch of either 100  $\mu\text{m}$  or 150  $\mu\text{m}$  and different numbers of digits. Such parameters may be optimized with multiphysics modelling software; however, accurate simulations that include interactions between acoustics and complex rheological properties in a microscale regime may require extensive computation.

Standard photolithography techniques were used and optimized for the materials used. The following process was used for photolithography:

1. A photomask was laser printed with 50,800 DPI resolution (FineLine Imaging, Colorado Springs, CO). The resolution requirements of the mask are determined by the resolution of structures. A plastic laser printed photomask at

50,800 DPI can reproduce features down to 7  $\mu\text{m}$ . For higher frequency IDTs, a chrome-quartz mask is required. Chrome-quartz masks are more expensive but can potentially resolve submicron features. Masks used for photolithography are typically printed dark field read right down, which means the features are mirrored and the “ink” is printed on the bottom side of the mask that will be flush with the photoresist. For higher fidelity submicron lithography, electron-beam direct write systems are required<sup>31</sup>.

2. AZ5214E photoresist (MicroChemicals GmbH, Ulm, Germany) was spin coated at 800 rpm 15 sec and 4000 rpm 30 sec on XY-cut 128° double polished 0.5 mm thick lithium niobate (University Wafer, Boston, MA). This is a positive photoresist, which means UV exposed regions are dissolved during the development process.
3. The photoresist on the wafer was soft baked for 90 sec at 110°C.
4. The photoresist was exposed to UV light (Karl Suss MBJ3 mask aligner Garching, Germany) through the photomask for 30 sec. It is crucial that the mask is completely flush with the photoresist; otherwise, gaps in between the mask and photoresist will cause diffraction of the UV light and result in poorly defined structures.
5. The wafer was then hard baked at 110°C for 2 min.
6. Patterns were developed in 1:3 diluted AZ400K developer (AZ Electronic Materials GmbH, Wiesbaden, Germany) for about 45 sec. Development time was highly variable and needed to be adjusted manually. Improper development yields unusable IDTs. If patterns are underdeveloped, photoresists remain in the exposed regions and prevent metals from depositing. If patterns are overdeveloped or if debris interfered with the pattern, metal can be improperly deposited, causing an electrical short between the two IDTs in the pair.

$\text{LiNbO}_3$  crystals are anisotropic, which gives rise to piezoelectricity. Thus, the orientation of the IDTs and the SAWs must be considered. The photomask is oriented such that SAWs would propagate along the +X axis of the wafer, which is the orientation of maximum piezoelectric coupling for this type of  $\text{LiNbO}_3$ . The  $\text{LiNbO}_3$  wafers are typically manufactured as circles with a reference flat edge to indicate the coordinate system. For a 4” wafer, multiple IDTs can be patterned. Wafers can be cut

to size using a dicing saw, or, with less precision, a diamond scribe. Care has to be used to avoid cracking the fragile wafer.

The photolithography process is very sensitive to light, temperature, and timing, which requires optimization based on individual equipment. Because the photoresist should only be exposed to UV light during step 4, all steps are carried out in a yellow room that filters out ambient UV light. Ideally thin film structures should be manufactured in a cleanroom.

The resulting wafer after development is patterned with a photoresist of  $\sim 10\ \mu\text{m}$  except for areas of UV exposure where the photoresist was dissolved. After, an adhesive layer of titanium (10 nm) was evaporated onto the surface of the patterned wafer followed by gold deposition (100 nm) using a Mantis HEX physical vapor deposition system. A lift-off process that removes the gold evaporated onto the photoresist was performed in acetone overnight with periodic gentle agitation, yielding the gold transducers.

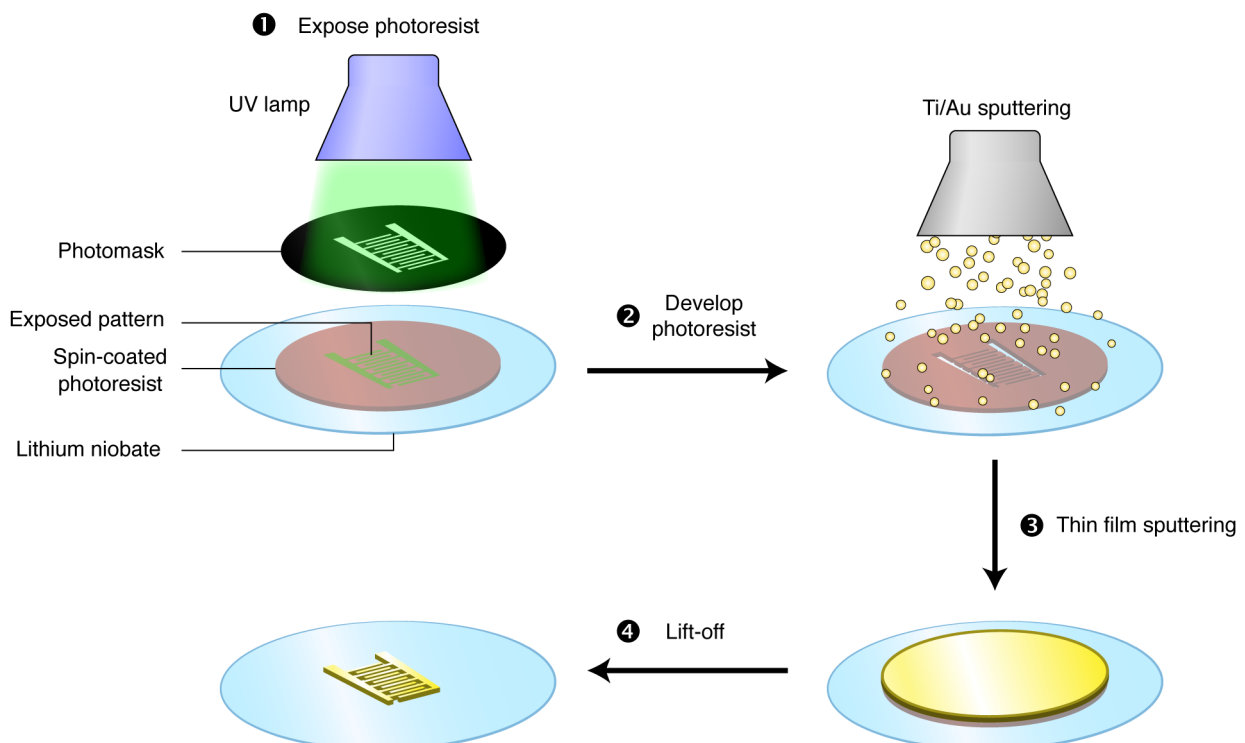


**Figure 4-6.** Fabrication of IDTs with photolithography and thin film deposition. (1) After the photoresist is spin-coated on the substrate, the photoresist is exposed to UV light through the photomask template. (2) The photoresist is then hard baked and developed in a solvent. Areas of the photoresist exposed to UV light are removed. (3) An adhesive layer of titanium (10 nm) and then gold (100 nm) is deposited on the wafer. Both regions of covered and uncovered substrate are sputtered. (4) All photoresist is dissolved by acetone, which also removes any metal that is deposited on top of the resist.

Here we use gold for the bulk of the electrode and titanium for the adhesive layer. Chromium is a common alternative to titanium and aluminum is a common alternative to gold. An ideal thin film metal for IDTs needs to have low electrical resistance. Aluminum is sometimes used because it is less dense than gold and therefore reduces the load on the lithium niobate<sup>5</sup>. This may be important for high frequency (>100 MHz) applications.

Once completed, the electrodes need to be connected to wires. To establish a good connection, wires were first adhered to gold contacts using silver paint. The wires were held in place permanently with a silver epoxy that cures at 80°C. To integrate microfluidic channels and IDTs, PDMS microfluidic channels and lithium niobate were treated with oxygen plasma (0.4 mbar for 12 seconds at 3.5 power). The PDMS was sprayed with a thin layer of ethanol to prevent instantaneous bonding with the lithium niobate. This allows time to align the microfluidic channel under a microscope. For tSSAWs, the angle between the microfluidic channel and the IDTs can be optimized for separation of components by numerical simulation using the drag force and acoustic radiation force<sup>15</sup>. Bonding is complete when the assembly is placed on an 80°C hotplate for at least 1 hour to evaporate the ethanol.

#### 4.2.3 Graphene FET device fabrication

Monolayer chemical vapor deposition (CVD) graphene on 25 µm copper foil (GrollTex) was transferred onto a Si wafer with 300 nm thermal SiO<sub>2</sub> (1–20 Ω.cm and 525 µm thick) via a wet chemical transfer process whereby the copper foil was etched using 0.01 mg/mL ammonium peroxodisulphate solution. A sacrificial poly(methyl methacrylate) (PMMA) layer was used during this process, which was later washed off using dichloromethane. Electrodes (10/50 nm Ti/Au) were subsequently deposited by direct current (DC) magnetron sputtering for the graphene FET source and drain electrodes whereas the back-gate for the graphene FET was applied using conductive silver paint. A polydimethylsiloxane (PDMS) channel (1 cm length, 1 mm diameter) was fabricated and cured for 12 hours at room temperature before being secured on top of the graphene FET surface for microfluidic integration after sample functionalization with a custom-made clamp.

#### 4.2.4 Biosensor functionalization

To functionalize PDMS/glass surfaces with antibodies, surfaces were plasma treated to expose reactive hydroxyl groups. Microfluidic channels were immediately filled with silane-PEG(5K)-NH<sub>2</sub> (ChemQuest Limited, Cheshire, UK) used at 10 mg/mL dissolved in 95% ethanol and left to react at room temperature for 1 hr under agitation. The silane grafts to the surface of glass/PDMS with catalytic amounts of water. Reaction times were kept at 1 hr to prevent polymerization. Channels were then washed with three channel volumes of distilled water and incubated at room temperature with 2.5% glutaraldehyde (Sigma-Aldrich, St. Louis, MO) for 15 min, which couples with the amine group of the PEG molecule, and washed. Glypican-1 antibody (Insight Biotechnology Limited, Middlesex, UK) used at 50 µg/mL in PBS was then introduced to the chambers and incubated for a further 2 hours at room temperature with agitation.

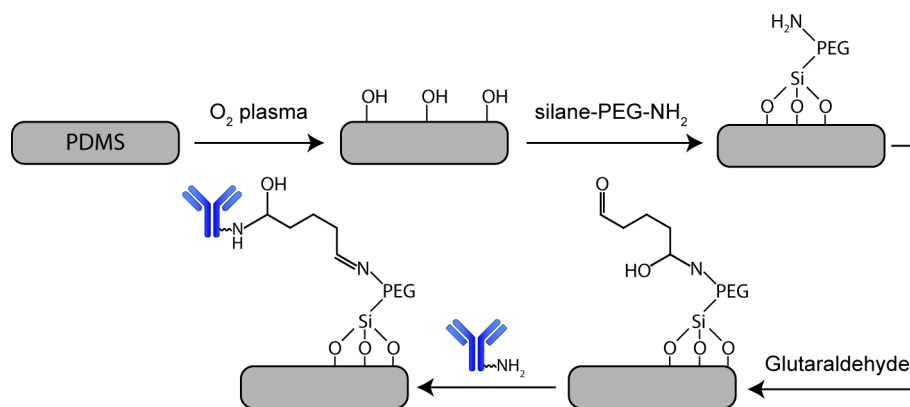


**Figure 4-7.** Antibody functionalization schematic via PEG linker. Note that both PDMS and glass surfaces undergo the same process.

For initial sensitivity tests and proof of concept, microfluidic chambers consisting only of the detection chambers with an inlet and outlet were used. We used 200 nm carboxy terminated polystyrene yellow-green fluorescent beads functionalized with either bovine serum albumin (BSA) or a mix of 20:80 glypican-1:BSA. Beads were conjugated with protein using a 1-ethyl-3-(3-dimethylaminopropyl)carbodiimide hydrochloride (EDC) linker. Solutions of beads were perfused through the chambers and incubated for 5 minutes to let the beads attach. Unattached beads were washed from the channels with PBS. Captured beads were visualized on a fluorescent microscope and counted using an automated ImageJ particle counter. In some cases, the number of captured beads was determined using fluorescent intensity in chambers using a custom written MATLAB script.

Antibody conjugation of the graphene biosensor was achieved as previously described by Kim *et al.* (2013)<sup>22</sup>. Briefly, graphene was incubated with 10 mM 1-pyrenebutanoic acid succinimidyl ester (PBASE) linker in dimethylformamide (DMF) for 2 hrs at room temperature and washed with distilled water. PBASE is a heterobifunctional linker that contains a pyrene group that stacks with graphene by  $\pi$ - $\pi$  overlap and an NHS ester that reacts with primary amines. Antibodies (100  $\mu$ g/mL) were reacted with the NHS ester in PBS pH 8.4 overnight at 4°C. Glycine (100 mM) was used to quench unreacted NHS ester for 30 min at room temperature. Sensors were washed with distilled water and dried prior to use.

Each layer of functionalization of the graphene sensors was characterized by x-ray photoelectron spectroscopy (XPS) with a high-throughput Thermo Fisher K-Alpha<sup>+</sup> spectrometer. Samples containing extracellular vesicles were prepared for XPS by dehydrating them in an ethanol series.

#### 4.2.5 Electrical measurements

DC measurements were carried out using a two-channel Keithley 2636B sourcemeter. For each graphene FET sensor  $V_g$  was swept between -20 and 120 V and was supplied through the back-gate a constant 200 mV source-drain voltage ( $V_{DS}$ ). The source-drain current ( $I_{DS}$ ) was measured for each  $V_g$  point and the gate current ( $I_{gS}$ ) was monitored to ensure negligible leakage current. The graphene FET responses were recorded when ~20  $\mu$ L solutions of phosphate buffered saline (PBS), bovine serum albumin (BSA), or exosomes in PBS were perfused through a microfluidic channel. The exosomes used in this study were lyophilized standards collected from healthy plasma donors using ultracentrifugation and microfiltration (Hansa Biomedical). Exosome standards were reconstituted in de-ionized water according to the manufacturer's instructions.

#### 4.2.6 Collection of extracellular vesicles from cell culture supernatant

Conventional vesicle collection was carried out using ultracentrifugation as described by Théry *et al.* (2006)<sup>32</sup>. Pancreatic epithelial carcinoma cells were cultured in T75 or T175 flasks for 48 h in serum-free conditions. FBS can be used if endogenous bovine vesicles are removed prior to use. To collect vesicles from cell culture supernatant, cells and debris were removed by centrifugation at 2,000  $\times g$  for 5 min and 0.22  $\mu$ m filtered. Vesicles were pelleted at 100,000  $\times g$  for 2 hrs and resuspended in PBS before

a second spin at 100,000  $\times g$  for 2 hrs. Pellets were resuspended in sterile PBS, aliquoted, and stored at  $-80^{\circ}\text{C}$ .

Scanning electron microscopy (SEM) and nanoparticle tracking analysis (NTA) were used to characterize isolated extracellular vesicles. For SEM imaging, aliquots of vesicles were pipetted on cleaned silicon chips, fixed in glutaraldehyde, contrast stained with 1%  $\text{OsO}_4$  for 1 hr, and dehydrated in an ethanol series. Samples were coated with 10 nm chromium and imaged on a Zeiss Sigma 300 microscope operating at an electron acceleration voltage of 5 kV.

NTA is a method of determining the size and concentration of nanoparticles by shining an incident laser light through the sample and determining the particle trajectories upon scattering of the light. The particles undergo Brownian motion, and mean squared displacement is a function of particle size and the viscosity and temperature of the medium.

## 4.3 Results and Discussion

### 4.3.1 IDT fabrication and acoustophoresis

IDTs were fabricated as described in the materials and methods along with the accompanying PDMS microchannel (**Figure 4-8**). Here IDTs were fabricated with a pitch of  $100\ \mu\text{m}$ , which produces the same sized wavelength. The microfluidic channel includes two inlets for sample and sheath that recombine in the central channel along the acoustophoretic region. Directly after the acoustophoretic region, the central channel splits into two (an upper and lower) for separation of particles (**Figure 4-8B**). The thickness of the PDMS walls that contain the channel are kept as narrow as possible in order to limit attenuation of the SSAW.

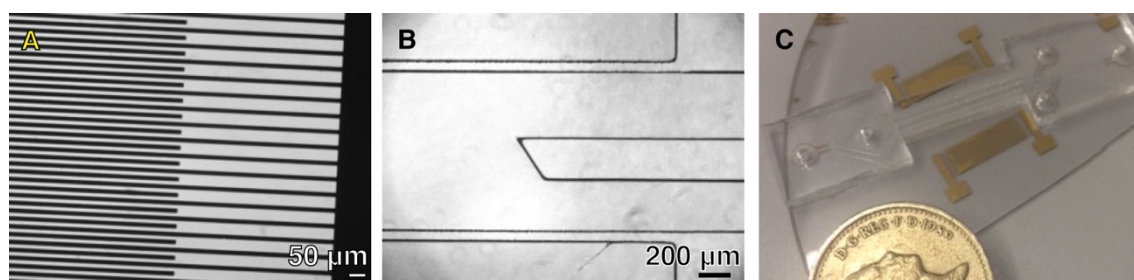


**Figure 4-8.** Brightfield micrographs of (A) IDTs and (B) the microfluidic channel. Black regions of the IDTs correspond to gold thin films. (C) Assembled device with PDMS microchannel bonded between IDTs.



Red latex beads (2  $\mu\text{m}$ ) were used to visualize fluid flow in PDMS microchannels and the effect of the acoustic field. The beads are uniformly and randomly distributed in the channels when the acoustic field is off, and particles flow in the upper channel of the microfluidic device (**Figure 4-9A** and **B**).

The theoretical resonant frequency for 100  $\mu\text{m}$  IDTs is about 39.8 MHz using the speed of sound in  $\text{LiNbO}_3$  of 3980 m/s. This was confirmed by determining the frequency of minimum insertion loss for each IDT pair. When excited by the signal generator, the IDTs produced a standing field which patterned beads into nodes, whereas anti-nodes were not occupied by beads (**Figure 4-9C**). As expected, the distance between successive nodes was 50  $\mu\text{m}$ , a half wavelength. In this configuration, the PDMS channel was aligned parallel to the IDTs, meaning nodal lines would also be parallel to the direction of flow.

Acoustophoresis of 2  $\mu\text{m}$  beads

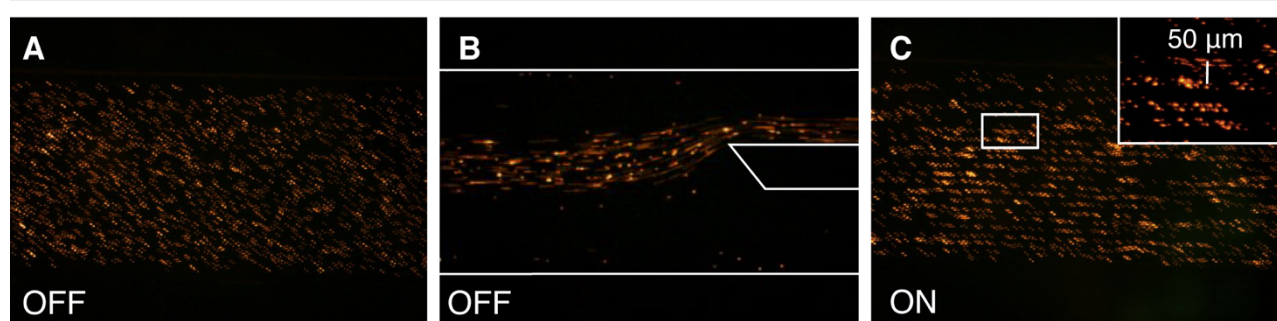


**Figure 4-9.** Distribution of beads in microfluidic channels. **(A)** Under static or flow conditions, beads are randomly and uniformly distributed in the channel. **(B)** Fluidic resistance biases flow towards the upper channel under flow conditions. **(C)** Establishment of the acoustic field creates nodal lines which attract particles. For  $\lambda = 100 \mu\text{m}$  SSAWs, nodes should be separated by a half-wavelength (50  $\mu\text{m}$ ). Inset: measured distance between consecutive nodes is 50  $\mu\text{m}$ .

When the microfluidic channel is angled with respect to the IDTs, it is possible to deflect particles towards an outlet<sup>25</sup>. Actuation of 2  $\mu\text{m}$  beads is sufficient to remove whole blood cell populations, given that red blood cells are 6-8  $\mu\text{m}$  in diameter. Thus, we demonstrate particle actuation within microfluidic channels; further modifications may be used to remove cells from blood as a pre-processing element prior to downstream analysis with a detection module.

#### 4.3.2 PDMS functionalization with antibodies

Detection of extracellular vesicles has been demonstrated in various forms (see **Table 2**, page 38). Initially we sought to improve upon immunoaffinity/immunocapture techniques already established with microfluidic channels or LOC diagnostics in order

to create a extracellular vesicle detection module within the microfluidic device. Specifically, we introduced a strategy to enhance antibody conjugation to PDMS and/or glass surfaces in which antibodies are immobilized onto PDMS and glass surfaces using a polyethylene glycol linker, after which vesicles are stained and detected. When activated by oxygen plasma, PDMS exposed hydroxyl groups will couple to the silane. Addition of antibodies with free primary amino residues will be crosslinked onto the surface using glutaraldehyde, resulting in covalent antibody grafting via a PEG linker (**Figure 4-7**). We expected that this strategy will result in a more stable antibody functionalization. The PEG linker also serves to reduce non-specific protein/vesicle adsorption and non-productive steric interactions between antibodies and vesicles. Once the antibodies are captured and washed to remove any unbound vesicles, a vesicle-specific dye (carboxyfluorescein succinimidyl diacetate ester) would flow through an inlet upstream of the reaction chambers. Detection of fluorescent vesicles could occur in “detection chambers” using a fluorescent microscope.

To first characterize the conjugation process, a fluorescent antibody was conjugated to surfaces with the PEG linker or without (DMSO; physio-adsorption of the antibody) and channels were perfused with fluorescent beads functionalized with bovine serum albumin (BSA). Because the antibody does not target BSA, adsorption of beads represents non-specific adhesion. We found that while the conjugation process does not greatly enhance the number of antibodies presented on the surface in comparison to direct adsorption, the number of BSA that non-specifically adhered was reduced (**Figure 4-10A, B, and C**), possibly due to the action of the PEG linker.

Next, we functionalized surfaces with an antibody and compared non-specific attachment of BSA beads with specific attachment of beads conjugated to the corresponding antigen of the antibody. We selected glypican-1 as the antigen and conjugated glypican-1 to beads in a solution of BSA spiked with 20% glypican-1. As discussed previously, glypican-1 has been identified as a potential exosomal biomarker for PDAC. Glypican-coated beads were preferentially attached to the microfluidic surfaces (**Figure 4-10D and E**).

The benefit of this strategy is that the immunocapture antigen could be used for detection or, through a separate pair of primary and secondary antibodies, further

membrane proteins could be stained and detected. However, given the apparent sensitivity of this method and the drawbacks – including the need for a microscope, spatial variations in immunocapture, and novelty of the detection method – we decided to investigate other sensors that have not been explored for the use of extracellular vesicle biosensing; namely, a graphene sensor.

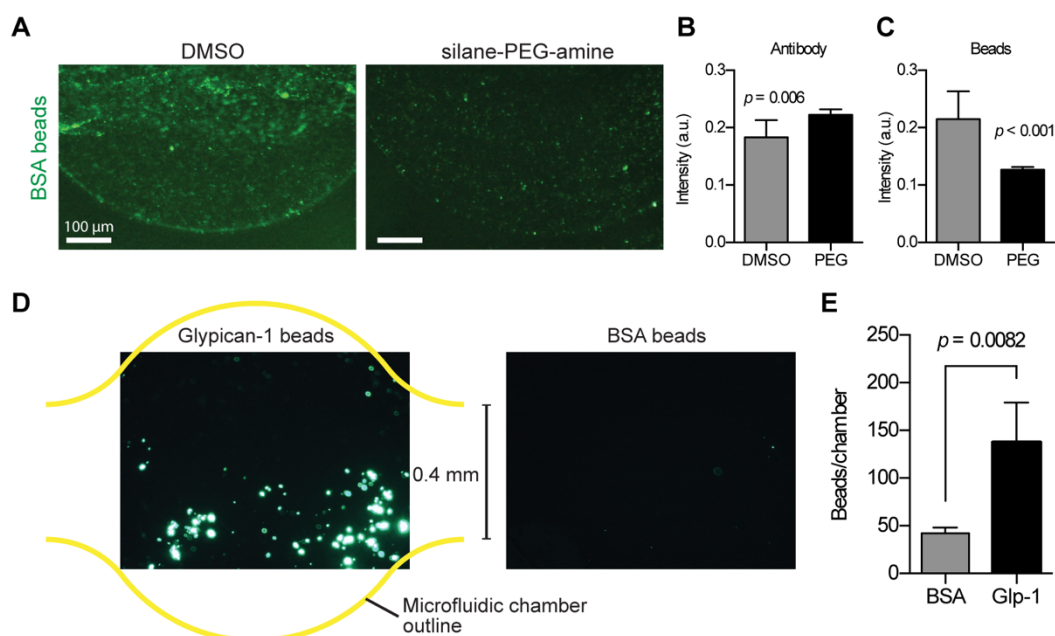


**Figure 4-10.** Non-specific adsorption of beads coated with BSA is reduced on silane-PEG-amine conjugated surfaces. **(A)** Fluorescence of BSA-coated beads that non-specifically attached to antibody-covered surfaces with or without a PEG linker. **(B)** Intensity of antibodies immobilized on surfaces. **(C)** Intensity of BSA-coated beads in channels of **A**. **(D)** and **(E)** Selective attachment of glypican-coated beads in comparison to BSA-only coated beads.

#### 4.3.3 Graphene-microfluidic integration

To improve upon extracellular vesicle detection with a more robust sensor, we developed a graphene FET biosensor. As discussed in **Section 4.1.4: Design considerations**, Deybe-Hückel screening can limit the sensitivity of a FET device due to aqueous ions. Thus, we introduced microfluidics to allow control over fluid flow across the sensor and replace solutions as needed. Channels were 1 cm long and 1 mm wide. Bonding of PDMS to substrates typically involves oxygen plasma treatment of surfaces or other chemical modification. Chemical modification of graphene is not appropriate, given that the pristine structure of graphene is key to its electronic properties. Instead, we constructed a clamp system to physically bond the PDMS to the silicon substrate (**Figure 4-11**). Integrating microfluidics has three additional benefits: (1) flowing a sample across a sensor increases the probability of antibody-

antigen ligation in comparison to static conditions, (2) manipulation of the sample volume can maximize surface area : volume ratio, and (3) for measurements that require an extended incubation time (minutes-hours), the microfluidic channel prevents evaporation of the sample.

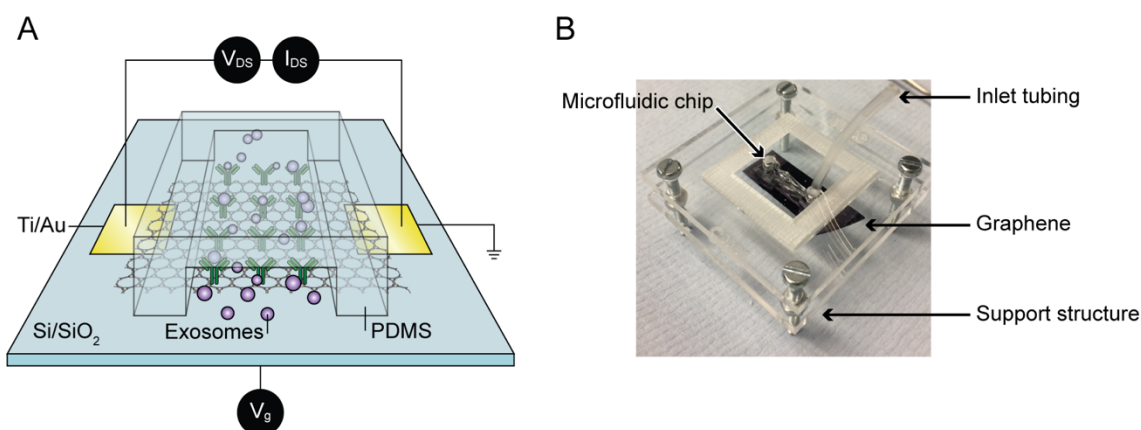


**Figure 4-11.** Integration of graphene biosensor with microfluidic element. **(A)** Graphene is exposed to solutions through the microfluidic channel and the current between the source and drain electrodes ( $I_{DS}$ ) is measured across values of the gate voltage ( $V_g$ ). **(B)** PDMS is clamped using a custom-made support structure made of PMMA (courtesy of Carlos Mattelan).

#### 4.3.4 XPS of exosomes on graphene

Graphene sensors were functionalized with antibodies via a PBASE linker as described in the Materials and Methods (**Section 4.2.4**). For this and subsequent experiments we functionalized the sensors with a CD63 antibody, which is a widely used marker for verification of vesicles of endosomal origin (i.e. a positive control for exosomes)<sup>32</sup>. We used XPS – which determines the elemental composition of surface layers – to characterize the graphene surfaces with each layer of functionalization. The nitrogen spectrum is informative for this purpose given that graphene is purely carbon, the unreacted PBASE linker is NHS terminated, and antibodies and exosomes contain many nitrogen-containing biomolecules. Each layer in this sequence increased the nitrogen signal in proportion with the expected nitrogen content of each, thereby confirming functionality (**Figure 4-12**).

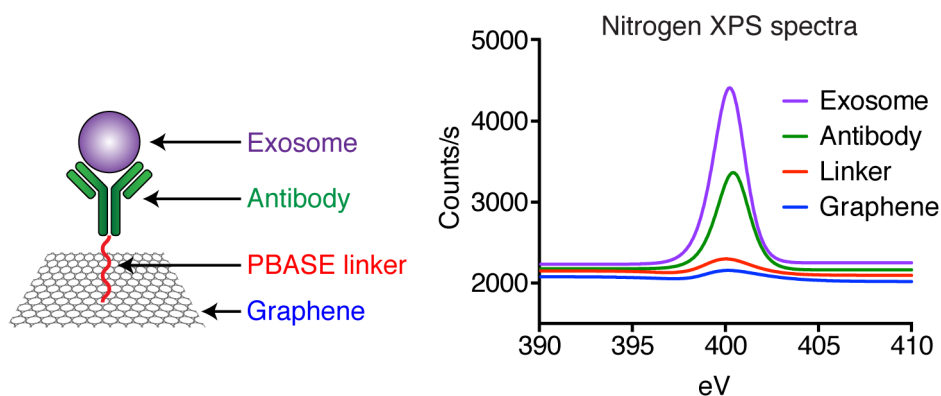


**Figure 4-12.** Nitrogen XPS spectra of graphene biosensor with increasing layers of functionalization. Colors in the diagram to the left are represented in the color scheme in the graph. Note that the preparation of devices for exosome capture here differs from the standard protocol in that NHS esters were not quenched with glycine, a primary amine, after antibody attachment.

#### 4.3.5 Exosome attachment to graphene biosensor

Extracellular vesicles were isolated from conventional ultracentrifugation of SUIT2-conditioned media (a pancreatic epithelial cell line) and characterized using SEM and NTA, which showed a population mode of 117 nm (**Figure 4-13A**). Additionally, we used lyophilized exosomes from healthy human plasma for characterization and testing of the biosensor. Exosomes were adherent on graphene sensors functionalized with the CD63 antibody (**Figure 4-13B and C**).

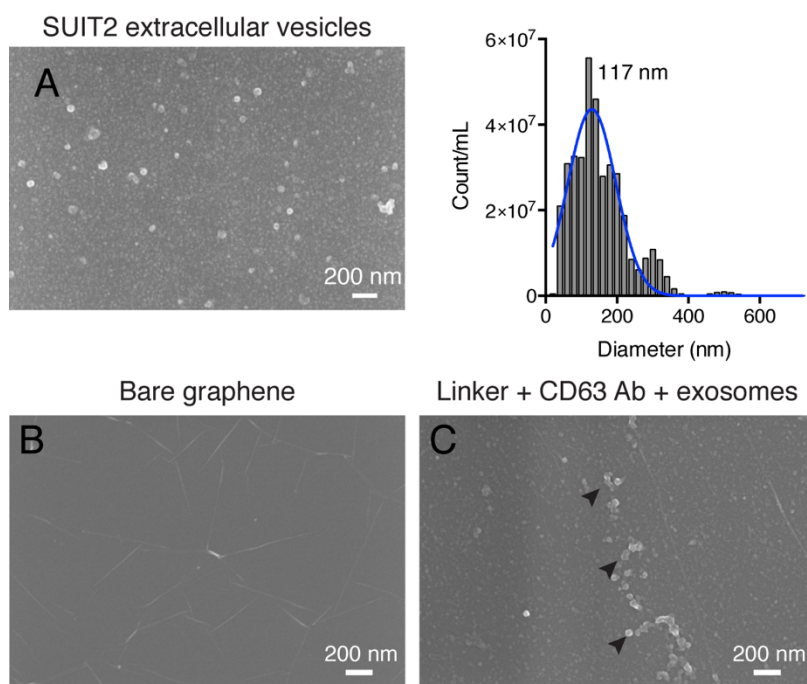


**Figure 4-13.** SEM of exosomes on graphene biosensor. **(A)** SEM imaging of extracellular vesicles on silicon isolated from SUIT2-conditioned media. NTA analysis shows the distribution of vesicle sizes in the population. **(B)** SEM imaging of non-functionalized graphene. **(C)** SEM imaging of functionalized graphene with adherent exosomes (arrowheads).

#### 4.3.6 Graphene FET response to PBS

When PBS is present in the channel, the graphene underneath is exposed to the charged species in solution and becomes regionally doped due to charge modulation<sup>33-35</sup>. This effect is observed through a new feature in the  $I_{DS}-V_g$  curve whereby an additional conductance minimum appears at a different  $V_g$  than that of the original Dirac point and is considered as the superposition of two  $I_{DS}-V_g$  curves of graphene with different doping levels. (The different areas of graphene can be seen in **Figure 4-11A**, where there is graphene underneath the microfluidic channel flanked by unexposed graphene on either side). This creates a p-n junction within the same graphene film whereby the uncovered graphene remains p-doped and the graphene exposed to the charged species is spatially and selectively n-doped. Hence, a higher density of electrons is induced in the graphene film under the channel. The additional minimum for each sensor appears at similar  $V_g$  with average position of  $9.3 \pm 0.7$  V ( $n = 4$  sensors), suggesting a consistent response of the sensor to PBS. The introduction of PBS caused n-doping of the graphene with respect to the original Dirac point, which can be attributed to the charge screening caused at the graphene/PBS interface<sup>36</sup>. Ions in PBS have the ability to screen negatively charged impurities present on the graphene surface that result in its overall p-doping. As a consequence, the potential distribution at the interface is altered and this screening effect acts to suppress these charges, reducing the effect of p-doping.

#### 4.3.7 Dirac point shifts of exosomes

To test the sensing properties of graphene,  $I_{DS}-V_g$  curves were determined for sensors functionalized with antibodies, with PBS solution, or  $10^{-2}$   $\mu\text{g}/\mu\text{L}$  ( $\sim 5 \times 10^5$  exosomes/ $\mu\text{L}$ ) of the exosome sample (**Figure 4-14A**). Introduction of exosomes induces a large shift in the Dirac point of the n-doped region within the microfluidic channel. For comparison, the Dirac point shift for most biosensing applications and appropriate analyte concentrations are generally  $<1$  V, depending on the gating strategy.

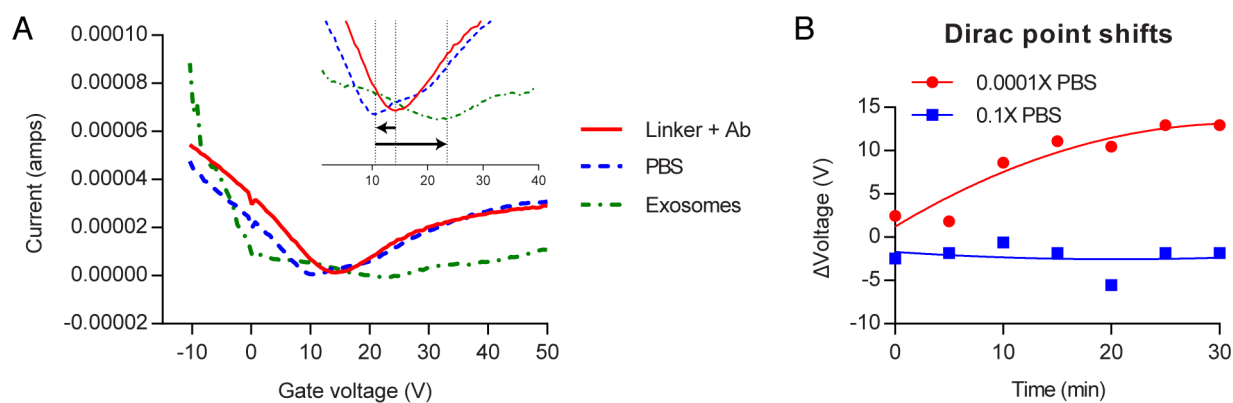


**Figure 4-14.** Measurement of exosome concentration using a graphene field effect transistor. **(A)** Characteristic current-gate voltage curves for graphene substrates with a linker conjugated CD63 antibody (Ab) (—), PBS on top of CD63-conjugated graphene (---), and exosomes on top of CD63-conjugated graphene (-.-). Inset: Dirac point shifts between the three conditions. **(B)** Time-resolved Dirac point shifts for  $10^{-2}$   $\mu\text{g}/\mu\text{L}$  exosomes dissolved in high or low concentration PBS in comparison to a PBS “blank.” Higher ionic strength solution effectively screens charges on exosomes and no Dirac point shift is detected.

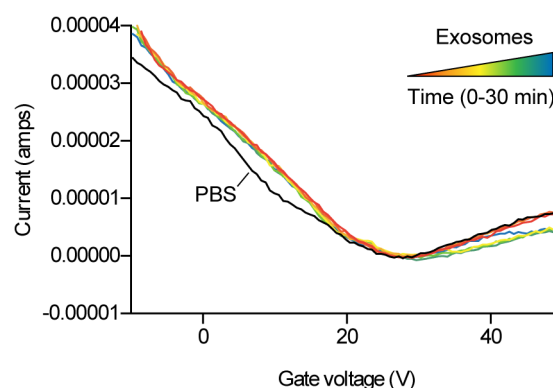


**Figure 4-15.** Current/gate voltage response to exosomes measured on graphene functionalized with an IgG isotype control antibody. Black line represents PBS “blank” measurement whereas other colored lines are measurements after introduction of exosomes every 5 minutes for 30 minutes. Overlapping lines indicates no change in Dirac point position.

We also compared the graphene sensitivity using PBS of different ion concentrations. The response was completely abrogated when 0.1x PBS was introduced in comparison to 0.0001x PBS (**Figure 4-14B**). The Debye length of 0.1x PBS is 2.3 nm, less than the length of an antibody<sup>30</sup>. Given the similarity of PBS ion concentration to that of blood plasma, measurement of plasma exosomes with the graphene sensor may be abrogated due to the screening effect of plasma ions. However, this reinforces the utility of microfluidic integration: once binding of exosomes to the sensor takes place, the solution can be replaced with a more suitable low-ion concentration buffer. Titration of an optimal pH may also allow protonation or ionization of vesicle proteins for increased signal generation. We also determined the sensor response to exosomes when the sensors were functionalized with a non-targeting IgG isotype



control antibody, which has no specificity for exosomes (**Figure 4-15**). As expected, no shifts in the Dirac point were observed, indicating that the charges on the surface of the graphene were unchanged.

To improve upon the consistency of devices and electrical contact between the source and drain, Ti/Au was patterned on the silicon substrate to act as source and drain electrodes. Then, we determined whether there are time-dependent changes in Dirac point shifts when the sensor was exposed to exosome solutions. The sensor response was investigated with exosomes in low ion concentration PBS pH 7, which was incubated in the channel for 30 minutes to ensure antibody-antigen binding, and  $I_{DS}$ - $V_g$  curves recorded every 5 minutes. The position of the additional conductance minimum was seen as expected for PBS, however a positive shift was observed when exosome solutions were introduced to the channel. **Figure 4-16A** clearly shows a representative sample in which there is a shift in the minimum over time. After 30 minutes, the position has moved 83.1 V from  $V_{PBS}$  to 92 V. Voltage changes are shown in **Figure 4-16B**, where  $\Delta V$  is the additional minimum's position at each time point, and a "saturation" in its position is seen by 30 minutes. The positive shift from the PBS position when exosomes are present indicates p-doping, which confirms the expected negative charge on exosomes at pH 7. To confirm this, exosomes were first bound to the sensor and then pH 5 buffer solution was pipetted into the microfluidic channel. The acidic solution would neutralize negative charges on the exosomes and negate the p-doping effect of exosomes (i.e. an n-doping effect). Accordingly, the pH 5 solution produces a leftward shift (**Figure 4-17**).

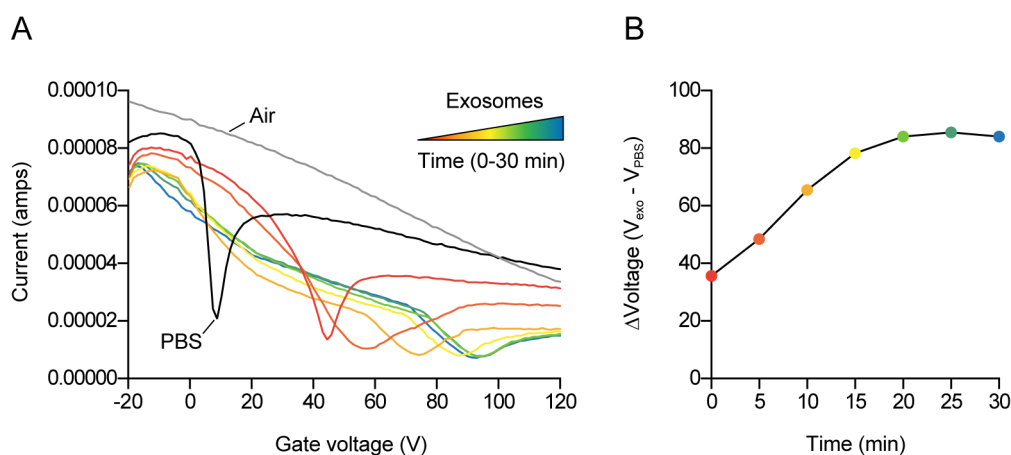


**Figure 4-16.** Graphene detection of exosomes is time-dependent. **(A)**  $I_{DS}$ - $V_g$  curves of  $10^{-2}$   $\mu\text{g}/\mu\text{L}$  exosomes in dilute PBS measured every 5 minutes for 30 minutes. **(B)** Dirac point voltage changes due to exosomes as a function of time.



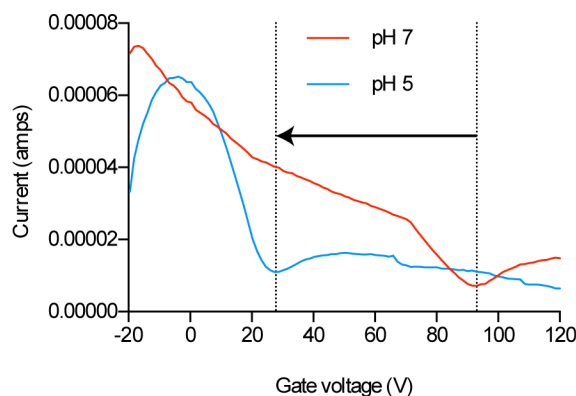


**Figure 4-17.** Dirac point shift of exosomes when a neutral buffer is replaced with a pH 5 solution, indicating a neutralization of exosome-mediated p-doping.

There is a time-dependent shift in the position of the Dirac point, indicating that the functionalized graphene surface is specific to exosomes compared to the response to BSA, which did not change over time (data not shown). Ostensibly, the saturation in the minimum's position after 30 minutes in **Figure 4-16B** may be attributed to two factors: (i) the binding and detection of all exosomes introduced to the graphene FET surface and/or (ii) all antibody binding sites on the graphene FET surface are occupied. Likely in the absence of mixing, many exosomes within the microfluidic channel do not come into contact with the sensor surface and cannot interact with antibodies. However, **Figure 4-16** demonstrates that the sensor is capable of detecting exosomes, and that further improvements to the design may enhance sensitivity.

#### 4.4 Conclusions

In this study, back-gated graphene FETs were fabricated using monolayer graphene and chemically modified for the selective detection of exosomes. By using a PDMS microfluidic channel, several different analytes can be introduced that have been shown to spatially dope the graphene giving rise to the formation of a controllable p-n junction within the same film, which does not cause degradation of electronic transport properties. As a result, an additional minimum, along with the original Dirac point of the graphene, appears on the  $I_{DS}-V_g$  curve when charged species are introduced through the channel. The position of this feature in relation to a reference point can be used to assess the nature of the charge on each molecule. If low concentrations of those expelled by cancerous cells can be counted and captured from a sub-milliliter

liquid sample, the graphene FET sensor may prove to be a sensitive and useful tool for early-stage cancer diagnosis.

## 4.5 Contributions and Acknowledgements

TJL designed and fabricated IDT prototypes, contributed to graphene biosensor design, conducted experiments, collected and analyzed data. DKHT developed graphene sensor, conducted experiments, and collected data. Technical assistance with ultracentrifugation was provided by Brian Cheung. The authors would like to thank A. Mihai and the London Centre for Nanotechnology for assistance and A. Chronopoulos for initial conceptualization of the acoustophoresis project. This study was supported by the European Research Council (ERC 282051) and Imperial Confidence in Concept scheme. TJL is supported by the James Dyson Foundation.

## 4.6 References

- 1 Duffy, D. C., McDonald, J. C., Schueller, O. J. & Whitesides, G. M. Rapid Prototyping of Microfluidic Systems in Poly(dimethylsiloxane). *Anal Chem.* 1998; 70, 4974-4984.
- 2 Whitesides, G. M. The origins and the future of microfluidics. *Nature.* 2006; 442, 368-373.
- 3 Yetisen, A. K. & Volpatti, L. R. Patent protection and licensing in microfluidics. *Lab Chip.* 2014; 14, 2217-2225.
- 4 Gronewold, T. M. Surface acoustic wave sensors in the bioanalytical field: recent trends and challenges. *Anal Chim Acta.* 2007; 603, 119-128.
- 5 Ballantine Jr, D., White, R. M., Martin, S. J., Ricco, A. J., Zellers, E., Frye, G. & Wohltjen, H. (1996). *Acoustic wave sensors: theory, design and physico-chemical applications*: Academic press.
- 6 Ding, X., Li, P., Lin, S. C., Stratton, Z. S., Nama, N., Guo, F., Slotcavage, D., Mao, X., Shi, J., Costanzo, F. & Huang, T. J. Surface acoustic wave microfluidics. *Lab Chip.* 2013; 13, 3626-3649.
- 7 White, R. & Voltmer, F. Direct piezoelectric coupling to surface elastic waves. *Applied physics letters.* 1965; 7, 314-316.
- 8 Ruppel, C. C., Reindl, L. & Weigel, R. SAW devices and their wireless communications applications. *IEEE microwave magazine.* 2002; 3, 65-71.
- 9 Campbell, C. (1998). *Surface acoustic wave devices for mobile and wireless communications*: Academic press.
- 10 Lindner, G. Sensors and actuators based on surface acoustic waves propagating along solid-liquid interfaces. *Journal of Physics D: Applied Physics.* 2008; 41, 123002.
- 11 Jhang, K.-Y. Nonlinear ultrasonic techniques for nondestructive assessment of micro damage in material: a review. *International journal of precision engineering and manufacturing.* 2009; 10, 123-135.

- 12 Du, J., Harding, G., Ogilvy, J. A., Dencher, P. & Lake, M. A study of Love-wave acoustic sensors. *Sensors and Actuators A: Physical*. 1996; 56, 211-219.
- 13 Fu, Y. Q., Luo, J., Nguyen, N.-T., Walton, A., Flewitt, A. J., Zu, X.-T., Li, Y., McHale, G., Matthews, A. & Iborra, E. Advances in piezoelectric thin films for acoustic biosensors, acoustofluidics and lab-on-chip applications. *Prog Mater Sci*. 2017; 89, 31-91.
- 14 Shi, J., Huang, H., Stratton, Z., Huang, Y. & Huang, T. J. Continuous particle separation in a microfluidic channel via standing surface acoustic waves (SSAW). *Lab Chip*. 2009; 9, 3354-3359.
- 15 Ding, X., Peng, Z., Lin, S. C., Geri, M., Li, S., Li, P., Chen, Y., Dao, M., Suresh, S. & Huang, T. J. Cell separation using tilted-angle standing surface acoustic waves. *Proc Natl Acad Sci U S A*. 2014; 111, 12992-12997.
- 16 Lee, K., Shao, H., Weissleder, R. & Lee, H. Acoustic purification of extracellular microvesicles. *ACS Nano*. 2015; 9, 2321-2327.
- 17 Taller, D., Richards, K., Slouka, Z., Senapati, S., Hill, R., Go, D. B. & Chang, H. C. On-chip surface acoustic wave lysis and ion-exchange nanomembrane detection of exosomal RNA for pancreatic cancer study and diagnosis. *Lab Chip*. 2015; 15, 1656-1666.
- 18 Li, P., Mao, Z., Peng, Z., Zhou, L., Chen, Y., Huang, P. H., Truica, C. I., Drabick, J. J., El-Deiry, W. S., Dao, M., Suresh, S. & Huang, T. J. Acoustic separation of circulating tumor cells. *Proc Natl Acad Sci U S A*. 2015; 112, 4970-4975.
- 19 Novoselov, K. S., Fal'ko, V. I., Colombo, L., Gellert, P. R., Schwab, M. G. & Kim, K. A roadmap for graphene. *Nature*. 2012; 490, 192-200.
- 20 Novoselov, K. S., Geim, A. K., Morozov, S. V., Jiang, D., Zhang, Y., Dubonos, S. V., Grigorieva, I. V. & Firsov, A. A. Electric field effect in atomically thin carbon films. *Science*. 2004; 306, 666-669.
- 21 Zhan, B., Li, C., Yang, J., Jenkins, G., Huang, W. & Dong, X. Graphene field-effect transistor and its application for electronic sensing. *Small*. 2014; 10, 4042-4065.
- 22 Kim, D. J., Sohn, I. Y., Jung, J. H., Yoon, O. J., Lee, N. E. & Park, J. S. Reduced graphene oxide field-effect transistor for label-free femtomolar protein detection. *Biosens Bioelectron*. 2013; 41, 621-626.
- 23 Dong, X., Shi, Y., Huang, W., Chen, P. & Li, L. J. Electrical detection of DNA hybridization with single-base specificity using transistors based on CVD-grown graphene sheets. *Adv Mater*. 2010; 22, 1649-1653.
- 24 Zhang, H., Freitas, D., Kim, H. S., Fabijanic, K., Li, Z., Chen, H., Mark, M. T., Molina, H., Martin, A. B., Bojmar, L., Fang, J., Rampersaud, S., Hoshino, A., Matei, I., Kenific, C. M., Nakajima, M., Mutvei, A. P., Sansone, P., Buehring, W., Wang, H., Jimenez, J. P., Cohen-Gould, L., Paknejad, N., Brendel, M., Manova-Todorova, K., Magalhaes, A., Ferreira, J. A., Osorio, H., Silva, A. M., Massey, A., Cubillos-Ruiz, J. R., Galletti, G., Giannakakou, P., Cuervo, A. M., Blenis, J., Schwartz, R., Brady, M. S., Peinado, H., Bromberg, J., Matsui, H., Reis, C. A. & Lyden, D. Identification of distinct nanoparticles and subsets of extracellular vesicles by asymmetric flow field-flow fractionation. *Nat Cell Biol*. 2018; 20, 332-343.
- 25 Wu, M., Ouyang, Y., Wang, Z., Zhang, R., Huang, P. H., Chen, C., Li, H., Li, P., Quinn, D., Dao, M., Suresh, S., Sadovsky, Y. & Huang, T. J. Isolation of exosomes from whole blood by integrating acoustics and microfluidics. *Proc Natl Acad Sci U S A*. 2017; 114, 10584-10589.
- 26 Davies, R. T., Kim, J., Jang, S. C., Choi, E. J., Gho, Y. S. & Park, J. Microfluidic filtration system to isolate extracellular vesicles from blood. *Lab Chip*. 2012; 12, 5202-5210.

- 27 Kang, Y. T., Kim, Y. J., Bu, J., Cho, Y. H., Han, S. W. & Moon, B. I. High-purity capture and release of circulating exosomes using an exosome-specific dual-patterned immunofiltration (ExoDIF) device. *Nanoscale*. 2017; 9, 13495-13505.
- 28 Farid, S., Meshik, X., Choi, M., Mukherjee, S., Lan, Y., Parikh, D., Poduri, S., Baterdene, U., Huang, C. E., Wang, Y. Y., Burke, P., Dutta, M. & Stroschio, M. A. Detection of Interferon gamma using graphene and aptamer based FET-like electrochemical biosensor. *Biosens Bioelectron*. 2015; 71, 294-299.
- 29 Forsyth, R., Devadoss, A. & Guy, O. J. Graphene Field Effect Transistors for Biomedical Applications: Current Status and Future Prospects. *Diagnostics (Basel)*. 2017; 7.
- 30 Stern, E., Wagner, R., Sigworth, F. J., Breaker, R., Fahmy, T. M. & Reed, M. A. Importance of the Debye screening length on nanowire field effect transistor sensors. *Nano Lett*. 2007; 7, 3405-3409.
- 31 Shih, W.-C., Chen, Y.-C., Chang, W.-T., Cheng, C.-C., Liao, P.-C. & Kao, K.-S. Design and fabrication of nanoscale IDTs using electron beam technology for high-frequency SAW devices. *Journal of Nanomaterials*. 2014; 2014, 2.
- 32 Thery, C., Amigorena, S., Raposo, G. & Clayton, A. Isolation and characterization of exosomes from cell culture supernatants and biological fluids. *Curr Protoc Cell Biol*. 2006; Chapter 3, Unit 3 22.
- 33 Feng, T., Xie, D., Xu, J., Zhao, H., Li, G., Ren, T. & Zhu, H. Back-gate graphene field-effect transistors with double conductance minima. *Carbon*. 2014; 79, 363-368.
- 34 Baltazar, J., Sojoudi, H., Paniagua, S. A., Kowalik, J., Marder, S. R., Tolbert, L. M., Graham, S. & Henderson, C. L. Facile formation of graphene p-n junctions using self-assembled monolayers. *The Journal of Physical Chemistry C*. 2012; 116, 19095-19103.
- 35 Sun, Y., Xie, D., Zhang, C., Li, X., Xu, J., Sun, M., Teng, C., Li, X. & Zhu, H. Poly (ethylene imine)-modulated transport behaviors of graphene field effect transistors with double Dirac points. *Journal of Applied Physics*. 2017; 121, 134305.
- 36 Hess, L. H., Seifert, M. & Garrido, J. A. Graphene transistors for bioelectronics. *Proceedings of the IEEE*. 2013; 101, 1780-1792.

## Chapter 5: Conclusions and future work

### 5.1 Role of tamoxifen in immune modulation

In Chapter 2, we explored the use of tamoxifen in regulating biomechanical properties of macrophages. Beginning with the observation that macrophage stromal infiltration is reduced in KPC mice treated with tamoxifen, we show that tamoxifen regulates important biomechanical parameters *in vitro*. Such changes are consistent with reduced TLR4 expression, which is also reduced in macrophages *in vivo*. Further work is necessary to fully delineate the direct effect of tamoxifen on macrophages and the indirect secondary and tertiary interactions on macrophages due to its action on PSCs and the ECM. Specifically, paracrine networks and subsequent chemokine gradients between PSCs and macrophages or between cancer cells and macrophages may be modulated by tamoxifen; alternatively, tamoxifen-mediated ECM remodeling and amelioration of desmoplasia may regulate macrophage migration and phenotype.

It may also be necessary to study these and previous hypothesis in primary human peripheral blood isolated monocytes/macrophages or murine bone marrow derived macrophages, as well as other immune cell types such as neutrophils, myeloid derived suppressor cells, and T cells. Whether tamoxifen affects extravasation and migration of inflammatory monocytes to the tumor site or the *in situ* expansion of tissue resident macrophages may also have important implications for carcinogenesis and malignancy in accordance with their differing roles<sup>1</sup>. Similarly, the action of tamoxifen on macrophages or neutrophils systemically may have implications for the establishment of a pre-metastatic niche, which relies on these cell types for initiating a favorable inflammatory environment for tumor cell establishment<sup>2,3</sup>.

### 5.2 Macrophage mechanobiology

Further work is required to understand the mechanistic underpinnings and implications of macrophage mechanobiology, particularly in context of disease. As far as we are aware, there are no other studies that specifically target macrophage biomechanics in cancer treatment beyond inhibiting cytoskeletal activity like actin polymerization<sup>4</sup>. Future studies on macrophage mechanics might benefit from engineered 3D biomaterial systems to fully understand the contributions of ECM composition, architecture, and porosity to macrophage function in addition to substrate rigidity<sup>5</sup>.

Microfluidic *in vitro* systems might also be employed to control ECM parameters and stiffness/chemokine gradients.

### 5.3 Extracellular vesicle diagnostics

Chapter 4 outlines the methods and development of acoustophoresis, microfluidics, and a graphene field effect transistor for use in extracellular vesicle processing and analysis. Several important considerations should be addressed in further development of these devices for research or potential clinical use.

- *Device integration.* The versatility of microfluidic and LOC fabrication processes allows development of devices with multiple functions. This is advantageous in cases where portability and usability are essential because it limits size and reduces operator involvement. Here, two devices were designed separately mainly due to substrate incompatibilities: the IDTs are deposited on lithium niobate whereas the graphene is mounted on a silicon chip. However, quartz is a suitable candidate that may be used for both devices – it is piezoelectric and has previously been used as a combined SAW-graphene gas sensor<sup>6</sup>. In a combined configuration, a single syringe pump would be required to flow a sample through the acoustophoretic aperture, and isolated vesicles would continue on to be perfused over the graphene sensor. Further work is required to demonstrate full functionality of the acoustophoresis module in order to integrate it with the graphene biosensor.
- *Miniaturization of components.* Integration of components on the device would be best achieved if electrical components could be miniaturized on-chip. Both devices currently require the use of bench-top electrical components that limit its use to a research setting.
- *Multiplexing capabilities and multiparametric sensing.* Essential to biomarker discovery is the ability to interrogate many proteins (or other biomarkers) in order to determine relative expression within and between samples. In this way, Yang *et al.* (2017) were recently able to multiplex an existing plasmonic assay with 100 independent sites of measurement to identify a five-marker signature of PDAC<sup>7</sup>. However, for graphene devices, manufacturing multiple graphene sheets on a single chip with integrated electrical connections and microfluidic channels is not trivial and may require novel approaches. An alternative might

be to strip the sensor surface to be reused, a method which has been used for graphene oxide nucleic acid sensors<sup>8</sup>. The sensing principle used by graphene (i.e. charge) may provide additional information about extracellular vesicle composition and structure; if the zeta potential of the vesicles is known, the absolute concentration of vesicles could be inferred, and *vice versa*. The label-free nature of detection also allows investigation of time-dependent binding events, which could provide information about binding kinetics and interrogation of preferential binding to cell adhesion molecules. This may be of use in investigating mechanisms of exosome biodistribution and formation of a pre-metastatic niche, which is dependent on expression of vesicle integrins<sup>9</sup>.

- *Limit of detection and vesicle concentration.* An important consideration of the graphene sensor is the limit of detection, sensitivity, and propensity for detecting background proteins and ions. In future work, the sensitivity and signal-to-noise ratio of exosome standards spiked with plasma proteins will be determined prior to validation of sensitivity and specificity of exosomal biomarkers in clinical samples. The detection of background non-specifically adsorbed proteins may pose a significant obstacle to specific detection of bound exosomes for a graphene sensor, which is mostly hydrophobic when aged in air<sup>10</sup>. Several modifications may be introduced to improve sensitivity and specificity including fluidic mixing of the sample across the sensor, blocking non-specific adsorption of vesicles/proteins without affecting sensor performance, improved antibody conjugation methods, or implementing an electrolytic top-gate. Other methods of amplifying a specific signal may also be explored, such as a metal nanoparticle secondary label.

The concentration of vesicles in blood plasma would determine the minimum volume of sample required to achieve a limit of detection given that the acoustophoretic isolation method does not concentrate vesicles and may in fact dilute them. However, microfluidic filtration methods can be implemented in order to concentrate isolated vesicles for detection. In previous work using acoustophoresis for extracellular vesicle isolation, separation efficiencies and purity can be extremely high<sup>11,12</sup>. To maintain this efficiency and improve the acoustophoretic power, an impedance matching network<sup>11</sup> can be implemented and a different microchannel material, such as PMMA, might reduce insertion loss of the SAW.

- *Downstream vesicle analysis.* Although perhaps not an advantage for multiplexing graphene sensors, the benefit of CVD-grown graphene is formation of large surface area graphene sheets. Depending on the dimensions of the constraining microfluidic channel, the sample can bind to a large surface area and may be recovered for downstream analysis such as PCR identification of intravesicular RNAs. This strategy has been employed in an electrokinetic microarray chip that isolated exosomes, after which vesicles were released and lysed for PCR<sup>13</sup>. Vesicles can also be lysed on-chip for further analysis<sup>14</sup>.

## 5.4 References

- 1 Zhu, Y., Herndon, J. M., Sojka, D. K., Kim, K. W., Knolhoff, B. L., Zuo, C., Cullinan, D. R., Luo, J., Bearden, A. R., Lavine, K. J., Yokoyama, W. M., Hawkins, W. G., Fields, R. C., Randolph, G. J. & DeNardo, D. G. Tissue-Resident Macrophages in Pancreatic Ductal Adenocarcinoma Originate from Embryonic Hematopoiesis and Promote Tumor Progression. *Immunity*. 2017; 47, 323-338 e326.
- 2 Nielsen, S. R., Quaranta, V., Linford, A., Emeagi, P., Rainer, C., Santos, A., Ireland, L., Sakai, T., Sakai, K., Kim, Y. S., Engle, D., Campbell, F., Palmer, D., Ko, J. H., Tuveson, D. A., Hirsch, E., Mielgo, A. & Schmid, M. C. Macrophage-secreted granulin supports pancreatic cancer metastasis by inducing liver fibrosis. *Nat Cell Biol*. 2016; 18, 549-560.
- 3 Steele, C. W., Karim, S. A., Leach, J. D. G., Bailey, P., Upstill-Goddard, R., Rishi, L., Foth, M., Bryson, S., McDaid, K., Wilson, Z., Eberlein, C., Candido, J. B., Clarke, M., Nixon, C., Connelly, J., Jamieson, N., Carter, C. R., Balkwill, F., Chang, D. K., Evans, T. R. J., Strathdee, D., Biankin, A. V., Nibbs, R. J. B., Barry, S. T., Sansom, O. J. & Morton, J. P. CXCR2 Inhibition Profoundly Suppresses Metastases and Augments Immunotherapy in Pancreatic Ductal Adenocarcinoma. *Cancer Cell*. 2016; 29, 832-845.
- 4 Pergola, C., Schubert, K., Pace, S., Ziereisen, J., Nikels, F., Scherer, O., Huttel, S., Zahler, S., Vollmar, A. M., Weinigel, C., Rummeler, S., Muller, R., Raasch, M., Mosig, A., Koeberle, A. & Werz, O. Modulation of actin dynamics as potential macrophage subtype-targeting anti-tumour strategy. *Sci Rep*. 2017; 7, 41434.
- 5 Springer, N. L. & Fischbach, C. Biomaterials approaches to modeling macrophage-extracellular matrix interactions in the tumor microenvironment. *Curr Opin Biotechnol*. 2016; 40, 16-23.
- 6 Whitehead, E., Chick, E., Bandhu, L., Lawton, L. & Nash, G. R. Gas loading of graphene-quartz surface acoustic wave devices. *Applied Physics Letters*. 2013; 103, 063110.
- 7 Yang, K. S., Im, H., Hong, S., Pergolini, I., Del Castillo, A. F., Wang, R., Clardy, S., Huang, C. H., Pille, C., Ferrone, S., Yang, R., Castro, C. M., Lee, H., Del Castillo, C. F. & Weissleder, R. Multiparametric plasma EV profiling facilitates diagnosis of pancreatic malignancy. *Sci Transl Med*. 2017; 9.
- 8 Liu, X., Aizen, R., Freeman, R., Yehezkeli, O. & Willner, I. Multiplexed aptasensors and amplified DNA sensors using functionalized graphene oxide: application for logic gate operations. *ACS Nano*. 2012; 6, 3553-3563.
- 9 Hoshino, A., Costa-Silva, B., Shen, T. L., Rodrigues, G., Hashimoto, A., Tesic Mark, M., Molina, H., Kohsaka, S., Di Giannatale, A., Ceder, S., Singh, S., Williams, C., Soplod, N., Uryu, K., Pharmed, L., King, T., Bojmar, L., Davies, A. E., Ararso, Y., Zhang, T., Zhang, H., Hernandez, J., Weiss, J. M., Dumont-Cole, V. D., Kramer, K., Wexler, L. H., Narendran, A., Schwartz, G.




- K., Healey, J. H., Sandstrom, P., Labori, K. J., Kure, E. H., Grandgenett, P. M., Hollingsworth, M. A., de Sousa, M., Kaur, S., Jain, M., Mallya, K., Batra, S. K., Jarnagin, W. R., Brady, M. S., Fodstad, O., Muller, V., Pantel, K., Minn, A. J., Bissell, M. J., Garcia, B. A., Kang, Y., Rajasekhar, V. K., Ghajar, C. M., Matei, I., Peinado, H., Bromberg, J. & Lyden, D. Tumour exosome integrins determine organotropic metastasis. *Nature*. 2015; 527, 329-335.
- 10 Li, Z., Wang, Y., Kozbial, A., Shenoy, G., Zhou, F., McGinley, R., Ireland, P., Morganstein, B., Kunkel, A., Surwade, S. P., Li, L. & Liu, H. Effect of airborne contaminants on the wettability of supported graphene and graphite. *Nat Mater*. 2013; 12, 925-931.
- 11 Lee, K., Shao, H., Weissleder, R. & Lee, H. Acoustic purification of extracellular microvesicles. *ACS Nano*. 2015; 9, 2321-2327.
- 12 Wu, M., Ouyang, Y., Wang, Z., Zhang, R., Huang, P. H., Chen, C., Li, H., Li, P., Quinn, D., Dao, M., Suresh, S., Sadvovsky, Y. & Huang, T. J. Isolation of exosomes from whole blood by integrating acoustics and microfluidics. *Proc Natl Acad Sci U S A*. 2017; 114, 10584-10589.
- 13 Ibsen, S. D., Wright, J., Lewis, J. M., Kim, S., Ko, S. Y., Ong, J., Manouchehri, S., Vyas, A., Akers, J., Chen, C. C., Carter, B. S., Esener, S. C. & Heller, M. J. Rapid Isolation and Detection of Exosomes and Associated Biomarkers from Plasma. *ACS Nano*. 2017; 11, 6641-6651.
- 14 Chen, C., Skog, J., Hsu, C. H., Lessard, R. T., Balaj, L., Wurdinger, T., Carter, B. S., Breakefield, X. O., Toner, M. & Irimia, D. Microfluidic isolation and transcriptome analysis of serum microvesicles. *Lab Chip*. 2010; 10, 505-511.

## Appendix: Copyright Permissions

Permission for **Figure 1-2**.

[Copy order >](#)

 [Print this page](#)  
[Print terms & conditions](#)  
[Print citation information](#)  
[\(What's this?\)](#)

**Confirmation Number: 11695669**  
**Order Date: 01/29/2018**

### Customer Information

**Customer:** Tyler Lieberthal  
**Account Number:** 3001240604  
**Organization:** Tyler Lieberthal  
**Email:** t.lieberthal15@imperial.ac.uk  
**Phone:** +44 7492567320

Search order details by:


**This is not an invoice**

### Order Details

**Convergent science physical oncology**

Billing Status:  
**N/A**

**Order detail ID:** 70975868  
**ISSN:** 2057-1739  
**Publication Type:** Journal  
**Volume:**  
**Issue:**  
**Start page:**  
**Author/Editor:** Institute of Physics (Great Britain),

**Permission Status:**  **Granted**  
**Permission type:** Republish or display content  
**Type of use:** Thesis/Dissertation  
**Order License Id:** 4278150950415

[View details](#)


**Note:** This item was invoiced separately through our **RightsLink service**. [More info](#)

**\$ 0.00**

**Total order items: 1**

**Order Total: \$0.00**

Permissions for **Figure 1-7**.[Back to view orders](#)[Copy order](#)

 [Print this page](#)  
[Print terms & conditions](#)  
[Print citation information](#)  
[\(What's this?\)](#)

**Confirmation Number: 11695668**  
**Order Date: 01/29/2018**


**Customer Information**

**Customer:** Tyler Lieberthal  
**Account Number:** 3001240604  
**Organization:** Tyler Lieberthal  
**Email:** t.lieberthal15@imperial.ac.uk  
**Phone:** +44 7492567320

Search order details by:

**This is not an invoice****Order Details****Convergent science physical oncology**

Billing Status: <b>N/A</b>
-------------------------------

**Order detail ID:** 70975867**ISSN:** 2057-1739**Publication Type:** Journal**Volume:****Issue:****Start page:****Author/Editor:** Institute of Physics (Great Britain),**Permission Status:**  **Granted****Permission type:** Republish or display content**Type of use:** Thesis/Dissertation**Order License Id:** 4278150707991[View details](#)**Note:** This item was invoiced separately through our **RightsLink service**. [More info](#)**\$ 0.00****Total order items: 1****Order Total: \$0.00**